

NASA CR-66518

N68-13962

DESIGN CRITERIA AND CONCEPTS  
FOR FIBROUS COMPOSITE STRUCTURES

by Norris F. Dow, B. Walter Rosen,

Larry S. Shu and Carl H. Zweben

Space Sciences Laboratory

July 1967

Prepared under Contract NASw-1377 by  
General Electric Company  
Philadelphia, Pennsylvania  
for  
National Aeronautics and Space Administration

Distribution of this report is provided in the interest of information exchange. Responsibility for the contents resides in the author or organization that prepared it.

## ABSTRACT

The results of a program to study the analysis and design of composite materials and structures is reported. Emphasis was placed upon three major areas: The definition of design criteria for laminates including studies of basic failure mechanisms; the definition of unique design concepts to enhance the beneficial characteristics of composite materials and to utilize them in structures; and the analysis of composite materials property test techniques.

## FOREWORD

This document is the annual report on the program entitled "Study of the Relationship of Properties of Composite Materials to Properties of Their Constituents". The program was performed for the National Aeronautics and Space Administration under Contract NASw-1377 and was monitored by Dr. R. W. Leonard of the NASA Structures Research Division.

# TABLE OF CONTENTS

	Page
INTRODUCTION . . . . .	1
DESIGN CRITERIA . . . . .	3
<u>Laminate Strength</u> . . . . .	5
<u>Lamina Strength</u> . . . . .	9
Limit Analysis of Unidirectional Fibrous Composites . .	11
Tensile Strength . . . . .	33
The Steady State Viscoelastic Response . . . . .	50
<u>Evaluation of Transverse Effectiveness Factors for Use in</u>	
<u>Elastic Analysis of Three Dimensional Filamentary Composites</u>	62
DESIGN CONCEPTS . . . . .	65
<u>Study of Composite Structures</u> . . . . .	65
Circular Tube Columns . . . . .	66
Scalloped Tube Columns . . . . .	71
Plate Efficiencies . . . . .	74
Panel Efficiencies . . . . .	77
<u>Studies of Composite Materials</u> . . . . .	80
Three-Dimensionally Isotropic Materials . . . . .	80
Three Phase Composite Compression Members . . . . .	87
STUDIES OF MATERIALS PROPERTIES TESTS . . . . .	93
<u>The NOL Split-Dee Tensile Test</u> . . . . .	93
Variations of the Split-Dee Test . . . . .	96

	Page
<u>Compression Tests of NOL Rings</u> . . . . .	99
<u>Low-Melting Alloy Casting Fixture of Compression Tests</u> . . . .	101
<u>Elastic Moduli</u> . . . . .	102
Axial Compression Test . . . . .	110
Internal Pressure Test . . . . .	112
Tension Test . . . . .	114
CONCLUDING REMARKS . . . . .	115
REFERENCES . . . . .	117
APPENDIX A . . . . .	120
APPENDIX B . . . . .	131
TABLES . . . . .	136
FIGURES . . . . .	144

# LIST OF TABLES

Table No.		Page No.
1	Generalized Equations for Compliances having Uni-directional Reinforcing Filaments in the 1-direction (from Ref. 1).	136
2	Relationships among Elastic Constants and Compliances for Uni-directional Reinforcement for use in Evaluations of the Various $\beta$ 's in Table 1 (from Ref. 1).	137
3	Equations for the Transvers Effectiveness Factors ( $\beta$ ) in Terms of the Elastic Constants for Uni-directional Reinforcement (Equations of Table 2 Solved in Terms of $\beta$ for $\beta_0$ Values equal to Unity).	138
4.	Generalized Equations for the Compliances of Three-Dimensionally Reinforced Composites having Three Orthogonal Planes of Symmetry.	139

# LIST OF FIGURES

<u>Figure</u>		<u>Page</u>
1	Calculated Stress-strain Curves for E-Glass and Epoxy Composite Laminates.	144
2	Yield Strength of a Symmetric Bi-axial Composite Laminate for Failure Modes Involving Each of the Principal Lamina Stresses.	145
3	Composite Specimen for Limit Analysis. (Fibers in $X_1$ -Direction).	146
4	Bounds on the Limit Load for In-plane Shear.	147
5	Bounds on the Limit Load for Transverse Tension.	148
6	Bounds on the Interaction Curves for In-plane Shear and Transverse Tension for Various Fiber Volume Fractions.	149
7	The $K^{\text{th}}$ Layer in a Laminate for the Limit Analysis Model.	150
8	Tensile Failure Model for a Composite Reinforced by Continuous Fibers.	150
9	Number of Breaks as a Function of Applied Load (Ref. 4, Series B).	151
10	Number of Breaks as a Function of Applied Load (Ref. 4, Series C).	152
11	Expected Number of Groups of Fractures as a Function of Applied Load (Ref. 4, Series B).	153
12	Expected Number of Groups of Fractures as a Function of Applied Load (Ref. 4, Series C).	154
13	Observed and Predicted Multiple-Fracture Groups (Ref. 4, Series B).	155
14	Observed and Predicted Multiple-Fracture Groups (Ref. 4, Series C).	156
15	Static and Dynamic Values of $P_{2/1}$ and $P_{3/1}$ as a Function of Applied Load (Ref. 4, Series B).	157

# LIST OF FIGURES (Cont.)

<u>Figure</u>		<u>Page</u>
16	Expected Number of Fracture Groups as a Function of Applied Load (Ref. 17 Tests).	158
17	Variation of $E_2$ with Applied Stress for Various Composite Lengths (Ref. 4, Series B).	159
18	Typical Variations of Transverse Effectivenesses of Filamentary Reinforcement with Volume Fraction, as Calculated for an E-Glass/Epoxy Composite.	160
19	Efficiencies of Round, Unreinforced Tube - Columns of 7075-T6 Aluminum Alloy and Beryllium.	161
20	Efficiencies of Round 7075-T6 Aluminum - Alloy Tube-Columns Reinforced at Three Circumferential Points by Uni-directional Boron/Epoxy Stiffeners.	162
21	Efficiencies of Round Beryllium Tube-Columns Reinforced at Three Circumferential Points by Uni-directional Boron/Epoxy Stiffeners.	163
22	Changes in Column-Binding Characteristics of Scalloped Thin-Walled Tubes at Constant R/t with Angle Included by Scallop.	164
23	Efficiencies of 7075-T6 Aluminum-Alloy Scalloped Triangle Thin-Walled Tube Columns Reinforced at Apexes with $0^\circ$ Boron/Epoxy Stiffeners, and Comparison with Minimum-Weight Reinforced 7075-T6 Round Tubes.	165
24	Efficiencies of Beryllium Scalloped Triangle Thin-Walled Tube Columns Reinforced at Apexes with $0^\circ$ Boron/Epoxy Stiffeners, and Comparison with Minimum-Weight Reinforced Beryllium Round Tubes.	166
25	Efficiencies of Solid-Sandwich Plates having $0^\circ$ Reinforced Boron/Epoxy Cores and Faces of Various Materials.	167
26	Comparative Efficiencies of Wing Box Beams having $\pm 45^\circ$ Boron Reinforced Epoxy Compression Skins and Beryllium Skins on $0^\circ$ Reinforced Boron/Epoxy Z-Section Stiffeners.	168



# LIST OF FIGURES (Cont.)

<u>Figure</u>		<u>Page</u>
27	Calculated Compliances $A_1$ , $A_4$ , and $A_6$ , Caltropic Reinforcement in the Directions of the Orthotropic axis 1-, 2-, 3- Respectively, for Equal and Unequal Assumed Transverse Effectiveness $\beta$ . ( $E_f = 10$ , $E_b = \frac{10}{21}$ , $\nu_f = 0.2$ , $\nu_b = 0.35$ ).	169
28	Calculated Compressive Strengths for Three Indicated Failure Modes for a Boron/Epoxy Composite of Nominal Constituent Properties with Constant Total Reinforcement Volume Fraction of 50% but Varying Proportions of the Reinforcement Uni-directional and Randomly Dispersed in the Binder.	170
29	Calculated Compressive Strengths for Three Indicated Failure Modes for Glass/Epoxy Composites of Nominal Constituent Properties with Constant Total Reinforcement Volume Fraction of 50%, but Varying Proportions of the Reinforcement Uni-directional and Randomly Dispersed in the Binder.	171
30	Calculated Compressive Strengths for Glass-Boron/Epoxy Composites of Nominal Constituent Properties with Constant Uni-directional Boron Reinforcement Volume Fraction $V_f = 0.5$ and Varying Quantities of Randomly Dispersed Glass Filaments in the Binder.	172
31	Experimental Results for Tests of Glass-Boron/Epoxy Composites having Uni-directional Boron Filamentary Reinforcement of Nominally 50% by Volume, and Comparison with Calculations for Various Glass-Filament and Binder Strengths.	173
32	Schematic of N. O. L. Ring, "Split-Dee" Tensile Test.	174
33	Photoelastic Study of Stresses in the Vicinity of the Split between the Dees in an N. O. L. Ring "Split-Dee" Tensile Test.	175
34	Results of Analysis of Maximum Bending Moment in the "Split-Dee" Test of a Glass Filament Reinforced Epoxy N. O. L. Ring.	176

# LIST OF FIGURES (Cont.)

<u>Figure</u>		<u>Page</u>
35	"Race-Track", Filament-Wound Tensile Specimen.	177
36	Ratios of Maximum Bending Moments Induced in Race-Track and Circular 0.15 cm. (0.06 in.) Thick Split-Dee Specimens of Glass/Epoxy at $0.69 \frac{\text{GN}}{\text{m}^2}$ (100 ksi) Axial Stress.	178
37	Schematic Representative of Mechanics of Deflection of "Race-Track" Specimen.	179
38	Photoelastic Study of Stresses in the Straightaway of a "Race-Track" Specimen.	180
39	Strain Measurements Near the Split in the Dee in N.O.L. Ring Type Split-Dee Tension Test.	181
40	Proposed Compression Specimen Made From Segments of N.O.L. Ring.	182
41	Aluminum Insert from Specimen Similar to that of Figure 40 after Test.	183
42	N.O.L. Ring Segment Compression Test Specimen Showing Shear Failure.	184
43.	Top and End Views of Compression Specimen Cast in Cerrobend End Fixtures.	185

## INTRODUCTION

Development of methods of analysis of the strength and stiffness of fibrous composites has advanced to the point where it is feasible to establish rational initial design procedures for composite structures. These procedures are naturally subject to revision as continuing studies enhance the understanding of composite failure mechanics. In conjunction with the theoretical developments, there is the unsatisfied need for definition of suitable techniques for material property measurements. Accordingly, the program described herein treated the above problem areas and the present report presents the results of investigations leading to: The definition of design criteria; the enhancement of the understanding of failure mechanisms; the definition of unique design concepts for composites; and the development of improved techniques for composite property measurement.

The section on "Design Criteria" describes the failure criteria for laminates, which have been computerized for structural efficiency analysis. Further studies of the laminae failure mechanisms upon which this is based are also described, including some treatment of time dependent behavior. The application of these criteria is treated in the "Design Concepts" section, wherein the utilization of the high uniaxial compressive strength of fibrous composites is emphasized. Columns, plates and panels of combined composite and metallic construction are designed and their potential is assessed. Concepts for improved material performance including three phase and isotropic three dimen-

sional materials are also defined. In the final section, "Studies of Materials Properties Tests" the results of the analysis of several current test techniques are presented along with suggested new methods for uniaxial strength measurements.

When, in the angle between the tensile load and the reinforcement direction is increased gradually from zero to ninety degrees, three primary failure modes can be expected to be encountered: first, at small angles, tensile failure of the filaments; second, at intermediate angles,

## DESIGN CRITERIA

The parametric evaluations of fibrous composites for aerospace structures (e. g. Refs. 1 and 2) have indicated the attractive potential of composite structures which are configured to achieve high stresses. When efficient stiffening arrangements permit the use of the high modulus composite materials high strength, the resulting structures are shown to be substantially lighter than metallic structures. These studies emphasized the need for better definition of composite strength. The prediction of laminate strength from a knowledge of constituent properties is a complex undertaking and, in general, strength estimates most suitable for design are obtained experimentally. However, an analytical estimate is required in the assessment of the potential of candidate composites which have not yet been brought to the practical fabrication stage. Indeed, the concept of analytically predicting composite properties for use in a structural application analysis, is an essential part of the search for guidelines for the development of improved composite materials.

The strengths of fibrous composites, perhaps to an even greater degree than their stiffnesses, are complex functions of the anisotropies associated with the uni-directional character of filaments. For filaments in one (the loaded) direction only, strength in tension (Ref. 3), compression (e. g. Ref. 4) and shear (e. g. Refs. 5, 6) have been related to the properties of the constituents. Further study of these problems is described subsequently. Extensions to reinforcements in other directions have now been incorporated into the computer programs for structural properties of anisotropic composite

elements (SPACE). The aim is to provide a strength assessment for preliminary design studies.

Numerous strength theories have been proposed; the validity of which can only be justified by experiments which are themselves complex and formidable. A comprehensive tabulation of strength theories has been presented in Reference 7. Among the theories proposed is the strength theory in References 8, 9. In this theory, the strength of a fiber-reinforced composite, considered as quasi-homogeneous and anisotropic, is governed by a continuous failure surface of Hill (Ref. 10). Once the failure surface is determined, the strength of the composite body under any type of surface loading can be determined in a straight-forward manner. This appears to be a reasonable approach for composites with elastic perfectly-plastic fibers and matrix.

For most composites there is a vast difference between the strength of the filaments and the strength of the binder, and failures in the binder may be encountered as the maximum stress direction varies from the filament direction. In the simplest case, for example, of a unidirectionally reinforced composite in tension, if the angle between the tensile load and the reinforcement direction is increased gradually from zero to ninety degrees, three primary failure modes can be expected to be encountered: first, at small angles, tensile failure of the filaments; second, at intermediate angles, shear failure in the binder; third, as the filaments become oriented mostly transverse to the load, tensile failure in the binder. These failure modes are essentially independent of one another. Particularly for the change from

tensile failure in the filaments to shear in the binder, there appears to be little reason to expect a gradual transition of the type that leads to a smooth, "yield surface" for homogeneous materials.

When the various failure modes are independent of each other for a composite having an oriented structure, the applicability of a continuous function, like Hill's anisotropic yield condition for a homogeneous material (Ref. 10), to represent a yield or strength criterion appears open to question. Accordingly, the approach utilized herein to determine strength criteria for composite laminates has been to determine separately the strengths for all possible failure modes. Thus, to a degree, a family of failure surfaces representative of the material will be generated, and the lowest of them for any loading condition will be the governing one.

This approach is described in the following sub-section. This is followed by a presentation of the recent studies of the strength properties of a uniaxial laminate. Note that these latter quantities are required both for the discontinuous and the continuous failure surface models. The analysis is developed first for composites where both fiber and matrix are elastic-plastic and a continuous failure surface is defined. These results are then specialized for rigid brittle fibers to generate strength values which can be used in a maximum stress failure theory.

#### Laminate Strength

The strength analysis of a laminate of layers of uniaxial fibrous composites utilizes the elastic analysis, under given surface loadings, of the state of stress in each laminate layer considered as quasi-homogeneous, i. e.

locally heterogeneous, but grossly homogeneous. If the surface loadings increase monotonically and proportionally, there will be a stage at which the stress in one (or more) layers of the laminate is at a failure point and the layer, being assumed to fail, is replaced by a new degraded layer having an assumed mode of degradation. As successive failure of constituting layers proceeds, a redistribution of stress among the laminae occurs and the slope of the load-deflection curve is discontinuous. The ultimate strength of the laminate is reached when all the constituting layers have failed.

In each layer, the stresses referred to the principal axes of anisotropy are computed. If the shear or transverse stress is equal to its corresponding yield stress, the lamina is considered to hold that stress level for those components and to have additional stiffness only in the fiber direction. As successive failure of constituting layers occurs, the entire load-deflection history can be traced until a failure in the fiber direction occurs or until all layers yield, at which point the associated applied load is defined as the failure load. An illustration of the application of this approach is presented in Fig.

1 where calculated stress-strain curves for two simple laminates of E-glass in epoxy are shown. For more general laminate configurations there will be a greater number of straight line sections in the stress-strain curve.

For those applications where only the limiting stress levels - and not the entire stress-strain curve - are required, a simpler approach to the definition of failure criteria appears reasonable. This approach is based upon the concept that the first departure from elastic behavior is a most significant



point on a composite material stress-strain curve. It is desired to keep actual stress levels below this point in a fashion analogous to the use of the yield stress for metal construction. Similarly, at the ultimate stress level, the transverse properties of the individual layers have generally deteriorated. Thus this level can be approximated by using a "netting" analysis with the uniaxial strength properties of the individual layers. The application of these principles in the definition of failure criteria is described below. These methods have been incorporated as a subroutine of the SPACE computer program.

The basic stress strain relations for the laminate are given by:

$$\begin{Bmatrix} N \\ M \end{Bmatrix} = \begin{bmatrix} a & b \\ \text{---} & \text{---} \\ b & d \end{bmatrix} \begin{Bmatrix} \bar{\epsilon}_0 \\ \bar{\kappa} \end{Bmatrix}$$

Where  $N_i$  and  $M_i$  are the laminate stress and moment resultants,  $\bar{\epsilon}_{0i}$  are the middle surface strain components,  $\bar{\kappa}_i$  are the curvatures, and  $a_{ij}$ ,  $b_{ij}$ , and  $d_{ij}$  are the laminate elastic constants obtained by suitable integration of the laminae elastic constants. For definition of laminate strength we desire to treat the stresses arising from a set of applied stress resultants when the curvatures are prevented. Thus we can consider above equation rewritten as:

$$\begin{Bmatrix} \bar{\epsilon}_0 \\ M \end{Bmatrix} = \begin{bmatrix} a^{-1} & -a^{-1}b \\ \text{---} & \text{---} \\ ba^{-1} & d-ba^{-1}b \end{bmatrix} \begin{Bmatrix} N \\ \bar{\kappa} \end{Bmatrix}$$

where  $a^{-1}$  is the inverse of the matrix  $a$ .

For zero curvatures we have

$$\left\{ \begin{matrix} - \\ \epsilon \end{matrix} \right\} = [a]^{-1} \left\{ \begin{matrix} - \\ N \end{matrix} \right\}$$

and

$$\bar{\sigma}_i^{(k)} = \bar{C}_{ij}^{(k)} \bar{\epsilon}_{oj}$$

where  $\bar{\sigma}^{(k)}$  are the stress components in the  $k^{\text{th}}$  layer referred to the laminate axes.

$\bar{C}_{ij}^{(k)}$  are the elastic moduli of the same layer referred to the same axes.

From these equations we may find the stresses,  $\sigma_i^{(k)}$ , referred to the lamina principal axes from:

$$\sigma_i^{(k)} = T_{ij} (\beta^k) \bar{\sigma}_j^{(k)} \quad \text{no sum on } k$$

where  $T$  is the transformation matrix for rotation of coordinate axes.

$\beta^k$  is the angle from laminate principal axes to lamina principal axes.

To evaluate laminate strength, the stress components  $\sigma^k$  are evaluated for a laminate having its laminae thicknesses and the total load normalized. Thus, the total thickness is unity and the load vector for axial load, for example, is (1, 0, 0). With the stress components known, and the maximum strengths,  $\sigma_{iu}^{(k)}$  defined for each of the stress components, (as in Refs. 3, 4, and 5) the ratios

$$\frac{\sigma_{iu}^{(k)}}{\sigma_{iu}^{(k)}}$$

are formed. The lowest ratio of this set of  $3n$  quantities (for an  $n$  layer laminate) is the material yield stress,  $\sigma_y$ .

The same analysis is now repeated for the case where the moduli  $E_2$ ,  $G_{12}$ , and  $\nu_{21}$  are set equal to zero for all layers. Thus only  $E_1$ , the modulus in the fiber direction is non-zero and we have (for  $E_1 = \nu_f E_f$ ), a "netting" analysis. Here there are only  $n$  stress ratios and the lowest one is taken as the material ultimate stress,  $\sigma_u$ .

As an application, the yield stress of a symmetric biaxial laminate subjected to an axial tensile load was treated. The results for these laminates are presented in Fig. 2. Each curve represents the results generated for one of the three stress components and the lower envelope curve is the design yield stress curve.

### Lamina Strength

It has been postulated (Refs. 8 and 9) that the strength of a unidirectional fibrous composite, considered as quasi-homogeneous and anisotropic, can be represented by a surface having the form of Hill's Generalized von Mises' Yield Condition (Ref. 4), namely:

$$2f(\tau_{ij}) = F(\tau_{22} - \tau_{33})^2 + G(\tau_{33} - \tau_{11})^2 + H(\tau_{11} - \tau_{22})^2 + 2L\tau_{23}^2 + 2M\tau_{31}^2 + 2N\tau_{12}^2 = 1 \quad (1)$$

where the coefficients  $F$ ,  $G$ ,  $H$ ,  $L$ ,  $M$ ,  $N$  are parameters characterizing the state of anisotropy and  $\tau_{ij}$  are components of the stress tensor referred to the

principal axes of anisotropy  $x_1, x_2, x_3$  where the  $x_1$  axis is parallel to the fibers.\* In general, the yield condition (1) can be represented by a surface in a stress space. A stress point within the yield surface represents a "safe" stress state. Yielding can occur if the stress point is on the yield surface. Since unidirectional fibrous composite layers in laminates are thin compared with their lateral dimensions, only  $\tau_{11}$ ,  $\tau_{22}$  and  $\tau_{12}$  are considered non-zero if the  $x_3$  axis is along the thickness of the layer. Furthermore, since unidirectional fibers are randomly located in a composite layer, it can be assumed to be transversely isotropic. Then the yield condition (1) reduces to

$$\left(\frac{\tau_{11}}{X_1}\right)^2 + \left(\frac{\tau_{22}}{X_2}\right)^2 + \left(\frac{\tau_{12}}{X_{12}}\right)^2 - \frac{\tau_{11}\tau_{22}}{X_1^2} = 1 \quad (2)$$

where  $X_1$ ,  $X_2$  and  $X_{12}$  are the normal yield stress in the direction of the fibers, the normal yield stress in the direction transverse to the fibers and the yield stress in axial shear of the composite, respectively. These are the three basic strength characteristics of the unidirectional fibrous composites. Once these are known, the yield condition (2) can be employed to determine whether a combined state of (plane) stress can cause failure of the composite.

In what follows, effort is made to evaluate the quantities,  $X_1$ ,  $X_2$  and  $X_{12}$  analytically in terms of the strength and geometry of the constituents.

---

\* Henceforth, unless otherwise specified,  $i, j = 1, 2, 3$ ; Summation on repeated indices is implied.

## Limit Analysis of Unidirectional Fibrous Composites

The composite material under consideration consists of a relatively soft matrix material in which stiffer fibers are embedded. Initially both materials are assumed to be elastic-perfectly plastic and satisfy the von Mises' yield criterion. As shown in Figure 1, referred to an orthogonal Cartesian co-ordinate system, a typical unidirectional fibrous composite is taken to be a cylinder with rectangular cross-section. Circular fibers running from base to base of the specimen are in  $x_1$ -direction. Limit analyses of such a specimen with various arrangements of both elastic brittle and elastic perfectly plastic fibers in an elastic-plastic matrix under various types of surface loading will be described.

### Elastic-plastic Constituents

In this study only the "random array" geometry is considered: circular fibers of various diameters are randomly located in the specimen. Each of them can be surrounded entirely by a concentric cylinder of matrix material. A cylinder consisting of a fiber of radius  $r_f$  and the outer matrix-shell of radius  $r_b$  is called a composite cylinder. It is assumed that a constant  $\beta = \frac{r_f}{r_b}$  can be chosen so that the composite cylinders are non-overlapping. The entire specimen can then be considered as an assemblage of composite cylinders and the remaining matrix volume. The lateral boundary of the specimen may touch or cut through some fibers. In both cases the associated composite cylinders are "incomplete". Since in practice fiber diameters are very small compared with the transverse dimensions of the specimen, the

total number of fibers in the interior of the specimen is much larger than the total number of those possibly on the lateral boundary. Hence, the total volume of "incomplete" composite cylinders is much smaller than that of the "complete" cylinders.

If  $V$ ,  $V_1$  and  $V_2$  denote, respectively, the total volumes of the specimen, the composite cylinders and the remaining matrix in the specimen, the following obvious relation holds:

$$V = V_1 + V_2 \quad (3)$$

In the case where the entire specimen is occupied by composite cylinders,  $V_2 = 0$ . Following Hashin and Rosen (Ref. 11) this distribution is called the "random array".

The von Mises' yield criterion which the fiber and matrix materials are assumed to obey has the following form (Ref. 12):

$$\frac{S_{ij} S_{ij}}{2} \leq k^2 \quad (4)$$

where  $S_{ij}$  are components of the stress deviator and  $k$  is the yield stress in simple shear for the fiber material (denoted by  $k_f$ ) or for the matrix material (denoted by  $k_b$ ).

Under the conditions of plane strain perpendicular to the  $x_1$ -axis, von Mises' yield criterion (4) reduces to

$$\left( \tau_{22} - \tau_{33} \right)^2 + 4 \tau_{23}^2 \leq 4 k^2 \quad (5)$$

where  $\tau_{22}$ ,  $\tau_{33}$  and  $\tau_{23}$  are components of the stress tensor in the transverse plane.

In order to evaluate the three basic strength characteristics (Refs. 8, 9) of the composite specimen shown in Figure 3, the specimen is subjected to axial shear stress  $\tau_{12}$ , transverse tensile stress  $\tau_{22}$  and longitudinal tensile stress  $\tau_{11}$ , respectively. The upper and lower bound theorems of limit analysis of plasticity (Refs. 13, 14) will be used to obtain bounds for the limit loads  $\tau_{12}^L$ ,  $\tau_{12}^L$  and  $\tau_{11}^L$  which represents the lamina strengths.

Case 1. Axial shear stresses  $\tau_{12}$  applied on the boundary of the composite specimen.

According to the lower bound theorem, a uniform shear stress field  $\tau_{12}$  can be chosen as the statically admissible stress field. Since  $\tau_{12}$  can nowhere violate the yield condition (4) for both matrix and fibers, it follows that a lower bound for the limit load  $\tau_{12}^L$  is

$$\left( \tau_{12}^L \right)_L = k_b$$

For upper bound construction, a kinematically admissible velocity field is chosen as follows:

- (a) In  $V_2$  (and thus also on the boundary of the composite cylinders) and on the entire lateral boundary of the specimen,

$$\begin{Bmatrix} u_1 \\ u_2 \\ u_3 \end{Bmatrix} = \begin{Bmatrix} 0 \\ \gamma_1 x_1 \\ 0 \end{Bmatrix} \quad (6)$$

where  $\gamma_1$  is a positive number.

(b) In any composite cylinder, referred to a local cylindrical polar coordinate system, \*

$$\begin{aligned} \begin{pmatrix} u_l \\ u_r \\ u_\theta \end{pmatrix} &= \begin{pmatrix} -\gamma_1 r \cos \theta \\ \gamma_1 x_1 \cos \theta \\ -\gamma_1 x_1 \sin \theta \end{pmatrix} \quad \text{for } 0 \leq r \leq r_f \\ &= \begin{pmatrix} \frac{\gamma_1 \beta^2}{1 - \beta^2} \left(1 - \frac{r_b^2}{r^2} r \cos \theta\right) \\ \gamma_1 x_1 \cos \theta \\ -\gamma_1 x_1 \sin \theta \end{pmatrix} \quad \text{for } r_f \leq r \leq r_b \end{aligned}$$

---

\* The velocity field in any "incomplete" composite cylinder is defined by solving similar elastic displacement boundary value problems for the "incomplete" composite cylinder. However, since the volume of the "incomplete" composite cylinder is small, the difference between their actual contribution to the dissipation function and that obtained by treating all cylinders as "complete" is negligible. This approximation is implied in the subsequent analysis wherever a similar situation arises.



The velocity field (7) in a composite cylinder is the elastic displacement solution to the boundary value problem with the boundary condition (6) prescribed. The problem is the same as that which was formulated by Hashin and Rosen (Ref. 11) with the modification that for  $0 \leq r \leq r_f$ , the velocity field is associated with rigid body motion.

With this velocity field constructed for the entire specimen, the dissipation density function and the rate of external work done can be obtained to yield an upper bound for  $\tau_{12}^L$  (Ref. 5).

$$\frac{(\tau_{12}^L)_U}{k_b} = \frac{1}{\pi(1-\beta^2)} \int_{\beta}^1 \int_0^{2\pi} R \sqrt{\left(1 + \frac{\beta^4}{R^4}\right) + 2 \frac{\beta^2}{R^2} \cos \theta} d\theta dR \quad (8)$$

The above expression is for "random array" in which  $V_2 = 0$  and the fiber volume fraction  $v_f = \beta^2$ .

The integral in (7) is integrated numerically for different fiber-volume fractions. The result is shown in Figure 4 where  $\frac{(\tau_{12}^L)_U}{k_b}$  in (8) is plotted as a function of  $v_f$  ( $0 < v_f < 1$ ,  $v_f = \beta^2$ ). Note that particularly in Figure 4,

$$\lim_{v_f \rightarrow 0} \frac{(\tau_{12}^L)_U}{k_b} = 1,$$

$$\lim_{v_f \rightarrow 1} \frac{(\tau_{12}^L)_U}{k_b} = \frac{4}{\pi}$$

From the above result, it is concluded that  $X_{12}$  is at most about 27% above and at least the same as the yield stress in shear for the matrix.

Case 2. Transverse tensile stresses  $\tau_{22}$  applied on the boundary of the composite specimen.

For lower bound construction, a uniform tensile stress  $\tau_{22}$  throughout the specimen is chosen as a statically admissible stress field. Since the von Mises' yield condition (4) can nowhere be violated in the specimen, the lower bound associated with the constructed statically admissible stress field is

$$\left( \tau_{22} \frac{L}{L} \right)_L = \sqrt{3} k_b \quad (9)$$

For upper bound construction, a kinematically admissible velocity field is chosen as follows:

(a) In  $V_2$  (and thus also on the boundary of the composite cylinders) and on the boundary of the specimen,

$$\begin{Bmatrix} u_1 \\ u_2 \\ u_3 \end{Bmatrix} = \begin{Bmatrix} 0 \\ \frac{\gamma_2}{2} x_2 \\ -\frac{\gamma_2}{2} x_3 \end{Bmatrix} \quad (10)$$

where  $\gamma_2$  is any positive number.

(b) In any composite cylinder, referred to the local coordinate system,

$$\begin{cases} u_1 \\ u_2 \\ u_3 \end{cases} = \begin{cases} \frac{\gamma_2}{2} x_2 \left[ A_1 + A_2 \frac{x_2^2 + 3x_3^2}{2r_f^2} + A_3 \frac{r_f^4 (-x_2^2 + 3x_3^2)}{r^6} + A_4 \frac{r_f^2 (x_2^2 - x_3^2)}{2r^4} \right] \\ -\frac{\gamma_2}{2} x_3 \left[ A_1 + A_2 \frac{3x_2^2 + x_3^2}{2r_f^2} + A_3 \frac{r_f^4 (3x_2^2 - x_3^2)}{r^6} + A_4 \frac{r_f^2 (-x_2^2 + x_3^2)}{2r^4} \right] \end{cases} \left. \begin{array}{l} 0 \\ \text{for } r_f \leq r \leq r_b \end{array} \right\} \quad (11)$$

$$= \begin{cases} \frac{\gamma_2}{2} x_2 B_1 + B_2 \frac{x_2^2 + 3x_3^2}{2r_f^2} \\ -\frac{\gamma_2}{2} x_3 B_1 + B_2 \frac{3x_2^2 + x_3^2}{2r_f^2} \end{cases} \quad \text{for } 0 \leq r \leq r_f$$

where

$$A_1 = \frac{1}{C} \left\{ 4(1-\eta)(1+\eta)\beta^4 - 3(1-\eta)(1+\eta)\beta^2 + \frac{(1+\eta)^2}{\beta^2} \right\}$$

$$A_2 = \frac{1}{C} \left\{ 4(1-\eta)(1+\eta)(1-\beta^2)\beta^2 \right\}$$

$$A_3 = \frac{1}{C} \left\{ (1-\eta) \left[ (1-\eta)\beta^2 + \frac{(1+\eta)}{\beta^2} \right] \right\}$$

$$A_4 = \frac{1}{C} \left\{ 4(1-\eta) \left[ -2\eta + (1+\eta) \left( 1 + \frac{1}{\beta^6} \right) \right] \beta^4 \right\}$$

$$B_1 = \frac{1}{C} \left\{ 8(1-\eta)\beta^4 - 6(1-\eta)\beta^2 + \frac{2(1+\eta)}{\beta^2} \right\}$$

$$B_2 = \frac{1}{C} \left\{ 8(1-\eta)\beta^2(1-\beta^2) \right\}$$

$$\text{and } C = (1-\eta)^2\beta^6 + 4(1-\eta)(1+\eta)\beta^4 - 6(1-\eta)(1+\eta)\beta^2 + 4(1-\eta)(1+\eta) + \frac{(1+\eta)^2}{\beta^2}$$

The velocity field (11) in a composite cylinder is the incompressible elastic displacement solution to the boundary value problem with the boundary condition (10) prescribed. The problem was formulated by Hashin and Rosen (Ref. 11) in evaluating the effective plane strain shear modulus of elastic fiber-reinforced composites. The constant  $\eta$  in (11) considered as the displacement solution to the elastic problem is the ratio of the elastic shear moduli of the fiber and matrix materials. However, it can be considered as merely a parameter when (11) is used as a kinematically admissible velocity.

For the case of the "random array", an application of the upper theorem gives an upper bound

$$\frac{(\tau_{22}^L)_U}{2 k_b} = \frac{k_f}{k_b} I_1 + I_2 \quad (12)$$

where

$$I_1 = 2 \int_0^{\beta} R \left| \frac{8(1-\eta) \beta^4 - 6(1-\eta) \beta^2 + \frac{2(1+\eta)}{\beta^2} + 12(1-\eta)(1-\beta^2) R^2}{C} \right| dR$$

and

$$I_2 = \frac{1}{\pi} \int_{\beta}^1 \int_0^{2\pi} \frac{R}{C} \sqrt{\bar{\Phi}_1(\eta, \beta, R) + \bar{\Phi}_2(\eta, \beta, R) \cos \theta} \cdot d\theta dR$$

in which

$$\begin{aligned} \bar{\Phi}_1(\eta, \beta, R) = & \left\{ 4(1-\eta)(1+\eta) \beta^4 - 3(1-\eta)(1+\eta) \beta^2 + \frac{(1+\eta)^2}{\beta^2} + 6(1-\eta)(1+\eta)(1-\beta^2) R^2 \right\}^2 \\ & + \frac{(1-\eta)^2 \beta^8}{R^4} \left\{ -\frac{3}{R^2} \left[ \frac{(1+\eta)}{\beta^2} + (1-\eta) \beta^2 \right] + 2\beta^2 \left[ -2\eta + (1+\eta) \left( 1 + \frac{1}{\beta^6} \right) \right] \right\}^2 \end{aligned}$$

$$\bar{\sigma}_2(\eta, \beta, R) = 2 \left\{ 4(1-\eta)(1+\eta) \beta^4 - 3(1-\eta)(1+\eta) \beta^2 + \frac{(1+\eta)}{\beta^2} + 6(1-\eta)(1+\eta)(1-\beta^2)R^2 \right\} \\ \left\{ \frac{(1-\eta) \beta^4}{R^2} - \frac{3}{R^2} \left[ \frac{(1-\eta)}{\beta^2} + (1-\eta) \beta^2 \right] + 2\beta^2 \left[ -2\eta + (1+\eta) \left( 1 + \frac{1}{\beta^6} \right) \right] \right\}$$

and  $\beta^2 = v_f$ .

For any finite  $k_f/k_b$  and for  $\eta \rightarrow \infty$ , (12) becomes

$$\frac{(\tau_{22}^L)_v}{2 k_b} = \frac{2}{\pi(1-\beta^2)^3} \int_{\beta}^1 \int_0^{2\pi} R \sqrt{\Psi_1(\beta, R) + \Psi_2(\beta, R) \cos \theta} d\theta dR \quad (13)$$

where

$$\Psi_1(\beta, R) = \frac{\beta^4}{R^4} \left[ (\beta^4 + \beta^2 + 1) - \frac{3}{2} (\beta^2 + 1) \frac{\beta^2}{R^2} \right]^2 + \left[ \frac{(4\beta^4 + \beta^2 + 1)}{2} + 3 \beta^2 R^2 \right]^2$$

and

$$\Psi_2(\beta, R) = 2 \frac{\beta^2}{R^2} \left[ (\beta^4 + \beta^2 + 1) - \frac{3}{2} (\beta^2 + 1) \frac{\beta^2}{R^2} \right] \cdot \left[ \frac{(4\beta^4 + \beta^2 + 1)}{2} + 3 \beta^2 R^2 \right]$$

The right hand side of expression (13) was obtained in Ref. 5 for

an upper bound of the limit load (normalized with respect to  $k_b$ ) for transverse

shear stresses applied on composites reinforced with rigid fibers. In Figure

5,  $\frac{(\tau_{22}^L)_v}{2 k_b}$  is plotted as a function of  $v_f$  according to (13). It is a monotonically increasing function of  $v_f$  with  $\lim_{v_f \rightarrow 0} \frac{(\tau_{22}^L)_v}{2 k_b} U = 1$  and  $\lim_{v_f \rightarrow 1} \frac{(\tau_{22}^L)_v}{2 k_b} U = \infty$ .

On the other hand, for any finite  $\eta$ ,  $\frac{(\tau_{22}^L)_U}{2 k_b}$  can be plotted as a function of

by evaluating numerically  $I_1$  and  $I_2$  in (12). For example, for  $\eta = 100$ ,  $\frac{(\tau_{22}^L)_U}{2 k_b}$

is also a monotonically increasing function of  $v_f$   $\left( \lim_{v_f \rightarrow 0} \frac{(\tau_{22}^L)}{2k_b} U = 1 \right)$  and  $\lim_{v_f \rightarrow 1} \left( \frac{(\tau_{22}^L)}{2k_b} U = \frac{k_f}{k_b} \right)$ , which is shown in Figure 3, with  $\frac{k_f}{k_b} = 10$ . It is observed that for fiber volume fractions smaller than about 75%, the upper bound for the limit load  $\tau_{22}^L$  is higher than for  $\eta \rightarrow \infty$  but for higher fiber volume fraction, the opposite is true. Therefore, for any fiber volume fraction between 0 and 1, the lower value of the bounds obtained from  $\eta = 100$  and  $\eta \rightarrow \infty$  will give a better estimate of  $\tau_{22}^L$  and it is shown in Figure 5 in solid line as a function of  $v_f$ .

It is interesting to note that for  $\eta = 1$ , (12) reduces to the following simple form

$$\frac{(\tau_{22}^L)}{2k_b} = 1 + v_f \left( \frac{k_f}{k_b} - 1 \right) \quad (14)$$

which is commonly known as the "rule of mixtures". From Figure 3, it is seen that the straight line represented by (14) will be higher than the chosen curve for  $\frac{(\tau_{22}^L)}{2k_b} U$  for  $0 < v_f < 1$ . Therefore, it is concluded that the "rule of mixtures" to be used in this case would overestimate the composite strength.

In Figure 5,  $\frac{(\tau_{22}^L)}{2k_b} L$  obtained from (9) is also shown. The difference between the upper and lower bounds for  $v_f \rightarrow 0$  is due to the fact that in the upper bound construction, a plane strain velocity field is used as a kinematically admissible velocity field.

Case 3. Longitudinal tensile stresses  $\tau_{11}$  applied on the boundary of the composite specimen.

The study of longitudinal strength of unidirectional fibrous composites is extensive. Various models and failure mechanisms have been proposed in the literature. Here, the yield strength in axial tension is obtained by the construction of very simple velocity and stress fields, for composites having elastic-plastic fibers of uniform strength.

For upper bound construction, in the entire region of the composite specimen, a kinematically admissible velocity field is chosen as

$$\begin{Bmatrix} u_1 \\ u_2 \\ u_3 \end{Bmatrix} = \begin{Bmatrix} \epsilon_0 x_1 \\ \frac{\epsilon_0}{2} x_2 \\ -\frac{\epsilon_0}{2} x_3 \end{Bmatrix}$$

An application of the upper bound theorem gives

$$\left( \tau_{11}^L \right) = \tau_f v_f + \tau_b v_b \quad (15)$$

or

$$\left( \frac{\tau_{11}^L}{\tau_b} \right) = 1 + v_f \left( \frac{\tau_f}{\tau_b} - 1 \right)$$

where  $\tau_f$  and  $\tau_b$  are the yield stresses in tension for the fiber and matrix, respectively and  $v_b = 1 - v_f$ .

Relation (15) is known as the "rule of mixtures" for the predication of the strength of a composite. If  $\tau_f$  and  $\tau_b$  are given,  $\left( \frac{\tau_{11}^L}{\tau_b} \right) U$  is a linear function of fiber-volume fraction  $v_f$ .

For lower bound construction, if the applied stress  $\tau_{11}$  is assumed to be uniformly distributed on the boundary of the composite specimen, then a lower bound  $(\tau_{11}^L)_L$  is equal to  $\tau_b$ . However, if we assume that the tensile stress  $\tau_{11}$  is not uniformly distributed on the boundary surface and we are only interested in the average stress intensity on the boundary surface that causes failure, then a higher lower bound can be obtained. In fact, a statically admissible stress field can be chosen as follows:

In the region occupied by fibers

$$\tau_{ij} = \begin{bmatrix} \tau_f & 0 & 0 \\ 0 & 0 & 0 \\ 0 & 0 & 0 \end{bmatrix} \quad (16)$$

In the region occupied by the matrix,

$$\tau_{ij} = \begin{bmatrix} \tau_b & 0 & 0 \\ 0 & 0 & 0 \\ 0 & 0 & 0 \end{bmatrix} \quad (17)$$

It is obvious that the stress field expressed in (16) and (17) satisfy the requirements to be statically admissible.

The average traction corresponding to this stress field is therefore

$$\tau_f v_f + \tau_b v_b \quad (18)$$

which can be taken as  $(\tau_{11}^L)_L$ .

According to (15) and (18), the upper and lower bounds for  $\tau_{11}^L$  coincide. Therefore, this strength can be determined from the "rule of mixtures", for



this type of composite, (i. e. elastic-plastic fibers and matrix of uniform yield strength).

From the above results, it is observed that bounds for  $\tau_{22}^L$  are far apart, especially for high volume fractions. Further effort should be made to improve the bounds in order to have a better estimate of the limit load. For lower bound construction, uniform stress distribution used as statically admissible stress fields can only give lower bounds which are the corresponding matrix yield stresses. In order to obtain higher lower bounds, one has to assume applied tractions to be non-uniformly distributed on the boundary surface according to the properties of the fibers and matrix. Equilibrium stress fields can then be constructed in equilibrium with the applied tractions. Then the lower bound theorem can be applied to obtain higher lower bounds. To decide the distribution of the applied tractions on the boundary and to construct an equilibrium stress field in the body is not at all easy in general. The success in the construction of such a statically admissible stress field for Case 3 is due to the simplicity of geometry and loading conditions.

#### Brittle Fibers

In the previous section, the strength of unidirectional fibrous composites has been evaluated by obtaining bounds for the basic strength characteristics. The theory assumes the existence of a continuous failure surface. This hypothesis appears reasonable for composites with elastic-perfectly plastic fibers and matrix such as metal fibers and matrix. However, for contemporary high strength fibers embedded in epoxy resin matrix, this "elastic-perfectly

plastic model" may seem inadequate. Instead, it seems more suitable to assume elastic-brittle fibers and an elastic-perfectly plastic matrix which obeys the von Mises' yield criterion. Upper and lower bounds have been obtained for the following types of surface loadings:

1. Tractions equivalent to a uniform shear stress  $\tau_{12}$  applied on the entire boundary surface of the specimen.
2. Tractions equivalent to a uniform shear stress  $\tau_{23}$  applied on the entire boundary surface under the conditions of plane strain.
3. Tractions equivalent to uniform uniaxial tension  $\tau_{22}$  applied on the entire boundary surface under the conditions of plane strain.
4. Tractions equivalent to biaxial uniform tension  $\tau_{22}$  and  $\tau_{33}$  ( $\tau_{22} \neq \tau_{33}$ ) applied on the entire boundary surface under the conditions of plane strain.
5. Tractions equivalent to combined in-plane shear  $\tau_{12}$  and transverse tension  $\tau_{22}$  ( $\tau_{11} = \alpha \geq 0$ ) applied on the entire boundary surface.

Since the method of analysis is similar to what has been presented in the preceding pages in obtaining bounds for the basic strength characteristics, the details of analysis will be presented in Appendix A. However, results are summarized as follows:

$$1. \quad \left( \tau_{12} \right)_L = k_b.$$

$$\frac{\left( \tau_{12} \right)_U}{k_b} = \frac{1}{\pi (1-\beta^2)} \int_{\beta}^1 \int_0^{2\pi} R \sqrt{\frac{(1+\beta^4)}{R^4} + 2 \frac{\beta^2}{R^2} \cos \theta} \, d\theta \, dR$$

for the "random array" geometry. The above expression for  $\frac{(\tau_{12}^L)}{k_b} U$  is the same as (8) which is shown in Figure 4 as a function of  $v_f$  ( $0 < v_f < 1$ ,  $v_f = \beta^2$ ) since the same velocity is used here.

For arbitrary geometry of arrangement of fibers,  $\frac{(\tau_{12}^L)}{k_b} U = 1 + \left(\frac{\pi}{2} - 1\right) v_f$

which is higher than  $\frac{(\tau_{12}^L)}{k_b} U$  given by (8).

$$2. \quad \left(\tau_{23}^L\right)_L = k_b.$$

$$\frac{(\tau_{23}^L)}{k_b} U = \frac{2}{\pi(1-\beta^2)^3} \int_{\beta}^1 \int_0^{2\pi} \sqrt{\Psi_1(\beta, R) + \Psi_2(\beta, R) \cos \theta} d\theta dR$$

where

$$\Psi_1(\beta, R) = \frac{\beta^4}{R^4} \left[ \left( \beta^4 + \beta^2 + 1 \right) - \frac{3}{2} (\beta^2 + 1) \frac{\beta^2}{R^2} \right]^2 + \left[ -\frac{(4\beta^4 + \beta^2 + 1)}{2} + 3\beta^2 R^2 \right]^2$$

$$\text{and } \Psi_2(\beta, R) = \frac{2\beta^2}{R^2} \left[ \beta^4 + \beta^2 + 1 - \frac{3}{2} (\beta^2 + 1) \frac{\beta^2}{R^2} \right] \left[ -\frac{(4\beta^4 + \beta^2 + 1)}{2} + 3\beta^2 R^2 \right]$$

for the "random array" geometry. The above expression for  $\frac{(\tau_{23}^L)}{k_b} U$  is the same as (13) which is plotted in Figure 5, as a function of  $v_f$  with

$$\lim_{v_f \rightarrow 0} \frac{(\tau_{23}^L)}{k_b} U = 1 \quad \text{and} \quad \lim_{v_f \rightarrow 1} \frac{(\tau_{23}^L)}{k_b} U = 1.5$$

since the velocity field chosen here can be obtained from (10) and (11) through an orthogonal transformation together with the limiting process of  $\eta \rightarrow \infty$

$$3. \quad (\tau_{22}^L)_L = 2k_b$$

$$(\tau_{22}^L)_U = 2 \tau_{23}^L U$$

$$4. \quad (\tau_{22}^L)_U - (\tau_{33}^L)_U = 2k_b.$$

$$(\tau_{22}^L)_U - (\tau_{33}^L)_U = 2 (\tau_{23}^L)_U$$

$$5. \quad \frac{(\tau_{22}^L)_L}{k_b} = \frac{1}{\sqrt{\frac{1}{3} + \alpha^2}}$$

$$\text{and} \quad \frac{(\tau_{12}^L)_L}{k_b} = \frac{\alpha}{\sqrt{\frac{1}{3} + \alpha^2}} \quad (19)$$

for  $\alpha \gg 0$ .

For the case of the "random array" geometry,

$$\frac{(\tau_{22}^L)_U}{k_b} = \min_{\{\omega\}} \frac{I_3}{\frac{1}{2} + \alpha \omega} \quad (20)$$

$$\text{and} \quad \frac{(\tau_{12}^L)_U}{k_b} = \min_{\{\omega\}} \frac{\alpha I_3}{\frac{1}{2} + \alpha \omega}.$$

where

$$I_3 = \frac{1}{\pi(1-\beta^2)^3} \int_{\beta}^1 \int_0^{2\pi} R \sqrt{\Omega_1(\omega, \beta, R) + \Omega_2(\omega, \beta, R) \cos \theta + \Omega_3(\beta, R) \cos^2 \theta} \\ \Omega_1(\omega, \beta, k) = 4 \left\{ \frac{\beta^4}{R^4} \left[ (\beta^4 + \beta^3 + 1) - \frac{3}{2} (\beta^2 + 1) - \frac{3}{2} (\beta^2 + 1) \frac{\beta^2}{R^2} \right]^2 \right. \\ \left. + \left[ 3\beta^2 R^2 - \frac{(4\beta^4 + \beta^2 + 1)}{2} \right]^2 \right\} + \omega^2 (1-\beta^2)^4 \left( 1 + \frac{\beta^4}{R^4} \right) \\ \Omega_2(\omega, \beta, R) = 2 \omega^2 (1-\beta^2)^4 \frac{\beta^2}{R^2}$$

$$\text{and } \Omega_3(\beta, R) = 8 \frac{\beta^2}{R^2} \left[ (\beta^4 + \beta^2 + 1) - \frac{3}{2} (\beta^2 + 1) \frac{\beta^2}{R^2} \right] \left[ 3\beta^2 R^2 - \frac{(4\beta^4 + \beta^2 + 1)}{2} \right]$$

Numerical calculation is performed to obtain  $(\tau_{22}^L)_U$  and  $(\tau_{12}^L)_U$  from (20) for different values of  $\beta$  and  $\alpha$ . The results are summarized in Figure 6 in which  $\beta^2 = 0.8$  is the highest fiber volume fraction shown. The dotted line represents (19) which gives the lower bound for  $(\tau_{22}^L)$  and  $(\tau_{12}^L)$  for any  $\beta$ .

It is worth mentioning that for this model of elastic-brittle fibers embedded in elastic-perfectly plastic matrix, in the upper bound expressions, only the matrix strength and fiber-volume fraction appear - the brittle strength of the fibers is not involved. This is due to the fact that rigid body motion of fibers is always incorporated into the kinematically admissible fields. Hence, regions occupied by fibers in the composite body contribute nothing to the dissipation function. The result is reasonable since in reality, elastic moduli and brittle strength of fibers are much higher than the corresponding elastic moduli and

strength of the matrix material. On the other hand, the longitudinal strength along fiber-direction of fibrous composites under tension or compression cannot be obtained by limit analysis of plasticity because of the presence of the high modulus, high strength elastic-brittle fibers. Instead, a statistical failure theory was established for tensile strength [3] and a fiber-buckling model was postulated for compressive strength of fibrous composites [4] and [15]. These failure mechanisms are based on experimental observation. Furthermore, as mentioned previously, for this mathematical model of composite material, the existence of a smooth yield surface that governs the strength of the material is still an open question. Based on experimental investigation, the failure mechanisms for individual cases seem to be different and independent of one another. Accordingly, the approach to the determination of the strength criterion for unidirectional fiber-reinforced composites as well as fibrous composite laminates is as described earlier. Instead of using a continuous yield surface, all possible failure modes are considered. To determine which one is dominant for a particular type of loading condition can sometimes become a tedious task especially for fibrous laminates under various types of design loading. However, this approach has the advantage that the entire load-deflection history can be traced until complete failure occurs. With modern high speed digital computers available, a systematic strength analysis can be programmed to obtain accurate results.

For certain composites, it is possible to utilize, as an alternate approach, the application of limit analysis methods to the laminate as a whole. This is treated in the following section.

### Application to Laminates

It is interesting to note that the kinematically admissible velocity fields constructed to evaluate the upper bound for the three basic strength characteristics can be used to obtain upper bounds of limit loads for in-plane loading applied on laminates.

To demonstrate the method, consider a laminate composed of uni-directional fibrous laminae subjected to in-plane shear stress  $\tau_{12}$ . The problem is to find an upper bound for the limit load  $\tau_{12}^L$ . A typical constituting layer, the  $k^{\text{th}}$  layer, in which fibers are all running in  $\bar{x}_1^{(k)}$  direction, is shown in Figure 7. Depending on the orientation of fibers in the layer, the principal axes  $\bar{x}_1^{(k)} \bar{x}_2^{(k)} x_3$  can be defined by an angle  $\theta^{(k)}$  measured from the laminate axes  $x_1 x_2 x_3$ .

For upper bound construction, a kinematically admissible velocity field is constructed in the following manner:

The velocity field  $(\mu_1, \mu_2, \mu_3) = (0, \gamma_1 x_1, 0)$  is assigned in  $V_2$  of each layer, referred to  $x_1 x_2 x_3$  axes. In the  $k^{\text{th}}$  layer referred to its principal axes  $\bar{x}_1^{(k)} \bar{x}_2^{(k)} x_3$ , the above velocity field is transformed into the following form:

$$\left\{ \begin{array}{l} \bar{\mu}_1^{(k)} \\ \bar{\mu}_2^{(k)} \\ \bar{\mu}_3^{(k)} \end{array} \right\} = \left\{ \begin{array}{l} \gamma_1 \sin \theta^{(k)} \cos \theta^{(k)} x_1^{(k)} = \gamma_1 \sin^2 \theta^{(k)} x_2^{(k)} \\ \gamma_1 \cos^2 \theta^{(k)} x_1^{(k)} - \gamma_1 \sin \theta^{(k)} \cos \theta^{(k)} x_2^{(k)} \\ 0 \end{array} \right\} \quad (21)$$

The right hand side of equation (21) can be decomposed into four parts so that

$$\vec{\mu}(k) = \vec{\mu}_1(k) + \vec{\mu}_2(k) + \vec{\mu}_3(k) + \vec{\mu}_4(k) \quad (22)$$

where

$$\vec{\mu}_1(k) \equiv \begin{Bmatrix} 0 \\ \gamma_1 \cos^2 \theta(k) x_1(k) \\ 0 \end{Bmatrix}$$

$$\vec{\mu}_2(k) \equiv \begin{Bmatrix} 0 \\ -\frac{\gamma_1}{2} \sin \theta(k) \cos \theta(k) x_2(k) \\ \frac{\gamma_1}{2} \sin \theta(k) \cos \theta(k) x_3(k) \end{Bmatrix}$$

$$\vec{\mu}_3(k) \equiv \begin{Bmatrix} \gamma_1 \sin \theta(k) \cos \theta(k) x_1(k) \\ -\frac{\gamma_1}{2} \sin \theta(k) \cos \theta(k) x_2(k) \\ -\frac{\gamma_1}{2} \sin \theta(k) \cos \theta(k) x_3(k) \end{Bmatrix}$$

and

$$\vec{\mu}_4(k) \equiv \begin{Bmatrix} -\gamma_1 \sin^2 \theta(k) x_2(k) \\ 0 \\ 0 \end{Bmatrix}$$

Except for multiplicate factors and reference coordinate system,

$\vec{u}_1(k)$ ,  $\vec{u}_2(k)$ , and  $\vec{u}_3(k)$  are the same as those velocity fields constructed in  $V_2$  for the three different cases of loading in the preceding section.

Furthermore.



$$\vec{u}_4^{(k)} = \begin{Bmatrix} -\gamma_1 \sin^2 \theta^{(k)} x_2^{(k)} \\ 0 \\ 0 \end{Bmatrix} = \begin{Bmatrix} 0 \\ -\gamma_1 \sin^2 \theta^{(k)} x_1^{(k)} \\ 0 \end{Bmatrix} + \begin{Bmatrix} -\gamma_1 \sin^2 \theta^{(k)} x_2^{(k)} \\ \gamma_1 \sin^2 \theta^{(k)} x_1^{(k)} \\ 0 \end{Bmatrix} \quad (23)$$

where the first part of the decomposition has the same form as  $\vec{u}_1^{(k)}$  while the second part represents a rigid body motion of  $V_2$  as a whole.

The velocity field chosen in  $V_1$  is also composed of four parts: The first part is due to  $\vec{u}_1^{(k)}$ , which is the same as (7) with the modification that  $\gamma_1 \cos^2 \theta^{(k)}$ . The second part is due to  $\vec{u}_2^{(k)}$  which is the same as (11) with the modification that  $\gamma_2$  is now replaced by  $-\gamma_1 \sin \theta^{(k)} \cos \theta^{(k)}$ . The third part is due to  $\vec{u}_3^{(k)}$  which is exactly the same as  $\vec{u}_3^{(k)}$  in  $V_2$ . The fourth part is due to  $\vec{u}_4^{(k)}$  which can be obtained in the same way as in Case 1 in the preceding section. However, a moment's reflection reveals that the strain rate associated with  $\vec{u}_4^{(k)}$  if  $\gamma_1 \cos^2 \theta^{(k)}$  is replaced by  $-\gamma_1 \sin^2 \theta^{(k)}$  since the additional rigid body motion contributes nothing to the value of the strain rate. Now, after the kinematically admissible velocity field is constructed as described above, the associated strain rate and dissipation density function can be calculated without difficulty. Moreover, the rate of external work done can also be calculated so that an upper bound for  $\tau_{12}^L$  can be obtained.

As an example, consider a laminate composed of two unidirectional fibrous composite layers of equal thickness with  $\theta^{(1)} = 0$  and  $\theta^{(2)} = -\frac{\pi}{2}$ .

In this simple geometry of lamination, the kinematically admissible velocity field constructed above reduces to a very simple form.

For layer 1, the velocity field (21) reduces to

$$\begin{Bmatrix} \bar{\mu}_1^{(1)} \\ \bar{\mu}_2^{(1)} \\ \bar{\mu}_3^{(1)} \end{Bmatrix} = \begin{Bmatrix} 0 \\ \gamma_1' \bar{x}_1^{(1)} \\ 0 \end{Bmatrix} \quad \text{in } V_2 \quad (24)$$

For layer 2, the velocity field (21) reduces to

$$\begin{Bmatrix} \bar{\mu}_1^{(2)} \\ \bar{\mu}_2^{(2)} \\ \bar{\mu}_3^{(2)} \end{Bmatrix} = \begin{Bmatrix} -\gamma_1' \bar{x}_2^{(2)} \\ 0 \\ 0 \end{Bmatrix} \quad \text{in } V_2 \quad (25)$$

Then, following the principles described above, it is easy to obtain the velocity fields and the associated strain rate fields for both layers. After some manipulation, it turns out that

$$\frac{(\tau_{12}^L)_U}{k_b} = \frac{1}{\pi(1-\beta^2)} \int_{\beta}^1 \int_0^{2\pi} R \sqrt{\left(1 + \frac{\beta^4}{R^4} + 2 \frac{\beta^2}{R^2} \cos \theta\right)} d\theta dR$$

for the "random array" geometry.

The above equation is exactly (8), which means that the upper bound  $(\tau_{12}^L)_U$  is not higher for this type of cross-ply laminates than for the uni-directional fibrous composite.

Similarly, it is easy to show that the three types of velocity fields constructed in the preceding section can be used to construct upper bounds for limit loads for laminates subjected to any in-plane stresses.

## Tensile Strength

The high-strength, high modulus fibers which are of interest for use in composite materials are generally brittle, having tensile strengths that must be characterized statistically. Any theory for the tensile strength of composites containing such fibers must take into account the dispersion in their failure stress levels in order to have any relevance.

(16)  
Parratt noted the dispersion in fiber strength and suggested that failure of a fibrous composite subjected to tensile load occurs when the fibers have broken up into lengths so short that any increase in applied load cannot be transmitted to the fibers because the limit of interface or matrix shear has been reached.

A theory has been presented (3) for the failure stress of composites containing continuous, uniaxially-oriented, brittle fibers in a ductile matrix loaded parallel to the fiber direction. This theory predicts that due to the distribution of flaws or imperfections in the fibers there occurs a series of randomly-distributed fiber fractures as the applied stress level is increased.

It is argued that a portion of the broken fiber in the vicinity of the fracture is ineffective in resisting the applied load. Assuming that the stress in a broken fiber is uniformly distributed among the unbroken fibers in the cross-section and that this overstress acts over a length equal to the "ineffective" length, it is predicted that failure occurs when a weakened cross-section cannot sustain an increase in load. In effect, the theory pre-

dicts that the composite has a strength equal to that of a bundle of fibers whose length is the "ineffective" length.

The present study considers fibers having a statistical strength distribution resulting in fractures at various stress levels as the applied load increases. It is assumed that the stress in the broken fiber is distributed unevenly to the other fibers in the cross-section which has a length equal to the ineffective length. As a first approximation the effect of this overstress is presumed to affect only those fibers adjacent to a break. Failure is assumed to occur due to an increasing probability of fracture in the fibers adjacent to a prior break.

#### Description of the Model

The model consists of a two-dimensional composite of length  $L$  consisting of a ductile matrix in which are imbedded  $N$  continuous brittle fibers whose orientation is parallel to the applied tensile load. The fibers are considered to be composed of layers of length  $\delta$ . The total number of layers being  $M = L/\delta$ . (See Figure 8.)

The quantity  $\delta$  represents some length over which the stress is perturbed in the area of a fracture. It is variously referred to as the ineffective length or twice the transfer length and several formulae have been proposed for its evaluation. Two of the definitions(3), (17) are based on an elastic shear-lag type of analysis. The axial stress in a broken fiber is found to be

$$\sigma_f(x) = \sigma_0 [1 + \sinh \eta x - \cosh \eta x] \quad (1)$$

where

$$\eta^2 = 2 \frac{G_b}{E_f} \frac{v_f^{1/2}}{1-v_f^{1/2}} \frac{1}{r_f^2}$$

$E_f$  = Young's modulus of fiber

$G_b$  = Shear modulus of binder (matrix)

$r_f$  = Fiber radius

$v_f$  = Volume fraction of fibers

$x$  = Distance from end of broken fiber

$\sigma_0$  = Extensional stress in the fiber at a large distance from the fiber end.

It should be noted that in Reference 3 the factor of 2 in the expression for  $\eta$  was incorrectly omitted. The first author defines  $\delta$  as the value of  $x$  for which the stress in the fiber has reached 90% of  $\sigma_0$ , the stress at a long distance from the fiber break. On the other hand, Friedman defines the ineffective length by means of an approximate step-function stress distribution which has the same average stress as the distribution of Equation 1. Furthermore, this author includes the ineffective portion on both sides of the break whereas the first definition uses only one side.

The expressions for the two ineffective lengths discussed above are, respectively

$$\frac{\delta_R}{d_f} = 1.15 \left[ \frac{1}{2} \frac{E_f}{G_b} \frac{1-v_f^{1/2}}{v_f^{1/2}} \right]^{1/2} \quad (2)$$

$$\frac{\delta_F}{d_f} = \left[ \frac{1}{2} \frac{E_f}{G_b} \frac{1-v_f^{1/2}}{v_f^{1/2}} \right]^{1/2} \quad (3)$$

If the shear stress between the matrix and fiber is assumed to be constant, as in the case of plastic flow or frictional shear stress due to interface failure, the fiber tensile stress becomes constant at a finite distance from the fiber end. This distance is called the transfer length  $l_t$  by some authors and is given by the expression

$$l_t = \frac{\sigma_0 r_f}{2\tau}$$

where  $\tau$  is the (constant) plastic shear stress of the matrix, or, if there is interface failure, the frictional force between the matrix and fiber.

The ineffective length can also be determined experimentally by a photoelastic examination of the stress patterns in the vicinity of a fiber break. In this investigation the experimentally determined ineffective length is used where available.

#### Statistical Analysis of the Model

It is assumed that the strength of the population of fiber elements of length  $\delta$  can be characterized by a cumulative distribution function  $F(\sigma)$ . That

is, the probability that an arbitrary element has a failure stress level less than, or equal to  $\sigma$  is  $F(\sigma)$ .

The expected number of elements in the composite that will fail under fiber stress  $\sigma$  is

$$E = MNF(\sigma) \dots \quad (4)$$

This expression includes the possibility of further fractures of adjacent fibers. If the composite does not fail, the stress in the broken fibers is distributed to the other fibers in the cross-section in a complex manner. As a first approximation, Hedgepeth<sup>(18)</sup> used a shear lag analysis to determine the average stresses in fibers adjacent to an arbitrary number of broken fibers. He considers an infinite two-dimensional array of fibers subjected to tensile load parallel to the fiber direction which is uniform at a great distance from the fracture area. The ratio of stress in the two fibers adjacent to a run of  $r$  broken fibers to the uniform applied stress at infinity is, for a static stress distribution

$$K_r = \frac{4 \cdot 6 \cdot 8 \cdots (2r+2)}{3 \cdot 5 \cdot 7 \cdots (2r+1)} \quad (5)$$

Hedgepeth calls  $K_r$  a stress-concentration factor, but in this paper it will be referred to as an overstress-factor so that it will not be confused with stress concentration factors found by an "exact" analysis of the stress distribution.

For the case where  $r$  fibers break simultaneously the author demonstrated that the ratio of the maximum dynamic stress to the static stress in

the fibers adjacent to the break increases from 1.15 for  $r = 1$  to a limit of 1.27. The values for  $r = 2$  and  $r = 3$  are 1.19 and 1.20 respectively.

In the present paper it is assumed that the overstress in two fibers adjacent to the broken ones exists over the entire ineffective length. Therefore, the probability that an element adjacent to  $r$  broken elements will fail is, approximately, the probability that its strength lies between  $\sigma$  and  $K_r \sigma$ . This probability is equal to

$$F(K_r \sigma) - F(\sigma) \quad (6)$$

This approximation is justified, as will be shown later, by the fact that composite failure occurs for small values of  $F(\sigma)$  and therefore the probability of having adjacent fractures because both fibers have strength less than  $\sigma$ , which probability is proportional to  $F(\sigma)^2$ , and the probability of interaction of fracture groups is relatively small.

Given that a single element is broken the probability that one of the two adjacent fibers will break is

$$P_{2/1} = 2 [F(K_1 \sigma) - F(\sigma)] - 2 [F(K_1 \sigma) - F(\sigma)]^2 \quad (7)$$

The probability that both adjacent fibers will break simultaneously is

$$P_{3/1} = [F(K_1 \sigma) - F(\sigma)]^2 \quad (8)$$

It should be noted that each of these expressions does not exclude the possibility of further fractures.



It is now assumed that only the two fibers immediately adjacent to a break are subjected to an overstress and that all of the remaining fibers in the cross-section have a stress level equal to the average stress  $\sigma$ . If one of the fibers adjacent to a single fracture breaks the fibers adjacent to the two broken fibers are subjected to a stress level  $K_2\sigma$ . One of these overstressed fibers was previously exposed to a stress level  $K_1\sigma$  while the other saw only the average stress  $\sigma$ . The probability that one of the two fibers will break is

$$p_{3/2} = [F(K_2\sigma) - F(K_1\sigma)] + [F(K_2\sigma) - F(\sigma)] - 2 [F(K_2\sigma) - F(K_1\sigma)] [F(K_2\sigma) - F(\sigma)]. \quad (9)$$

The probability that both fibers will break simultaneously is

$$p_{4/2} = [F(K_2\sigma) - F(K_1\sigma)] [F(K_2\sigma) - F(\sigma)] \quad (10)$$

If both fibers adjacent to an initial fracture break there will be three broken fibers in a row and therefore the two fibers adjacent to this group, which were previously at a stress level  $\sigma$ , will be subjected to a stress  $K_3\sigma$ . Again it is possible for one or two of these fibers to break, and so on.

By now the process and complexity of the problem should be evident so that the expressions for further fracture probabilities are presented without discussion. Note that there are two paths by which a state of three broken fibers can be reached from a single break; A) by the simultaneous

breaking of both fibers adjacent to the initial break, B) by the successive breaking of two fibers.

The expression  $p_{i/jz}$  represents the probability of having  $i$  fibers broken given that  $j$  are already broken. The letter  $z$  represents the particular path if there is more than one. The letters  $A$  and  $B$  refer to the paths described above.

$$\begin{aligned}
 p_{4/3A} &= 2 \left[ F(K_3\sigma) - F(\sigma) \right] - 2 \left[ F(K_3\sigma) - F(\sigma) \right]^2 \\
 p_{5/3A} &= \left[ F(K_3\sigma) - F(\sigma) \right]^2 \quad (11a-d) \\
 p_{4/3B} &= \left[ F(K_3\sigma) - F(K_2\sigma) \right] + \left[ F(K_3\sigma) - F(\sigma) \right] - \\
 &\quad 2 \left[ F(K_3\sigma) - F(K_2\sigma) \right] \left[ F(K_3\sigma) - F(\sigma) \right] \\
 p_{5/3B} &= \left[ F(K_3\sigma) - F(K_2\sigma) \right] \left[ F(K_3\sigma) - F(\sigma) \right]
 \end{aligned}$$

#### Probability of Cumulative Fractures

Each of the  $E_1$  fracture sites distributed throughout the composite is a nucleus for further fiber breaks because of the overstress in adjacent fibers. The probability that an element will break followed by the fracture of at least one adjacent element is

$$p_2 = F(\sigma) (p_{2/1} + p_{3/1}). \quad (12)$$

Therefore, for the composite as a whole the expected number of groups of two or more broken fibers is

$$E_2 = \frac{M(N-1)p_2}{2}, \quad (13)$$

and the associated probability of having at least one such group is

$$P_2 = 1 - (1 - \frac{1}{2} p_2)^{M(N-2)} \quad (14)$$

where the factors of  $1/2$  are introduced to account for the independence of order of two fractures.

The probability that an element will fracture followed by the breaking of at least two other fibers in a row is equal to the probability of at least two fractures less the probability that two will break without further fractures occurring. This probability is

$$p_3 = p_2 - F(\sigma) p_{2/1} (1 - p_{3/2} - p_{4/2}) \quad (15)$$

The probability of having at least one group with three or more fractures is

$$p_3 = 1 - (1 - \frac{1}{4} p_3)^{M(N-2)} \quad (16)$$

and the expected number of such events is

$$E_3 = \frac{1}{4} p_3 M(N-2) \quad (17)$$

The analogous expressions for groups of four or more fractures is

$$p_4 = p_3 - F(\sigma) \left[ p_{3/1} (1 - p_{54/3A}) + p_{2/1} p_{3/2} (1 - p_{54/3B}) \right] \quad (18)$$

$$P_4 = 1 - (1 - \frac{1}{8} p_4)^{M(N-3)} \quad (19)$$

$$E_4 = \frac{1}{8} p_3 M(N-3) \quad (20)$$

Although it has not been possible to obtain the general expression for the probability of a group containing an arbitrary number of broken elements it is contended that this expression is only of academic interest. It is argued that once the probability of secondary breaks (i. e. the probability of groups containing two or more fractures) becomes significant failure of the composite can be expected. More will be said of this point later on.

#### Comparison with Experiments

The ultimate test of any theory is its agreement with experimental results. The present theory has been compared with the data obtained in References 17 and 4 for glass-epoxy composites.

The tests reported in Reference 4 were run on composites consisting of a single layer of 3 1/2 mil E-glass fibers embedded in two resin systems (B and C). Tests were run to determine the strengths of the fibers for several gage lengths. As in Reference 4, it is assumed that the cumulative distribution function can be characterized sufficiently well by the Weibull distribution.

$$F(\sigma) = 1 - e^{-\alpha L \sigma^\beta} \quad (21)$$

where  $L$  is the length of the fibers and  $\alpha$  and  $\beta$  are parameters that characterize the distribution. Using this expression the variation of mean fiber strength with gage length is

$$\bar{\sigma}_L = (\alpha L)^{-\frac{1}{\beta}} \Gamma(1+1/\beta). \quad (22)$$

The fiber parameters are found to be

$$\beta = 9.40, \quad \alpha \frac{1}{\beta} = 181.5 \text{ ksi.}$$

From the photographs of the specimens under polarized light the ineffective lengths for series B and C were found to be 0.031" and 0.086", respectively.

Using this data the expected number of single broken elements were calculated from Equation 4, and are represented by the dashed lines in Figures 9 and 10. The number of fractures observed experimentally in the various specimens in the two test series are presented for comparison. It can be seen that for low stress levels there are generally more fractures than the theory predicts. However, the behavior is most important at the higher stress levels in the area of failure loads, and here agreement is fairly good considering the statistical spread in fiber properties and the experimental uncertainties involved. The relatively large number of fractures at low stress levels is possibly a result of damage to the fibers during fabrication of the specimens since glass is notoriously sensitive to handling as far as strength is concerned. However, since the observed fractures approach the expected number of higher stress levels they are of little importance. If, on the other hand, failure occurs without a significant accumulation of fractures the breaks at low stress level may be of extreme importance. More will be said of this later on.

The quantities of  $E_1$ ,  $E_2$ ,  $E_3$  and  $E_4$  (where  $E_i$  represents the expected number of groups of fractures having at least  $i$  broken fibers) obtained in

Equations 4, 13, 17 and 20 are plotted for test series B and C in Figures 11 and 12. It can be seen that the expected number of multiple fracture groups ( $E_2$ ,  $E_3$  and  $E_4$ ) rise sharply in the observed range of composite failure. The failure predictions of Reference 3 are presented for comparison.

In order to assess the validity of the expressions for multiple fractures the number of groups of multiple fractures were counted on films of the tests. The results are plotted in Figures 13 and 14. The dashed curves in the figures are calculated values of  $E_2$ . It can be seen that, in general, multiple breaks begin to appear in the stress range predicted by the theory. Furthermore, the composites fail without the occurrence of a large number of multiple-break groups compared to the number of isolated single fractures.

There are several factors that could account for this phenomenon. One possibility is illustrated by Figure 15. This graph shows the relative behavior of the sum  $p_{2/1} + p_{3/1}$  for static and dynamic overstress factors. It will be recalled that this sum represents the probability of the fracturing of at least one element adjacent to a single broken fiber. In the observed failure range <sup>assuming a Weibull distribution for  $t(c)$  the expected value (mode) for the first fiber fracture is found to be</sup> the dynamic curve is markedly higher than the static curve indicating that there is a definite possibility of a failure crack being caused by the dynamic effects of fiber fracture rather than by cumulative static probability of failure. It should also be noted that the use of overstress-factors is just an approximation and that the actual stress concentrations caused by multiple breaks may be, and probably are, much more severe than those of single fractures. (As an analogy, the stress concentration factor for an ellipse

increases with the aspect ratio) Whatever the mechanism, experimental observations seem to indicate that multiple breaks tend to occur shortly before composite failure.

The present theory was also compared with two tests on continuous glass fibers in epoxy run by Friedman<sup>(17)</sup>. The Weibull parameters for the strength distribution of fibers used are

$$\beta = 4.0, \quad \alpha - \frac{1}{\beta} = 137.1.$$

Since  $\beta$  is an inverse measure of dispersion, these fibers had a much wider spread in failure stress levels than did those of Reference 4. This large dispersion is reflected in the wide spread of the curves of  $E_1$ ,  $E_2$ ,  $E_3$  and  $E_4$  presented in Figure 16. However, failure in both specimens occurred quite near the stress level for which the first multiple fracture is predicted.

On the basis of the experimental evidence cited it is proposed that the failure stress of a continuous fibrous composite loaded in tension parallel to the fibers can be reasonably well predicted by that load for which the first multiple fracture is expected to occur. That is,

$$E_2 = \frac{M(N-1)}{2} F(\sigma) (p_{2/1} + p_{3/1}) = 1. \quad (23)$$

#### Analysis of Non-Cumulative Fracture Mode

Although a large number of isolated, fractures are observed in glass-epoxy composites, this is not the case for other fiber-resin systems such as boron-epoxy and boron aluminum. For these composites failure usually

occurs catastrophically, without an accumulation of isolated fractures. However, Leno<sup>(19)</sup> has demonstrated scattered fractures in a boron-aluminum composite containing 5% volume fraction of fibers, which is quite small.

The absence of a significant number of isolated fractures seems to indicate that the entire composite is failing at the load at which the weakest fiber breaks. This would mean that the matrix is actually detrimental since the strength of a bundle of fibers, without a matrix, would be stronger. It was, therefore, decided to determine the theoretical value at which a first fiber fracture is expected and compare the results with experimental evidence.

Consider a population of fibers of length  $L$  whose strength is characterized by the probability density  $g(\sigma)$ . For a sample of  $N$  fibers from this group the distribution function for the strength of the weakest fiber has the following form

$$p_0(\sigma) = Ng(\sigma) [1-G(\sigma)]^{N-1} \quad (24)$$

Assuming a Weibull distribution for  $G(\sigma)$  the expected value (mode) for the first fiber fracture is found to be

$$\sigma_e = \left( \frac{\beta - 1}{NL\alpha\beta} \right)^{\frac{1}{\beta}} \quad (25)$$

Friedman<sup>(17)</sup> ran two tests on boron-epoxy specimens 2 inches long which contained about 90 fibers. The Weibull parameters for the fibers were found to be



$$\beta = 7.0, \quad \alpha - \frac{1}{\beta} = 368.$$

The fiber stress levels, at failure for the test specimens were 193 and 215 ksi. The expected value for the first fracture computed from Equation 26 is 171.5 ksi which is about 16% lower than the average failure stress of the two specimens. On the other hand, the first multiple fracture is predicted ( $E_2 = 1$ ) to occur at 300 ksi while the theory of Reference 3 predicts a failure stress of 428 ksi. In the last two cases Friedman's definition of ineffective length was used.

Grinius<sup>(20)</sup> also ran tests on boron fibers in an epoxy matrix. These specimens were 2.5 inches long and contained 25 fibers. The Weibull parameters for the fibers were found to be

$$\beta = 11.11, \quad \alpha - \frac{1}{\beta} = 433.$$

Unfortunately only one undamaged specimen was tested. This specimen failed at 304 ksi fiber stress. The expected value of stress for the first fracture is 296 ksi while the first multiple fracture is predicted at 330 ksi and the failure stress predicted by the theory of Reference 3 is 340 ksi. It should be noted that to obtain the last two values, the definition of the ineffective length presented in Reference 3 was used.

From the experimental observation of the absence of cumulative fractures and the good correlation between the observed failure stress levels and those predicted for the first fiber break a good case can be made for the hypothesis that composites exhibiting this type of failure are only as strong

in tension as their weakest fiber. If this is also the case for the three dimensional composites, the matrix must be designed so that it will prevent this type of failure from occurring. This can possibly be accomplished by using a ductile matrix or by allowing the matrix to partially debond from a broken fiber.

### Conclusions

A statistical model including the effects of stress concentrations for planar arrays of fibers in a matrix has been presented which provides a good description of composite behavior up to the failure load. The stress level for which the first multiple fracture is expected to occur has been proposed as a predicted failure stress.

The model predicts that the composite itself is a "brittle" material in that its strength decreases as the length or width of the specimen increases. This is illustrated in Figure 17 where the variation of  $E_2$  with length is presented for the composite system used in test series B of Reference 4. This is in contrast with the theory in that paper which predicts a composite strength that is independent of length for large values of  $M$ .

Finally, it has been shown that the failure stress level in tests of three composites that did not exhibit cumulative damage occurred at about the expected value of stress at which the first fracture was predicted. This failure stress is lower than that for a bundle of fibers of the same length and number indicating that the matrix may have a detrimental effect in composites exhibiting this type of failure.

The present study demonstrates that the understanding of composite behavior is a continually evolving process and that even in the case of such a simple

loading condition as pure tension the failure mechanisms are not completely understood. More work must be done, for example, to explain the apparent difference in failure modes observed in glass and boron fibers, and to extend the analysis of stress concentration effects to three-dimensional composites.

## The Steady-State Viscoelastic Response

A systematic study of viscoelastic behavior of fiber-reinforced composites was initiated by Hashin (Ref. 21). Such analyses are motivated by both theoretical and practical points of view. Fibrous composites consisting of linear viscoelastic phases are a natural extension of the linear elastic model in which phase materials are assumed to be Hookean Solids. On the other hand, phase materials in composites do exhibit very strong time dependent properties especially in a high temperature environment. A basic understanding of the viscoelastic behavior of composites is important before such materials are utilized in practical applications.

Hashin (Ref. 21) related the effective viscoelastic properties of a composite which is composed of linear viscoelastic phases to those of its constituents by a correspondence principle. This same model used by Hashin is used to study the steady state response to some simple types of sinusoidal surface tractions or surface displacements. It should be noted that in Hashin's approach to viscoelastic theory of composites, inertia forces are neglected so that only quasi-static motion is treated. The present study is based on Hashin's work (Ref. 21) and the same assumption is implicit so that wave propagation phenomena will not be considered here.

Following Reference 21, the general macroscopic viscoelastic behavior of a composite can be described by the following constitutive equations:

$$\bar{\sigma}_{ij}(t) = \int_0^t G_{ijkl}^*(t-\tau) \frac{d\bar{\epsilon}_{kl}(\tau)}{d\tau} d\tau \quad (1)$$

or

$$\bar{\epsilon}_{ij}(t) = \int_0^t J_{ijk\ell}^*(t-\tau) \frac{d\bar{\sigma}_{k\ell}(\tau)}{d\tau} d\tau \quad (2)$$

where  $\bar{\sigma}_{ij}(t)$  and  $\bar{\epsilon}_{ij}(t)$  are, respectively, the average stress and average strain in the composite at time  $t$ ;  $G_{ijk\ell}^*(t)$  and  $J_{ijk\ell}^*(t)$  are the effective relaxation moduli and effective creep compliances, respectively.

By the symmetry of the average stress and average strain tensors, the following symmetry relations hold:

$$G_{jik\ell}^*(t) = G_{ijk\ell}^*(t) = G_{ij\ell k}^*(t) \quad \text{for } t \geq 0 \quad (3)$$

$$J_{jik\ell}^*(t) = J_{ijk\ell}^*(t) = J_{ij\ell k}^*(t)$$

In order to establish the correspondence principle between viscoelasticity and elasticity, it is assumed in Reference 21

$$G_{ijk\ell}^*(t) = G_{k\ell ij}^*(t) \quad \text{and} \quad \text{for } t \geq 0 \quad (4)$$

$$J_{ijk\ell}^*(t) = J_{k\ell ij}^*(t)$$

which are the Onsager Reciprocal Relations (Ref. 22)

The one-sided Laplace transform of (1) and (2) gives

$$\hat{\bar{\sigma}}_{ij}(p) = p \hat{G}_{ijk\ell}^*(p) \hat{\bar{\epsilon}}_{k\ell}(p) \quad (5)$$

$$\hat{\epsilon}_{ij}^*(p) = p \hat{J}_{ijkl}^*(p) \hat{\sigma}_{kl}^*(p) \quad (6)$$

where  $p$  is the transform variable and the circumflex " $\wedge$ " above a function denotes its Laplace Transform which is assumed to exist. Because of the formal resemblance of (5) and (6) to the generalized Hooke's Law in elasticity,  $p \hat{G}_{ijkl}^*(p)$  and  $p \hat{J}_{ijkl}^*(p)$  are termed transform domain (TD) effective moduli and compliances, respectively.

Now for unidirectional fiber-reinforced composites, transverse isotropy will be considered (Ref. 21, 11). Consequently, only five effective relaxation moduli (or five effective creep compliances) are independent so that (5) and (6) can be much simplified. For example, (5) can be written down in terms of the following five independent TD effective relaxation moduli:

- $p \hat{K}_{23}^*(p)$  -- the plane strain TD effective bulk modulus;
- $p \hat{G}_{23}^*(p)$  -- the TD effective transverse shear modulus;
- $p \hat{G}_1^*(p)$  -- the TD effective in-plane shear modulus;
- $p \hat{E}_1^*(p)$  -- the TD effective Young's modulus;
- $p \hat{C}_{11}^*(p)$  -- to be associated with uniaxial stress in fiber direction with transverse deformation prevented by a rigid enclosure.

On the other hand, the TD effective creep compliances are the reciprocals of the corresponding TD effective relaxation moduli. For example

$$p \hat{k}_{23}^* (p) = \frac{1}{p \hat{K}_{23}^* (p)}$$

$$p \hat{g}_{23}^* (p) = \frac{1}{p \hat{G}_{23}^* (p)}$$

etc..

After the effective characteristic functions (relaxation moduli and creep compliances) are defined, Hashin(Ref.21) used a correspondence principle to relate the effective viscoelastic characteristic functions to the effective elastic moduli of a duplicate composite body with elastic phases.

On the other hand, the effective elastic moduli of unidirectional fiber-reinforced composites have been obtained by Hashin and Rosen(Ref. 11). Closed-form expressions for four effective elastic moduli and bounds for the fifth are obtained for the "random array" geometry. In applying the corresponding principle, Hashin (Ref. 21) used these expressions and went through a replacement scheme to obtain the Laplace Transforms of the corresponding effective viscoelastic characteristic functions. Therefore, the entire problem of finding the quasi-static viscoelastic response reduces to Laplace Transform inversion which is not always easy. However, for cases where inversion is formidable, Abel-Tauber theorems can be used to draw important conclusions on the behavior of the effective moduli and compliances without the operation of inversion. Refs. 21 and 11 are referred for details.

Now, for a unidirectional fiber-reinforced composite body under special

boundary displacement or traction conditions (Ref. 21), (1) and (2) can be reduced to

$$\bar{\sigma}(t) = \int_{0_-}^t G^*(t-\tau) \frac{d\bar{\epsilon}(\tau)}{d\tau} d\tau \quad (7)$$

$$\bar{\epsilon}(t) = \int_{0_-}^t J^*(t-\tau) \frac{d\bar{\sigma}(\tau)}{d\tau} d\tau \quad (8)$$

where  $\bar{\sigma}(t) \left( \bar{\epsilon}(t) \right)$  is a component of the stress (strain) tensor  $\bar{\sigma}_{ij}(t) \left( \bar{\epsilon}_{ij}(t) \right)$  whereas  $G^*(t) \left( J^*(t) \right)$  represents one of the five effective relaxation moduli (effective creep compliances) of physical importance as defined previously. Henceforth, (7) (or (8)) will be used as the representative average stress-strain relation that defines a particular viscoelastic characteristic function.

In the course of obtaining the steady-state response by making use specifically of the results of Ref. 21, we shall first develop certain relationships and investigate their validity. Then the general results will be applied specifically to the unidirectional fiber-reinforced composite to obtain explicit expressions which characterize the response. Since we are interested in steady-state response to sinusoidal input, we can assume that the input has been applied on the body for an indefinitely long time and that all initial disturbances have died out. Under this circumstance, it is convenient to put the beginning of motion at time  $-\infty$  (Ref. 23). Hence (7) and (8) are modified to the following forms:

$$\bar{\sigma}(t) = \int_{-\infty}^t G^*(t-\tau) \frac{d\bar{\epsilon}(\tau)}{d\tau} d\tau \quad (9)$$



and

$$\bar{\epsilon}(t) = \int_{-\infty}^t J^*(t-\tau) \frac{d\bar{\sigma}(\tau)}{d\tau} d\tau \quad (10)$$

By changing the integration variable from  $\tau$  to  $\xi$  where  $t - \tau = \xi$ , (9) and (10) become, respectively,

$$\bar{\sigma}(t) = \int_0^{\infty} G(\xi) \bar{\epsilon}'(t-\xi) d\xi \quad (11)$$

$$\bar{\epsilon}(t) = \int_0^{\infty} J^*(\xi) \bar{\sigma}'(t-\xi) d\xi \quad (12)$$

where prime denotes differentiation with respect to the argument of the function.

Using complex representation for sinusoidal oscillation, we put

$$\bar{\epsilon}(t) = \epsilon_0 e^{i\omega t} \quad (13)$$

where  $\epsilon_0$  is in general a complex number and  $\omega$ , a real number, is the angular frequency of the oscillation.

Substituting (13) into (11) we obtain

$$\bar{\sigma}(t) = i\omega \epsilon_0 e^{i\omega t} \tilde{G}^*(\omega) \quad (14)$$

where

$$\tilde{G}^*(\omega) = \int_0^{\infty} G^*(\xi) e^{-i\omega\xi} d\xi \quad (15)$$

is the one-sided Fourier Transform of  $G^*(t)$  if it exists.

Let  $\bar{\sigma}(t) = \sigma_o e^{i\omega t}$ , where  $\sigma_o$  is in general a complex number, then by (14),

$$\frac{\bar{\sigma}(t)}{\bar{\epsilon}(t)} = \frac{\sigma_o}{\epsilon_o} = i \omega \widetilde{G^*}(\omega) M^* \quad (16)$$

where  $M^*$  is called the effective complex modulus associated with  $G^*(t)$ .

Equation (16) can also be written as

$$\bar{\sigma}(t) = |M^*| \epsilon_o e^{i(\omega t + \delta)} \quad (17)$$

where  $\delta = \tan^{-1}$

$$\frac{\text{Im}[M^*]}{\text{Re}[M^*]}$$

which reveals the fact that  $\bar{\sigma}(t)$  is not in phase with  $\bar{\epsilon}(t)$ .

Similarly, if  $\bar{\sigma}(t) = \sigma_o e^{i\omega t}$  then (12) becomes

$$\bar{\epsilon}(t) = i \omega \sigma_o e^{i\omega t} \widetilde{J^*}(\omega) \quad (18)$$

where

$$\widetilde{J^*}(\omega) = \int_0^\infty J^*(\xi) e^{-i\omega \xi} d\xi \quad (19)$$

is the one-sided Fourier Transform of  $J^*(t)$  if it exists.

Let  $\bar{\epsilon}(t) = \epsilon_o e^{i\omega t}$  then by (18),

$$\frac{\bar{\epsilon}(t)}{\bar{\sigma}(t)} = \frac{\epsilon_o}{\sigma_o} = i \omega \widetilde{J^*}(\omega) \equiv \frac{1}{M^*} \quad (20)$$

or

$$\tilde{\epsilon}(t) = \frac{1}{|M^*|} \sigma_o e^{i(\omega t - \delta)} \quad (21)$$

which again shows that  $\tilde{\epsilon}(t)$  lags behind  $\tilde{\sigma}(t)$  with a phase lag  $\delta$ .

From both (16) and (20), it follows that

$$-\omega^2 \tilde{G}^*(\omega) \tilde{J}^*(\omega) = 1$$

if both  $\tilde{G}^*(\omega)$  and  $\tilde{J}^*(\omega)$  exist.

The physical significance of  $\text{Im}[M^*]$  and  $\text{Re}[M^*]$  is now discussed.

First of all, it can be shown that the rate of work done by surface traction at time  $t$  on a body can be expressed in terms of an integral over the entire body as follows:

$$\int_S T_i \dot{u}_i dS = \int_V \sigma_{ij} \dot{\epsilon}_{ij} dV$$

where  $S$  denotes the boundary surface and  $V$ , the volume of the body. The above equality is valid only under the assumption of quasi-static motion.

Furthermore, under special boundary conditions on the boundary surface  $S$  (displacement boundary condition  $u_i(S) = \epsilon_{ij}(t) x_j$  or traction boundary condition  $T_i(S) = \sigma_{ij}(t) n_j$ , (Ref. 21)), it is easy to show that:

$$\int_V \sigma_{ij}(\underline{x}, t) \dot{\epsilon}_{ij}(\underline{x}, t) dV = \tilde{\sigma}_{ij}(t) \dot{\tilde{\epsilon}}_{ij}(t) V$$

Therefore, the total work done from time  $t_1$  to time  $t_2$  is:

$$\int_{t_1}^{t_2} \left[ \int_S T_i \dot{u}_i dS \right] dt = V \int_{t_1}^{t_2} \tilde{\sigma}_{ij}(t) \dot{\tilde{\epsilon}}_{ij}(t) dt$$

If  $t_2 - t_1$  is the period of motion, then

$$W = V \int_{t_1}^{t_2} \bar{\sigma}_{ij}(t) \dot{\epsilon}_{ij}(t) dt \quad (22)$$

denotes the total work done on the system in a cycle. According to the First Law of Thermodynamics, for isothermal steady state deformation,  $W$  is the total energy dissipated and transferred to the surroundings in the form of heat in a cycle. Under the special boundary conditions by which (7) and (8) are obtained,  $W$  in (22) can be reduced to the following simple form:

$$W = VF \int_{t_1}^{t_2} \bar{\sigma}(t) \dot{\epsilon}(t) dt \quad (23)$$

where the factor  $F$  is either 1 or 2 depending on the boundary condition.

Therefore, if  $\bar{\epsilon}(t) = \text{Re} [\epsilon_0 e^{i\omega t}]$  and  $\bar{\sigma}(t) = \text{Re} [M^* \epsilon_0 e^{i\omega t}]$ , then for a cycle with angular frequency of motion  $\omega$ , after some manipulation, (23)

becomes

$$W = VF \int_{\tau}^{\tau + \frac{2\pi}{\omega}} \bar{\sigma} \dot{\epsilon} dt = \pi \epsilon_0^2 \text{Im} [M^*] VF \quad (\epsilon_0 \text{ is assumed}$$

to be real without loss of generality) where  $\tau$  is any time during the motion.

This gives the amount of energy dissipated in a cycle.

Furthermore, it can be shown that a fraction of the amount of energy  $\frac{\epsilon_0^2}{2} \left( \text{Re} [M^*] \right) VF$  is twice in every cycle alternately stored and expended in

the system. Therefore,  $\text{Im} [M^*]$  is related to the energy dissipated while  $\text{Re} [M^*]$  is related to the energy stored.

From the above results, it is clear that in the steady state, the responding average stress (or average strain) will vary sinusoidally with the same angular frequency  $\omega$  as that of the input average strain (or average stress) with a phase difference  $\delta$  which is a function of  $\omega$ . Moreover, the amplitude ratio  $\frac{\sigma_0}{\epsilon_0}$  is also a function of  $\omega$  only.

According to (16) and (20), the knowledge of  $M^*$  hinges on the knowledge of  $\hat{G}^*(\omega)$  or  $\hat{J}^*(\omega)$ . However,  $\hat{G}^*(\omega)$  and  $\hat{J}^*(\omega)$  are formally related to the Laplace Transforms  $\hat{G}^*(p)$  and  $\hat{J}^*(p)$  by the following relations:

$$\hat{G}^*(\omega) = \hat{G}^*(i\omega) \quad (24)$$

and

$$\hat{J}^*(\omega) = \hat{J}^*(i\omega) \quad (25)$$

Therefore, if expressions for  $\hat{G}^*(p)$  and  $\hat{J}^*(p)$  are known,  $\hat{G}^*(\omega)$  and  $\hat{J}^*(\omega)$  can be obtained immediately by the replacement of variable  $p$  in  $\hat{G}^*(p)$  and  $\hat{J}^*(p)$  by  $i\omega$ . However, there still exists the problem of convergence -- given a function of time  $t$ , the existence of its Laplace Transform does not imply the existence of its Fourier Transform. Thus, given a Laplace Transform of a viscoelastic characteristic function, it is necessary to examine the location of its singularities in a complex plane of complex variable  $p$ . According to the definitions of the one-sided Laplace and Fourier Transforms, it is observed that if the singularities of the Laplace Transform are all located in a region to

the left of imaginary axis of the complex plane, then the corresponding Fourier Transform exists.

Hashin (Ref.21) has obtained closed-form expressions for some effective relaxation moduli and creep compliances for the 'random array' model. Then, by making use of (24) and (25), the corresponding effective complex moduli can be obtained in a straight-forward manner. For example, for elastic fibers embedded in a viscoelastic matrix, the effective relaxation moduli  $K_{23}^*(t)$  characterizing the plane strain dilatation has the following form in the Laplace Transform domain:

$$p K_{23}^*(p) = [k_m(p) + \frac{1}{3} \Gamma_m(p)] + v_f \left\{ \frac{1}{K_f + \frac{1}{3} G_f - k_m(p) - \frac{1}{3} \Gamma_m(p)} + \frac{v_m}{k_m(p) + \frac{4}{3} \Gamma_m(p)} \right\}^{-1}$$

where  $k_m(p)$ ,  $\Gamma_m(p)$  are matrix TD moduli;  $K_f$  and  $G_f$  are fiber elastic bulk and shear moduli;  $v_f$  and  $v_m$  are the fiber and matrix volume fractions, respectively. All these quantities are considered known if the composite body is given. Then according to (24), formally we have:

$$i\omega \hat{K}_{23}^*(\omega) = [k_m(i\omega) + \frac{1}{3} \Gamma_m(i\omega)] + v_f \left\{ \frac{1}{K_f + \frac{1}{3} G_f - k_m(i\omega) - \frac{1}{3} \Gamma_m(i\omega)} + \frac{v_m}{k_m(i\omega) + \frac{4}{3} \Gamma_m(i\omega)} \right\}^{-1}$$

and the complex moduli associated with  $K_{23}^*(t)$  is, according to (16),

$$M_{23}^* = i\omega \hat{K}_{23}^*(\omega)$$

Furthermore, it follows from Ref.21 that for rigid fibers,

$$\hat{K}_{23}^*(\omega) = \tilde{K}_m(\omega) + \frac{\tilde{G}_m(\omega)}{3} + \left[ \tilde{K}_m(\omega) + \frac{4}{3} \tilde{G}_m(\omega) \right] \frac{v_f}{(1 - v_f)}$$

where  $\widetilde{K}_m(\omega)$  and  $\widetilde{G}_m(\omega)$  are the one-sided Fourier Transforms of the matrix bulk and shear relaxation moduli, respectively. On the other hand, if fibers are rigid and the matrix is elastic in dilatation and Maxwellian in shear, Hashin(Ref.21) has obtained simple expression for the effective creep compliance  $k_{23}^*(t)$  of which the one-sided Fourier Transform does not exist. Similarly, other steady-state responses such as in-plane shear, etc. can be obtained in a straight-forward manner.

It is emphasized here that the method developed here is also valid for other models than the composite-cylinder-assembly model used in Ref. 21; the latter is only a case in which bounds of some of the characteristic functions in transform domain coincide to yield closed-form expressions. If other expressions can be obtained by other models, the corresponding effective complex moduli can be obtained by the replacement scheme defined by (24) and (25). On the other hand, vibration experiments can be performed on composites to determine experimentally their respective effective complex moduli from which information on their corresponding effective viscoelastic characteristic functions can be obtained through Fourier transformations.

## Evaluation of Transverse Effectiveness Factors for Use in Elastic Analysis of Three Dimensional Filamentary Composites

The method of analysis developed in Reference 1 for the elastic constants of composites having filamentary reinforcements at various angles to the three principal orthogonal axes of the material employed factors  $\beta_0, \beta_0', \beta_{00}$  etc. to define the transverse effectiveness of the filaments for resisting stretching, shearing, etc. For simplicity the assumption was made that the transverse effectivenesses were the same for all strains due to stretching ~ regardless of whether the strains were induced by Poisson's ratio effects, or were simply those in the direction of an applied extension. (Different values of transverse effectivenesses in shear from those in stretching were, however, allowed for.) This approximation led to generally satisfactory results for stiffnesses, with the possible exception of  $E_L$ , that is the stiffness along the filaments, for uni-directional reinforcement - a somewhat disturbing exception in view of the simplicity of calculation of this stiffness by the rule of mixtures. Even more disturbing was the fact that the values of Poisson's ratios calculated with this simplifying assumption of equal transverse effectiveness factors were not consistent with those found by other methods of calculation.

Guidelines for the extension of the analysis of Reference 1 to provide for various values of  $\beta$  for direct and Poisson strains were included with the analysis, but within the time available no evaluation could be made to determine whether or not the extension would be justified. A brief series of calculations has now been made to evaluate the differences among the various transverse effectivenesses for the extended analysis. The results are shown in Figure 18,



and the equations relating thereto are reproduced as Tables 1 to 3.

In Figure 1, curves of  $\beta_{0L}$ ,  $\beta_{0T}$ ,  $\beta_{0LT}$ , and  $\beta_{0G}$  are plotted as derived from the upper limit values of the elastic constants of Reference 11 for a typical glass/epoxy combination employing the assumption that

$\beta_{0L} = \beta_{0T} = \beta_{0LT} = \beta_{0G} = 1$ . As can be seen, differences among  $\beta_{0T}$ ,  $\beta_{0LT}$ , and  $\beta_{0G}$  are found, of increasing relative magnitude with increasing volume fraction of binder (the abscissa on the Figure). Also  $\beta_{0L}$  differs from the value unity; this is the variation which is to be anticipated from the previously noted inconsistent calculation of  $E_L$  for uni-directional reinforcement with the simplified transverse effectiveness assumption. The differences in the various  $\beta$  - values shown are, of course, just those consistent with the elastic constants as found from Reference 11. The use of the  $\beta$ 's of Tables 2 and 3 thus reproduce properly all the elastic constants of a unidirectional reinforcement configuration, and hence provide a self-consistent basis from which the effects of multi-angular reinforcement may be determined via extensions to equations like those of Reference 1.

These extensions have been made and the general equations for the compliances incorporating the various  $\beta$ 's are presented in Table 4.

As presently written, the equations of Tables 2, 3, and 4 conceal some internal inter-relationships among the various expressions. For example, the trigonometric expressions of Table 4 are for convenience written in terms of the three angles  $\phi$ ,  $\psi$ , and  $\Omega$  which the reinforcing filaments make with the composite orthogonal axes of symmetry (1, 2, and 3). Only two

angles are needed, however, to define the filamentary directions;  $\phi$ ,  $\psi$ , and  $\Omega$  are related by the well known formula

$$\cos^2 \phi + \cos^2 \psi + \cos^2 \Omega = 1 \quad (1)$$

Similarly, for convenience six transverse effectivenesses have been defined ( $\beta_{0L}$ ,  $\beta_{0T}$ ,  $\beta_{LT}$ ,  $\beta_{0G}$ ,  $\beta_0'$ ,  $\beta_0''$  - see tables 1, 2, and 3), where only five  $\beta$ 's are needed for consistency with the five elastic constants used in evaluating the transverse effectivenesses. Accordingly the equations of Table 3 may be combined, as for example to yield the relation

$$\beta_{0G} = \frac{\beta_{0T}(1-\nu_f) - \beta_0''(1-2\nu_f)}{\nu_f} \quad (2)$$

where  $\nu_f$  = the Poisson's ratio of the filamentary material.

Thus simplifications of the equations as given in Table 4 are undoubtedly possible by the employment of the trigonometric expressions, and  $\beta$  values which lead to the least complex algebra.

## DESIGN CONCEPTS

### Study of Composite Structures

Efficient application of composite materials to aerospace structures requires proper selection of reinforcement pattern and material as well as overall structural arrangement. To a large degree guidelines for optimum design of such composite structures have been lacking, nor have they been obvious a priori to the designer.

Some clues about possible directions toward efficient configuration have recently become available. Reference 24 explored effects of material and reinforcement pattern on the structural efficiency of boost vehicle shells. Reference 2 investigated similar effects for a number of aircraft structural elements. While these studies revealed a number of specific factors of importance for efficiency of application of composites, three general conclusions also evolved which served as a basis for the studies to be reported here. These conclusions were:

1. For a wide range of shell type applications the isotropic ( $0^\circ$ ,  $\pm 60^\circ$ ) reinforcement configuration is most efficient.
2. The high (multi-directional) stiffness-to-density ratio of beryllium makes it more efficient than most near-future composites for many shell and plate type structures, - particularly if the load intensities encountered are low, or if stiffness requirements are important.
3. Filamentary composites appear most attractive when used as unidirectionally reinforced elements to carry unidirectional loads.

The further question that seems to arise from these conclusions is whether some combination of the biaxial properties of beryllium (or isotropic composite) with the uniaxial properties of one-directional filamentary reinforcement may possibly be the best configuration of all.

#### Circular Tube-Columns

To explore this possibility on an orderly basis, a simple round-tube column was selected as a first model for study. This model was chosen for simplicity; for an isotropic material optimization of the thin-walled tube in compression has perhaps achieved the status of being a classic example of balancing proportions between local buckling and column bending to achieve minimum weight. Thus its use to explore effects of combinations of unidirectional and multidirectional properties is uncomplicated by complexities of the optimization procedure itself.

Accordingly beginning with the model of Reference 25, modifications were assumed of increasing complexity, and the effects on efficiency evaluated. As a first step, unidirectionally reinforced composite stiffeners were assumed added to the tube at three equally spaced points around the circumference. These stiffeners were assumed to contribute nothing to the local stability, or instability, of the tube walls, but were assumed to add effective areas for column bending so that the effective radius of gyration of the tube is given by the expression

$$\left(r_{Gyr}\right)_{eff}^2 = \frac{\frac{1}{2}(2R^2 - 2Rt + t^2) + \frac{1}{2}R^2 V_B \frac{E_B}{E_0}}{V_0 + V_B \frac{E_B}{E_0}} \quad (1)$$

where

$(r_{Gyr})_{Eff}$	radius of gyration of stiffened tube
R	outside radius of tube
t	thickness of tube
$E_B$	Young's modulus of unidirectional (boron) composite
$E_o$	Young's modulus of tube material
$v_B$	volume fraction of composite stiffeners
$v_o$	volume fraction of tube material ( $v_B + v_o = 1$ )

With equation (1) incorporated into the procedure of Reference 25, the efficiencies of the reinforced tubes were calculated from the formulas that follow

$$\frac{P}{L^2} = 0.00912 \frac{E_{o_{sec}}}{E_{o_{ten}}} \left\{ \frac{(2\frac{R}{t} - 1) \left( 1 + \frac{v_o E_B}{v_o E_{o_{sec}}} \right) \left( 1 + \frac{v_o E_B}{v_o E_{o_{ten}}} \right)}{\left( \frac{R}{t} \right)^2 \left[ \frac{L}{4\pi} \left( 2\frac{R^2}{t^2} - 2\frac{R}{t} + 1 \right) + \frac{1}{2\pi} \left( \frac{R}{t} \right)^2 \left( \frac{v_o E_B}{v_o E_{o_{ten}}} \right) \right]} \right\} \quad (2)$$

$$\frac{W}{L^3} = \frac{\rho_o + \rho_B \frac{v_B}{v_o}}{1 + \frac{v_o E_B}{v_o E_{o_{sec}}}} \left\{ \frac{P/L^2}{0.3 E_{o_{sec}} \left( \frac{1}{R} \right)} \right\}$$

where

$P$	axial load
$L$	column length
$W$	overall weight
$\rho_B$	density of stiffening material
$\rho_c$	density of tube material

and the subscripts Sec and Tan refer to the secant and tangent moduli of the tube material, respectively.

As indicated in the formulas, the reduced moduli used for plastic buckling were the tangent modulus for column bending, and the secant modulus for local buckling. The use of the tangent modulus for column bending is well founded. The use of the secant modulus for local buckling is used here as slightly more optimistic than the root mean square of the tangent and secant moduli as proposed in Reference 26. Thus the efficiency curves resulting are perhaps slightly too high in the plastic region, representing a kind of upper bound. (Most affected are the curves for beryllium which should be accordingly somewhat discounted at the upper end.) In any event the use of this possibly optimistic reduced buckling modulus changes none of the conclusions drawn from the results.

Results of the calculations are given in Figures 19 to 24. In Figure 19 are given basic results for unstiffened aluminum-alloy and beryllium circular-tube columns. Here, the beryllium tubing is found to vary from 25% of the weight of the aluminum-alloy tubing in the elastic range  $\left( P_L < 1.4 \frac{KN}{m^2} [0.2 \text{ psi}] \right)$

to 80% of the aluminum-alloy weight at high stresses ( $P_2 > 276 \frac{\text{KN}}{\text{m}^2}$  [40 psi]).

The addition of the boron/epoxy three-point reinforcement permits the aluminum-alloy tubing to be made substantially lighter both at high and low loadings (Fig. 20). In the elastic stress range there is apparently an optimum reinforcement ratio ( $\frac{v_B}{v_0} \approx 0.667$ ) beyond which higher percentages of reinforcement do not further increase the efficiency. At the high stresses, however, the very great strength and stiffness of the unidirectional reinforced composite provide increases in efficiency up to the maximum reinforcement ratio considered ( $\frac{v_B}{v_0} = 4$ ).

The beryllium round tubing is not improved by the boron composite reinforcement at low stresses; rather the efficiency is decreased as the reinforcement ratio increases. This trend is just barely reversed, as might be expected, at high loadings (see Fig. 21).

Comparisons between Figures 20 and 21 reveal that at low loadings the unreinforced beryllium is always the lightest of the combinations considered, being approximately one-third the weight of the best boron/epoxy-aluminum. At the high stresses on the other hand the reinforced aluminum is better than any beryllium tube, being about one-half the weight of the beryllium construction at the maximum loading considered. Thus it appears that the low proportional limit strain of the beryllium together with the flat top to the beryllium stress-strain curve beyond the proportional limit prevents it from acting effectively in conjunction with high-strength uni-directional reinforcement. In this range a better combination of materials is an isotropic boron/epoxy

configuration for the tube walls. This configuration should still be elastic at the values of  $P/L^2$  covered in Figures 19 - 21, and at the maximum values of  $P/L^2$  considered the isotropic boron/epoxy tube is calculated from equations (1) and (2) to weigh very nearly one-half as much as the best reinforced aluminum tube.



## Scalloped Tube Columns

One of the pitfalls of efficiency studies like the foregoing is the possibility that a poor geometrical shape has been chosen, and as a result misleading conclusions are derived about the effects of various materials of construction. Ideally an optimum shape should be used (if need be the optimum for each material combination) so that shape effects may be divorced from material effects in the evaluations of the calculations.

In order to assess the shape effect, the efficiencies of scalloped tubes were also investigated. First, a three-lobed scalloped round shape was used (Figure 22). The objectives of the scalloped shape are enhanced local buckling resistance due to decreased radius of curvature of the tube wall together with increased column bending resistance because the scalloped tube approximates an equilateral triangle, and the equilateral triangle has a 21% greater cross-sectional moment of inertia for the same area than a circle. Because the scalloped round tube does not substantially enhance the moment of inertia, however, it was abandoned in favor of a scalloped triangular tube. The characteristics of these two shapes are summarized in Figure 22.

In Figure 22 are plotted the percentage increases from a simple thin-walled round tube section attained by scalloped-round and scalloped-triangle sections having the same cross-sectional area and radius of curvature-to-thickness ratios as the reference round tube. As indicated by the curves of the Figure, the "scalloped triangle" has substantially greater potential for enhancing the column strength (at a constant  $R/t$  so that in first approximation the local

buckling strength is constant). than the "scalloped circle." Furthermore, the apexes of the triangular shape provide a greater radius of gyration for added stiffening as in the form of concentrated boron/epoxy elements than the crests of the scallops of the "scalloped circle."

While clearly the extreme limit of 21% increase in section properties represented by the "infinitely scalloped" triangle ( $\frac{\theta}{2} = 0$ ) of Figure 4 surely cannot be attained, the development of a reasonable fraction of that amount may be anticipated for "reasonable" proportions. Here "reasonable" is taken to mean that the cusps between scallops are of sufficient depth to establish stable corners not prone to local buckling at the stresses encountered by the tubes. The assumption was made that the proportions so labelled on Figure 22 are reasonable, and likely performance gains through their use for reinforced composite columns was calculated with the results given in Figures 23 and 24. For these calculations, equation ( 2 ) was replaced by

$$\frac{P}{L^2} = 0.02912 \left( \frac{E_{osc}}{E_{oten}} \right)^2 \left\{ \frac{\left( 1 + \frac{\nu_B E_B}{\nu_B E_{osc}} \right) \left( 1 + \frac{\nu_B E_B}{\nu_B E_{oten}} \right)}{\frac{I_{\Delta}}{A_0^2} + 6 \frac{\nu_B E_B}{\nu_B E_{oten}} \left( \frac{r^2 \sin^2 \frac{\theta}{2}}{\nu_B A_0} \right)} \right\} \left( \frac{r}{R} \right)^2 \quad (3)$$

where

$I_{\Delta}$

moment of inertia of scalloped triangle section

$(\frac{1}{2}R)_{Eq}$

area of triangle section (equal to area of circular

section of equivalent  $R/t$ )

inside radius of scallops

equivalent thickness-radius ratio of tube

In Figures 23 and 24 comparisons of the efficiencies of the reinforced scalloped triangle tubes with envelope curves representing the lightest reinforced round tubes (the dotted curves on Figures 23 and 24, derived from Figures 20 and 21) show the expected gains for the triangular shape. With the triangular shape higher reinforcement ratios for the aluminum alloy tubing are effective (Fig. 23) and a reinforcement ratio  $\frac{V_2}{V_0} = 4$  produces a tube column competitive with beryllium even in the elastic range (see Fig. 21). Further, the boron/epoxy reinforcement of beryllium in the plastic range is more effective with the scalloped-triangle shape. The general trends established in the studies of the reinforced-round tube columns, however, are not changed by the more efficient triangle shape. Thus the scalloped-triangle beryllium tube is the most efficient of all at low loadings and the reinforced aluminum-alloy becomes more efficient when the stresses would cause yielding of the beryllium.

The gains in efficiency shown on Figures 23 and 24 for the scalloped-triangle shape appear great enough so that experiments to determine their validity appear desirable. That is, experimental definition is needed of the stability of a scalloped-wall tube to establish the degree of scalloping beyond which corners of cusps will no longer remain fixed as straight lines along the tube to provide edges as restraints against local buckling distortions.

## Plate Efficiencies

The efficiencies of composite materials for plate applications, already investigated for a variety of material combinations in Reference 25, have exhibited similar characteristics to those already discussed above for tube-columns. Indeed combinations of beryllium and  $0^{\circ}$  boron/epoxy plates made up as sandwiches with the beryllium as the faces and the  $0^{\circ}$  boron/epoxy as the core demonstrate rather clearly the problems encountered in the development of combination metal composite structures, as is shown in Figure 25.

In Figure are plotted the results of calculations (made as in Reference 25) of the efficiencies of sandwich plates which have  $0^{\circ}$  reinforced boron/epoxy cores and faces of beryllium, isotropic boron/epoxy, and (at the very top end of the curve) no faces at all. The solid curve represents the beryllium-faced sandwiches; up to the discontinuity (at  $\frac{N_x}{b} = 14.5 \frac{\text{MN}}{\text{m}^2} [2.1 \text{ ksi}]$ ) the plates are totally elastic (to achieve this elasticity at such high values of  $\frac{N_x}{b}$  a compressive pre-stress is assumed in the boron/epoxy core just sufficient to stress the faces to the proportional limit in tension at zero external load). The rapid increase in weight of sandwich above the discontinuity arises from the continuing decrease in stiffness of the beryllium faces as they are stressed further and further beyond their proportional limit. The dotted curve represents the higher efficiency that would be attained with beryllium with a higher elastic limit (or pre-stress). Inasmuch as neither of these improvements in the beryllium response appear possible of attainment in practice, the solid curve is the realistic one for the sandwich, and, as indicated, it can be surpassed in

efficiency - as by sandwiches utilizing isotropic boron/epoxy faces at the higher load intensities. Indeed as the loads become high enough, only the  $0^\circ$  boron/epoxy retains enough stiffness to be effective, and no faces at all become most efficient.

To a degree, the curves of Figure 25 may be considered to depict in general the various characteristics which must be balanced in composite plate construction for maximum efficiency, as follows:

- (1)  $0^\circ$  reinforced material should be used as the strength element, if possible pre-stressed to provide the maximum possible elastic range to the material used to provide transverse stiffness or plate buckling resistance.
- (2) The material used to provide the plate buckling resistance (the face material in a sandwich) should be selected on the basis of the stresses to be carried, - at low stresses beryllium is most attractive, at higher stresses composite configurations approaching closer and closer to the  $0^\circ$  configuration should be used.
- (3) While the example shown (Figure 25) is for a solid sandwich, so that the average stress is simply  $\frac{N_x}{t} = \frac{N_x}{b} \left( \frac{b}{t} \right)$ , the same rules as (1) and (2) apply for hollowed out constructions which raise the average stress to  $\frac{N_x}{\bar{t}}$  where  $\bar{t}$  is the average thickness and  $\bar{t} \leq t$ . Thus, in general, any hollowing out (light weight core sandwich construction, etc.) which

does not introduce new instabilities or failure modes is like an increase in the structural index value on Figure 25, - i.e., it tends to make optimum constructions utilizing higher percentages of  $0^\circ$  reinforcement and lower percentages of beryllium.

the efficiencies of the  $\pm 45^\circ$  B/Epoxy and beryllium-epoxy Z-panel constructions. These comparisons are presented in Figure 26.

## Panel Efficiencies

The plate efficiencies just discussed were considered on the basis of initial buckling stresses only. Particularly at low stresses, as is well known, plates of most materials can continue to carry compression load without failing at stresses substantially above the initial buckling stress.

For plate assemblies incorporating  $0^\circ$  reinforced composites as stiffeners, initial buckling of the plates may be expected to cause the major part of any subsequent load increase to be borne by these stiffeners. This load transfer into the  $0^\circ$  reinforcement is precisely the mechanism noted desirable above for increased structural efficiency. Accordingly, for example, compression panels incorporating  $0^\circ$  reinforced stiffeners should be expected to achieve high structural efficiencies.

High structural efficiencies were indeed found for  $0^\circ$  boron/epoxy Z-section stiffeners on  $\pm 45^\circ$  reinforced boron/epoxy skin in Reference 2. Part of this high efficiency arose from the high shear stiffness of the skin material (allowing the use of thin skins and hence allowing most of the material to be incorporated in the stiffeners.)

Reviews of the properties of  $\pm 45^\circ$  boron/epoxy and comparisons with the properties of beryllium suggest that replacement of the  $\pm 45^\circ$  boron/epoxy skin on the panels of Reference 2 with beryllium should result in even higher efficiencies than those calculated therein. For example, pertinent properties of these two materials are compared in the following table:

	<u><math>\pm 45^\circ \text{B/Epoxy}</math></u>	<u>Be</u>
Density $\frac{\text{Mg}}{\text{m}^3}$ (pci)	2.19 (0.079)	1.86 (0.067)
Yield Stress $\frac{\text{MN}}{\text{m}^2}$ (ksi)	138 (20)	400 (58)
Shear Modulus $\frac{\text{GN}}{\text{m}^2}$ (ksi)	72.5 (10,500)	145 (21,000)
Young's Modulus $\frac{\text{GN}}{\text{m}^2}$ (ksi)	25.5 (3700)	304 (44,000)
Yield Strain	0.0054	0.0013

Thus, except for its low yield strain, beryllium appears vastly superior to the  $\pm 45^\circ \text{B/Epoxy}$ . The low yield strain, however, raises uncertainties, and a detailed evaluation is required to determine whether the beryllium/composite panels are as superior as would at first appear.

Such an evaluation was made as a part of the study of Reference 27. The results are reproduced here and extended to make possible direct comparisons of the efficiencies of the  $\pm 45^\circ \text{B/Epoxy}$  and beryllium-skin Z-panel constructions. These comparisons are presented in Figure 26.

Figure 26 plots curves of weights of box-beam compression covers (plus supporting ribs) for optimized Z-stiffened panels. Optimization includes the selection of rib spacing and stiffener size and spacing for minimum weight to carry a design bending moment  $M$  with a box beam of width  $b$  and depth  $d$ . Further the skin thickness is required to be adequate, in terms of the box depth,



to provide a specified torsional stiffness; - accordingly the beryllium and  $\pm 45^\circ$  B/Epoxy are compared at "equivalent" values of skin thickness  $t_{Seq}$  such that

$$t_{S_{B/Epoxy}} = t_{S_{Be}} \left( \frac{G_{Be}}{G_{B/Epoxy}} \right) = 2t_{S_{Be}}$$

The curves of Figure 26 show substantial weight savings for the beryllium skin on  $0^\circ$  B/Epoxy stiffeners. These weight savings are depicted by the cross-hatching between the curves for the  $\pm 45^\circ$  B/Epoxy-skin panels (the dashed curves) and the beryllium-skin panels (the solid curves) at the equivalent torsional stiffness measures (equal values of  $d/t_{Seq}$ ).

Several factors accumulate to produce the weight savings shown in Figure 26 for the beryllium-skin composite construction: (1) the favorable shear stiffness of the beryllium permits an even higher percent of stringer material-with its high-strength, high column-bending stiffness characteristics, - than for the  $\pm 45^\circ$  Boron/Epoxy skin; (2) the beryllium is of lower density than the boron/epoxy; (3) the high strength of the  $0^\circ$  reinforcement (as noted in the opening discussion for this section) permits it to carry the load long after initial buckling of the beryllium skin.

## Studies of Composite Materials

### Three-Dimensionally Isotropic Materials

The form of the matrix of elastic constants relating stress to strain in a generalized Hooke's law has been studied for various conditions of structural symmetry. For two dimensions, it is known that a material is isotropic in a plane for which there exists a normal axis of at least six-fold symmetry. Thus, as a practical example, a fibrous composite plate is effectively isotropic in its plane when one  $n^{\text{th}}$  of the fibers are oriented every  $\frac{\pi}{n}$  radians for  $n \geq 3$ . (By effectively isotropic, it is meant that the average stress, average strain relations are isotropic.). Similar conditions to obtain three dimensional isotropy appear to be unavailable in the literature. Several configurations having multiple symmetry conditions which might yield at least an approximation to an elastically isotropic material have been studied. The first material treated has two three-fold axes of symmetry separated by the angle for which the cosine is  $-1/3$ . Such a material can be obtained with a fibrous composite having one fourth of the fibers oriented in each of the four directions defined by the altitudes of a regular tetrahedron.

The stress-strain relations for a general elastic body may be written as:

$$\tau_{ij} = c_{ij} \epsilon_j \quad i, j = 1, 2, \dots, 6 \quad (1)$$

where  $\tau_{ij}$  are the stress components

$\epsilon_j$  are the strain components

$c_{ij}$  are the 21 independent elastic constants ( $c_{ji} = c_{ij}$ )

We treat a material having two axes of three-fold symmetry at an angle  $\theta$  such that

$$\cos \theta = -\frac{1}{3}$$

As a consequence of this, there must exist two additional axes of three-fold symmetry; the four axes being oriented along the directions of the four altitudes of a regular tetrahedron. (This four-legged array is called a caltrop.)

We select the vertices of the tetrahedron at the points:  $(0, 0, \frac{1}{2}\sqrt{\frac{3}{2}})$ ,  $(\frac{1}{\sqrt{3}}, 0, -\frac{1}{4}\sqrt{\frac{2}{3}})$ ,  $(-\frac{1}{2\sqrt{3}}, \frac{1}{2}, -\frac{1}{4}\sqrt{\frac{2}{3}})$ ,  $(-\frac{1}{2\sqrt{3}}, -\frac{1}{2}, -\frac{1}{4}\sqrt{\frac{2}{3}})$ .

This is a tetrahedron with centroid at the origin. This body has elastic symmetry with respect to a rotation of  $\frac{2\pi}{3}$  about the z axis. Thus for the following transformation of coordinates, the stress-strain relations remain unchanged:

	x	y	z
x'	$\cos \theta$	$\sin \theta$	0
y'	$-\sin \theta$	$\cos \theta$	0
z'	0	0	1

This reduces the elastic constant matrix to the following form (Ref. 28)

$$c_{ij} = \begin{bmatrix} c_{11} & c_{12} & c_{13} & c_{14} & c_{15} & 0 \\ c_{12} & c_{11} & c_{13} & -c_{14} & -c_{15} & 0 \\ c_{13} & c_{13} & c_{33} & 0 & 0 & 0 \\ c_{14} & -c_{14} & 0 & c_{44} & 0 & -c_{15} \\ c_{15} & -c_{15} & 0 & 0 & c_{44} & c_{14} \\ 0 & 0 & 0 & -c_{15} & c_{14} & \frac{1}{2}(c_{11} - c_{12}) \end{bmatrix} \quad (2)$$

This array has seven independent constants.

The stress-strain relations will also be invariant for a rotation about one of the other axes of three-fold rotational symmetry. In particular, we consider a  $120^\circ$  (counter-clockwise) rotation about the axis passing through the point  $\left(\frac{-1}{2\sqrt{3}}, \frac{1}{2}, -\frac{1}{4}\sqrt{\frac{2}{3}}\right)$  followed by a  $120^\circ$  (clockwise) rotation about the axis passing through the point  $\left(\frac{1}{\sqrt{3}}, 0, -\frac{1}{4}\sqrt{\frac{2}{3}}\right)$ . The direction cosines for this transformation are

	x	y	z
x'	$\frac{1}{3}$	0	$\frac{2\sqrt{2}}{3}$
y'	0	-1	0
z'	$\frac{2\sqrt{2}}{3}$	0	$-\frac{1}{3}$

It can be shown that the elastic constant matrix must therefore be of the form

$$c_{ij} = \begin{bmatrix} c_{11} & c_{12} & c_{11} + c_{12} - c_{33} & 0 & \sqrt{2}(c_{11} - c_{33}) & 0 \\ & c_{11} & c_{11} + c_{12} - c_{33} & 0 & -\sqrt{2}(c_{11} - c_{33}) & 0 \\ & & c_{33} & 0 & 0 & 0 \\ & & & \frac{3}{2}c_{11} - \frac{c_{12}}{2} - c_{33} & 0 & -\sqrt{2}(c_{11} - c_{33}) \\ & & & & \frac{\sqrt{3}}{2}c_{11} - \frac{c_{12}}{2} - c_{33} & 0 \\ & & & & & \frac{1}{2}(c_{11} - c_{12}) \end{bmatrix} \quad (3)$$

This material has only three independent elastic constants and is a material with the symmetry of the cubic crystal. Indeed, a transformation

of the principal axes of a cubic crystal given by:

	$x''$	$y''$	$z''$
$x'$	$\frac{1}{\sqrt{2}}$	$-\frac{1}{\sqrt{2}}$	0
$y'$	$\frac{1}{\sqrt{6}}$	$\frac{1}{\sqrt{6}}$	$-\sqrt{\frac{2}{3}}$
$z'$	$\frac{1}{\sqrt{3}}$	$\frac{1}{\sqrt{3}}$	$\frac{1}{\sqrt{3}}$

followed by a transformation of axes given by

	$x'$	$y'$	$z'$
$x$	0	-1	0
$y$	1	0	0
$z$	0	0	1

brings the principal axes of a cubic crystal in coincidence with the  $x y z$  axes which are the reference axes for eqs. (5). This transforms the array of elastic moduli of a cubic crystal to the following form:

$$c_{ij} = \begin{bmatrix} \frac{1}{2}(C+D+2E) & \frac{1}{6}(C+5D-2E) & \frac{1}{3}(C+2D-2E) & 0 & \frac{1}{3\sqrt{2}}(C-D-2E) & 0 \\ \frac{1}{2}(C+D+2E) & \frac{1}{3}(C+2D-2E) & 0 & 0 & -\frac{1}{3\sqrt{2}}(C-D-2E) & 0 \\ & \frac{1}{3}(C+2D+4E) & 0 & 0 & 0 & 0 \\ & & \frac{1}{3}(C-D+E) & 0 & -\frac{1}{3\sqrt{2}}(C-D-2E) & 0 \\ & & & \frac{1}{3}(C-D+E) & 0 & 0 \\ & & & & \frac{1}{6}(C-D+4E) & 0 \end{bmatrix} \quad (4)$$

where C, D and E are the three independent elastic moduli for the cubic system.

The array (4) has the same form as the array (3). In fact, if we let

$$C = 4c_{11} - 3c_{33}$$

$$D = -c_{11} + 6c_{12} + 6c_{33}$$

$$\text{and } E = -\frac{(c_{11} + c_{12})}{2} + c_{33}$$

then (3) and (4) are identical. This shows that the material with the elastic moduli of the form of (3) is elastically cubic.

Although this material is not isotropic, the properties for a particular fibrous composite prove interesting, as will be shown in the following section.

Another configuration of interest is that of Reference 1 which is constructed by taking three pairs of reinforcing filaments, oriented with reference to an orthogonal Cartesian coordinate system,  $xyz$ , as follows: one pair in the  $xy$  plane making angles of  $\pm\theta$  with the  $x$  axis; one pair in the  $yz$  plane making angles of  $\pm\theta$  with the  $y$  axis; and one pair in the  $zx$  plane making angles of  $\pm\theta$  with the  $z$  axis. It was shown in Reference 1 that when  $\theta$  is approximately  $30^\circ$ , the shear modulus, Poisson's ratio, and Young's modulus satisfy the relation:

$$G = \frac{E}{2(1+\nu)}$$

It can be shown that when

$$\theta = \tan^{-1}(2 \sin 18^\circ) \approx 31^\circ 43'$$

the twelve rays ( 6 lines) from the origin pass through the vertices of a regular icosahedron with centroid at the origin. These six lines are therefore axes of five-fold symmetry. The possibility that a body having six axes of five-fold symmetry as isotropic is suggested. This result is perhaps of academic interest only, as it does not appear possible to construct a continuous space lattice having five-fold axes of symmetry.

## Evaluation of Moduli of Caltrop Reinforced Materials

The equations derived for the elastic constants of three-dimensionally reinforced composites were used to compute properties of the caltropic reinforcement configuration. Calculations were made using both the equations of Reference 1 (for which  $\beta_{o_T} = \beta_{o_{LT}} = \beta_{o_G}$ , etc.) and the equations of Table 4 herein. The following material constants were employed.

$E_f$	(Young's modulus of filaments)	10
$E_b$	(Young's modulus of binder)	$\frac{1}{21} \times E_f$
$\nu_f$	(Poisson's ratio of filaments)	0.2
$\nu_b$	(Poisson's ratio of binder)	0.35

These values correspond to those for E-Glass in epoxy. Values of  $\beta$  were found for these material constants by derivation of the upper bound Hashin-Rosen (Ref. 2) elastic constants of unidirectional reinforcement at values of volume fraction filament of 0.2, 0.4, 0.6, and 0.8.

Results of the calculations are given in Figure 27 for the filament orientation shown. Both methods of calculation yield different compliances in the 2- and 3-directions (values of  $A_4$  and  $A_6$ ) from that in the 1-direction. Differences between the two methods are not substantial, as was anticipated, nor are the compliances found substantially at variance in the three directions. For engineering purposes, the compliances in the three directions are probably so nearly equal that differences among them can be neglected.



### Three Phase Composite Compression Members

In the foregoing studies of the efficiency of combination metal/composite structures the efficacy of  $0^\circ$  reinforced composite material to provide strength to the structure while some other material or configuration provided adequate transverse stiffness or continuity was evaluated. On the presumption that such  $0^\circ$  reinforcement would truly be an extremely high compressive strength material, these evaluations were indeed favorable. Because of the relative weakness and lack of stiffness of available resin binder systems, however, it is not obvious that the  $0^\circ$  configuration necessarily has the maximum compressive strength. Rather, as this section will demonstrate, some transverse reinforcement may be desirable.

Reference 4 described the mechanics of stabilization of uni-directional filaments in compression. As noted there, three failure modes may be encountered:

(1) a mode in which the shear stiffness of the binder material governs, described by the equation

$$\sigma_c = \frac{G_b}{1-\nu_f}$$

where

- $\sigma_c$  ultimate compressive stress in filament direction
- $G_b$  shear modulus of binder
- $\nu_f$  volume fraction filament

(2) a mode in which the strength of the binder is critical, described by the equation

$$\sigma_c = \sqrt{\frac{v_f E_f \sigma_{by}}{3(1-v_f)}}$$

where

$\sigma_{by}$  yield stress for binder

$E_f$  Young's modulus for filament

and (3) a mode in which the stiffnesses of both filaments and binder are operative, described by the equation

$$\sigma_c = 2v_f \sqrt{\frac{v_f E_f E_b}{3(1-v_f)}}$$

The lowest value of  $\sigma_c$  found from the foregoing equations is, of course, the failure stress.

In all three modes of failure the binder properties are important. Accordingly, increases in binder properties may be expected to be reflected in increases in compressive strength of uni-directionally reinforced composites. One method for increasing effective binder properties would appear to be to take some of the uni-directional, load-carrying filaments and distribute them uniformly throughout the binder. Thus, while for every failure model the value of  $\sigma_c$  would tend to be reduced by the reduced volume fraction of load-carrying filament ( $v_f$  in above equations), the net effect should be expected to be an increase in  $\sigma_c$  due to the improvement in binder stiffnesses and strengths.

In order to assess the potential magnitude of compressive strength

increase available by this approach, the assumption was made that the binder properties attained by the utilization of some fraction  $v_{fb}$  of the filamentary material (the original volume fraction filaments  $v_{fo}$  was assumed to be 0.5 throughout) for binder reinforcement would be given by simple, rule-of-mixture-like, expressions such as

$$E'_b = \frac{1}{4} v_{fb} E_f + (1 - v_{fb}) E_b$$

$$G'_b = \frac{E'_b}{2(1 + \nu')}$$

where

$\nu'$  is the Poisson's ratio found by the rule of mixtures for filaments and binder

and

$$\sigma'_{by} = \frac{1}{4} v_{fb} \sigma_{fy} + (1 - v_{fb}) \sigma_{by}$$

with the primes denoting the properties after binder reinforcement.

Using the foregoing equations, three possible composite combinations were evaluated: (1) boron binder reinforcement for uni-directionally reinforced boron/epoxy; (2) glass binder reinforcement for uni-directionally reinforced glass/epoxy; and (3) glass binder reinforcement for uni-directionally reinforced boron/epoxy. In the first two cases the total amount of reinforcing material in the composite was held constant, so  $v_{fb} + v_f = 0.5$ . In the last case  $v_f$  was held constant and the total amount of reinforcement therefore increased as  $v_{fb}$  was increased.

The results of the calculations for these three combinations are plotted in Figures 28, 29, and 30. In Figure 28, curves for the boron-boron composite are presented for the following nominal constituent properties:

$$E_f = 414 \frac{\text{GN}}{\text{m}^2} \quad (60,000 \text{ ksi})$$

$$E_b = 3.45 \frac{\text{GN}}{\text{m}^2} \quad (500 \text{ ksi})$$

$$\sigma_{fy} = 2.76 \frac{\text{GN}}{\text{m}^2} \quad (400 \text{ ksi})$$

$$\sigma_{by} = 0.1 \frac{\text{GN}}{\text{m}^2} \quad (15 \text{ ksi})$$

$$\psi_f = 0.2$$

$$\psi_b = 0.35$$

In Figure 29 the glass-glass combination is considered for the same binder properties and the following nominal glass properties

$$E_f = 72.45 \frac{\text{GN}}{\text{m}^2} \quad (10,500 \text{ ksi})$$

$$\sigma_{fy} = 2.76 \frac{\text{GN}}{\text{m}^2} \quad (400 \text{ ksi})$$

$$\psi_f = 0.2$$

The boron-glass combination of Figure 30 uses the same nominal properties for each of the materials as those given above.

For properties like those of the boron/epoxy composites of Figure 28, the conversion of a small percentage of the axial filaments into transverse

filaments which effectively stiffen the binder should be advantageous, raising the compressive strength from  $2.75 \frac{\text{GN}}{\text{m}^2}$  (392 ksi) to  $3.8 \frac{\text{GN}}{\text{m}^2}$  (550 ksi), approximately (see Figure 28). If the properties are more like those of the glass/epoxy composites of Figure 29, however, the same gain is not to be expected (see Figure 29). If glass is added to boron/epoxy, on the other hand, as in Figure 30, substantial gains are to be anticipated.

Because of the gains found in the calculations for Figure 28, a series of uni-directional boron/epoxy compression specimens having various percentages of chopped-glass filaments added to the binder were fabricated and tested. The results are shown as the points in Figure 31, with the large and small circles representing nominal glass-filament lengths of 0.16 cm. (1/16 in.) and 0.08 cm. (1/32 in.), respectively. Despite the large scatter, strengthening appeared to be achieved in two cases.

Both the scatter in the test data, and the sensitivity of strength of the boron/epoxy composites of Figure 28 to the small amounts of binder reinforcement point to the critical nature of the role played by the binder in the composites for the development of high compressive stresses. The marked difference between the curves of Figures 28 and 29 suggests that this criticality is substantially greater for boron than for glass reinforcement.

To explore the sensitivity of boron composites to binder properties somewhat further, the calculations represented by the curves of Figure 31 were also made. These curves show the effects of changes in binder strengths ( $\sigma_{by}$ ) and binder-filament-reinforcement strengths on the compressive

strength of the three-constituent composite when the "binder strength" mode is critical. The compressive strength is found to depend most critically on the binder strength at the low ratios of binder reinforcement.

## STUDIES OF MATERIALS-PROPERTIES TESTS

The testing of filamentary composites to determine their mechanical properties has proved to be more difficult than the testing of homogeneous materials like metals. The difficulties take several forms; they may derive from discontinuities encountered in specimens designed to provide a diminished cross-section, as is often done to avoid failures at points of load introduction; they may be associated with the shear weakness of the binder leading to undesired modes of failure; or they may arise because a type of test known to be inadequate is used for economy or other reasons. In this section some of the aspects of mechanical-property testing of composites are examined both analytically and experimentally to help establish guidelines for improved techniques.

### The NOL Ring Split-Dee Tensile Test

The N. O. L. ring "split-dee" tensile test, shown schematically in Figure 32, has the advantages that the specimen may be readily fabricated by winding, and the test may be performed in a conventional universal testing machine without special fixtures (other than the split dees themselves). The test has the disadvantages, however, that (1) no test section is available at which strain gages may be mounted to measure the stress-strain properties, and (2) more seriously, the test introduces substantial bending moments in the ring where the split occurs between the two dees. These bending moments extend above and below the split, as shown in Figure 33. Because the membrane stress in the ring causes it to increase in diameter as the load increases,

the ring tends to pull away from the corners of the dee, and the maximum bending moment is that associated with the load times the deflection to the center of the ring cross-section near the corners of the dees. The magnitude of the bending may be found from the following equations (developed in Appendix B).

$$M_{\frac{\pi}{2}} = \frac{E_1 I \left[ \cosh\left(\frac{l}{\sqrt{E_1 I/P}}\right) - 1 \right]}{\left(R_0 + \frac{r}{2}\right) \cosh\left(\frac{l}{\sqrt{E_1 I/P}}\right)} \quad (1)$$

where  $l$  may be evaluated by the trial and error solution of the equations

$$\theta_1 = \tan^{-1} \left\{ \frac{\sqrt{E_1 I/P} \left(1 - \frac{1.2}{G_{12}} \frac{P}{A}\right) \tanh\left(\frac{l}{\sqrt{E_1 I/P}}\right)}{R_0 + \frac{r}{2}} \right\} \quad (2)$$

and


$$\theta_1' = \sin^{-1} \left\{ \frac{l}{R_0 + \frac{r}{2}} - \frac{\pi}{2} \frac{P}{E_1 A} \right\} \quad (3)$$

such that

$$\theta_1 = \theta_1' \quad (4)$$



where

$M_c$	bending moment at center line of ring, at split in dees
$E_1$	Young's modulus in direction of filaments
$I$	moment of inertia of ring cross-section
$R_o$	initial inside radius of ring
$t$	ring thickness
$P$	load acting in each half of ring (one-half of applied load)
$A$	ring cross-sectional area
	unsupported semi-span between dees
$\theta$ and $\theta'$	slope at point of departure of ring from dee, measured relative to direction of load application.
$G_{12}$	shear modulus along filaments

Evaluation of equation (1) for a typical E-glass reinforced epoxy ring for  $R_o = 7.30$  cm. (2.875 in.) yields the curve of maximum bending stress vs. ring thickness given in Figure 34. Obviously these bending stresses are of sufficient magnitude to raise questions about the engineering merit of the tensile strength values measured as the  $P/A$  stress at the maximum load on the ring.

(Curiously, the magnitude of the bending moment is relatively insensitive to the composite properties. For example, the stress increment due to bending in an hypothetical boron/epoxy ring with  $E_1 = 414 \frac{GN}{m^2}$  (60,000,000 psi) is essentially the same as that in a glass-epoxy ring with  $E_1 = 51.75 \frac{GN}{m^2}$

(7,500,000 psi) at the same load. The increased bending stiffness of the boron/epoxy is compensated for by the decreased diametral expansion of the ring under load, so that the bending stresses remain essentially constant as  $E_1$  varies.)

#### Variations of the Split-Dee Test

The high bending stresses encountered in the split-dee test are rather disappointing in view of the many attractive features of the test. Accordingly the question naturally arises as to whether minor changes may be made in specimen or fixture design which will reduce or eliminate the bending. Some possible variations of this nature are considered below.

The "racetrack" specimen - The provision of a straightaway section adjacent to the split in the dees is a first logical step toward the improvement of the N. O. L. ring split-dee tensile test. Such a specimen is shown schematically in Figure 35.

The analysis of the bending of the critical section of the racetrack is similar to that of the ring, and is described in the following equations:

$$M_x = \frac{E_1 I \left\{ 1 - \frac{1}{\cosh\left(\frac{l - s/2}{\sqrt{E_1 I / P}}\right)} \right\}}{\left(R_o + \frac{r}{2}\right) \left\{ \cosh\left(\frac{s/2}{\sqrt{E_1 I / P}}\right) + \left(\frac{l - s/2}{\sqrt{E_1 I / P}}\right) \sinh\left(\frac{s/2}{\sqrt{E_1 I / P}}\right) \right\}} \quad (5)$$

where now  $l$  is evaluated from

$$\theta_1 = \tan^{-1} \left\{ \frac{\sqrt{E_1 I / P} \left( 1 - \frac{1.2}{G_{12}} \frac{P}{A} \right) \tanh \left( \frac{l - \frac{s}{2}}{\sqrt{E_1 I / P}} \right)}{R_0 + \frac{t}{2}} \right\} - \tan^{-1} \left\{ \frac{\sqrt{E_1 I / P} \left( 1 - \frac{1.2}{G_{12}} \frac{P}{A} \right) \sinh \left( \frac{\frac{s}{2}}{\sqrt{E_1 I / P}} \right)}{R_0 + \frac{t}{2}} \right\} \quad (6)$$

and

$$\theta_1' = \sin^{-1} \left\{ \frac{l - \frac{s}{2}}{R_0 + \frac{t}{2}} - \frac{\pi}{2} \frac{P}{E_1 A} \right\} \quad (7)$$

again with

$$\theta_1 = \theta_1'$$

where  $s$  = length of straightaway, and the other symbols are as before.

Results from the analysis of this racetrack specimen compared to those from the N. O. L. ring are compared in Figure 36. Figure 36 shows that while bending is not eliminated by the straightaway, it is substantially reduced, - even by a relatively short straight section. For example, just a 1 cm (0.4 in.) straightaway reduces the bending moment to less than one-half that of the circular ring.

The mechanics of the reduction of maximum bending moment are suggested in the (exaggerated) sketch of Figure 37. Under load the mid-point of the straightaway deflects inward toward the center of the track, so that even though the curved portions pull away from the dees the eccentricity of the tensile load at mid-span is small and hence the moment associated with it is small, - i. e. the maximum moment is still that near the corners of the dees, not that at mid-span. The fact that the moment in the straight portion is small, however, is advantageous for the use of strain gages in that region.

Experimental confirmation of a qualitative nature of the foregoing analyses of split-dee tests were obtained by photoelastic tests (Figure 33 and 38), and by strain measurements on an enlarged, aluminum-alloy ring (Figure 39). Even with the enlarged ring the stress gradients were so steep around the circumference that the gages could not be located accurately enough to make a quantitative check of the analyses. Indeed, the strain gaging problems pointed up the merits of some such approach as the following for further improving the split-dee test.

### Compression Tests of N.O.L. Rings

A simple compression test for an N.O.L. ring-type specimen (analogous to the split-dee test for tension) would be useful for the evaluation of the compressive properties of filament-wound composites. Efforts to develop such a test under this contract were not successful. The specimen tried is shown schematically in Figure 40, consisting of two short segments cut from an N.O.L. ring and mounted back to back as shown.

Application of tangential end loads to the segments of ring in Figure 40 and pressure-like forces from the supporting, hour-glass-like core ideally would reproduce the compression induced in an entire ring by external pressure.

That is, moment equilibrium at any station  $\theta_1$  along the segment is represented by the equation

$$PR[1 - \cos(\alpha - \theta_1)] = \int_{\theta_1}^{\alpha} w [R^2 \sin(\theta - \theta_1)] d\theta$$

where

$P$  = 1/2 total load

$R$  = ring radius

$\alpha$  = 1/2 angle included by segment

$w$  = intensity of normal load on ring at station  $\theta_1$

that is  $w = w(\theta)$

As might be expected, this equation is compatible with a simple pressure load. Thus, if  $w = P/R$

$$PR \int_0^\alpha [\sin \theta - \theta] d\theta = PR [1 - \cos \alpha \cos \theta - \sin \alpha \sin \theta] \\ = PR [1 - \cos(\alpha - \theta)]$$

Tests of specimens fabricated as sketched in Figure 40, however, were not successful in maintaining the compatibility so readily expressible in equation form. Attempts were made to replace the resin filler of Figure 40 with aluminum - leading to a nice test of the aluminum (Fig. 41); attempts were made to test specimens of larger radius of curvature in this fashion, and a maximum failure stress of  $59 \frac{\text{MN}}{\text{m}^2}$  (86 ksi) was so achieved in a glass/epoxy composite. Despite the fact that failure in this case appeared to be by shearing at the quarter point of the specimen with no evidence of overall column instability (Fig. 42), the stress is less than can be achieved with well collimated, straight compression specimens and is probably not representative of the material strength.

Some evidence of "brooming" of the ends of the specimens was apparent even in this best test. A number of further tests of like specimens with ends cast in cerrobend were made to try to avoid such end failures. Stresses in no case were higher than the foregoing value.

Initially straight specimens appear to be required for compression testing.

### Low-Melting Alloy Casting Fixture of Compression Tests

The use of a fixture in which the specimen ends can be cast in a low-melting point alloy has proved successful in preventing premature "brooming" type failure in tests of straight compression bars. Such a fixture is shown in Figure 42. The fixture incorporates end plates having holes, - of the same shape as the specimen cross-section, - but approximately 0.6 cm. (1/4 in.) oversize so that .3 cm. of the low-melting alloy can be cast all around between the hole wall and the specimen.

Conventional 3 to 1 aspect ratio, uni-directionally reinforced compression specimens have been tested in this type of fixture with consistently high stresses at failure. Consistency and modes of failure both suggest that these high stresses are representative of the compressive properties of the material.

## Elastic Moduli

The desire to measure the elastic constants of a uniaxial fibrous composite by using specimens which represent the filament winding fabrication process has led to the use of thin-walled circumferentially wound tubes (e. g. Ref 29). Axial load and internal or external pressure tests of such tubes can be used to measure four of the five independent effective elastic constants of the composite material. (See Ref. 11 for a discussion of independent effective moduli of composites.) The use of these thin cylindrical tubes to measure the elastic moduli of a composite laminate appears to be a most suitable approach. However, it is not without problems; the first of which is that of definition of the moduli. When a laminate is to be used as a plate or shell structure, the desired elastic relations may be written with respect to the principal geometric axes, denoted as the 1 and 2 directions, as:

$$\begin{pmatrix} N_{11} \\ N_{22} \\ N_{12} \\ M_{11} \\ M_{22} \\ M_{12} \end{pmatrix} = \begin{bmatrix} & & & & & \\ & & & & & \\ & & & & & \\ & & & & & \\ & & & & & \\ & & & & & \end{bmatrix} \begin{pmatrix} \bar{\epsilon}_{11} \\ \bar{\epsilon}_{22} \\ \bar{\epsilon}_{12} \\ \bar{\kappa}_{11} \\ \bar{\kappa}_{22} \\ \bar{\kappa}_{12} \end{pmatrix} \quad (8)$$

(9)

(10)

(11)

(12)

(13)

where:  $\bar{\epsilon}$  are the three middle surface strain components

$\bar{\kappa}$  are the three curvature components



N are the three stress resultants

M are the three moment resultants.

In this form, for an arbitrary laminate, the  $C_{ij}$  matrix is a 6 x 6 array of elastic constants which must be determined experimentally. Because the laminate is non-homogeneous there may be coupling between extension and bending. The existence of certain non-zero terms in the C matrix complicates the relationships among these elastic constants and the so called engineering constants: Young's moduli and Poisson's ratios. This is best illustrated by considering alternate forms of Equations (8) - (13). These Equations may be written as (e.g. Ref. 2):

$$\begin{aligned} N_i &= a_{ij} \bar{\epsilon}_j + b_{ij} \bar{\kappa}_j \\ M_i &= b_{ij} \bar{\epsilon}_j + d_{ij} \bar{\kappa}_j \end{aligned} \quad (14)$$

These Equations are represented by:

$$\begin{Bmatrix} N \\ M \end{Bmatrix} = \begin{bmatrix} a & b \\ b & d \end{bmatrix} \begin{Bmatrix} \bar{\epsilon} \\ \bar{\kappa} \end{Bmatrix} \quad (15)$$

Equation (15) can be manipulated to yield:

$$\begin{Bmatrix} \bar{\epsilon} \\ \bar{\kappa} \end{Bmatrix} = \begin{bmatrix} e & f \\ g & h \end{bmatrix} \begin{Bmatrix} N \\ M \end{Bmatrix} \quad (16)$$

and

$$\begin{Bmatrix} \bar{\epsilon} \\ \kappa \end{Bmatrix} = \begin{bmatrix} A & B \\ C & D \end{bmatrix} \begin{Bmatrix} N \\ M \end{Bmatrix} \quad (17)$$

As an example we now consider the Young's modulus in the 1 direction which can be defined as the ratio of average stress to strain and is therefore given by:

$$E_1 = \frac{N_1}{t \bar{\epsilon}_1} \quad (18)$$

where  $t$  is the laminate thickness.

This modulus can be evaluated from Equation (17) for  $N_2 = N_3 = M_i = 0$ , as

$$E_1 = \frac{1}{t A_{11}} \quad (19)$$

Or it can be evaluated from Equation (16) for  $N_2 = N_3 = \kappa_i = 0$  as:

$$E_1 = \frac{1}{t e_{11}} \quad (20)$$

The definition of Equation (19) is consistent with the usual practice of having all but one of the stress components vanish. However, the restrictions associated with the definition of Equation (20) are representative of the loading conditions on the shell specimen. That is,  $\kappa_i = 0$ , because of symmetry. These two definitions are not the same unless  $b_{ij} = 0$ ; in which event, it follows that

$$f_{ij} = g_{ij} = B_{ij} = C_{ij} = 0 \text{ and } A_{ij} = e_{kj}.$$

It is suggested that the rational approach to this problem is to de-emphasize the calculation of Young's moduli, etc. and to utilize a six by six matrix definition of the elastic constants of a laminate. When a particular extensional or bending stiffness is required, the definition thereof should be explicitly stated.

A second aspect of the modulus problem is the influence of the form of the material anisotropy and the specimen configuration upon measured values. The filament wound cylindrical tube under consideration is a material possessing cylindrical anisotropy. In the case of a circumferential or other winding pattern symmetric with respect to the principal geometric axes, the material may be considered to be cylindrically orthotropic. An analysis of the stress distribution in such a medium for various applied loads is available in Reference 30, which shows that the stress distribution even for simple applied loads is non uniform. For example the axial stress,  $\sigma_z$ , in a cylindrical tube subjected to an axial load is not constant unless  $\nu_{rz} = \nu_{\theta z}$ . This condition is generally not satisfied in a filament wound shell, and for a circumferentially wound shell, the two Poisson ratios are definitely unequal. In this case, the modulus defined by Equation 18 is an average value and can be related to the true value by using the expression for the axial stress,  $\sigma_z$ . This result is presented on page 254 of Reference 30. However, there is evidently a typographical error in Equation (40.4) which is not dimensionally correct as presented. The desired result was therefore rederived for the particular type

of material symmetry represented by the circumferentially wound tube. The extensional stresses and strains for a cylindrically orthotropic tube are given by:

$$\begin{pmatrix} \epsilon_r \\ \epsilon_\theta \\ \epsilon_z \end{pmatrix} = \begin{bmatrix} \frac{1}{E_r} & -\frac{\nu_{r\theta}}{E_\theta} & -\frac{\nu_{rz}}{E_z} \\ -\frac{\nu_{\theta r}}{E_r} & \frac{1}{E_\theta} & -\frac{\nu_{\theta z}}{E_z} \\ -\frac{\nu_{zr}}{E_r} & -\frac{\nu_{z\theta}}{E_\theta} & \frac{1}{E_z} \end{bmatrix} \begin{pmatrix} \sigma_r \\ \sigma_\theta \\ \sigma_z \end{pmatrix} \quad (21)$$

The shear strains and stresses are simply related by:

$$\begin{aligned} \gamma_{\theta z} &= \tau_{\theta z} / G_{\theta z} \\ \gamma_{zr} &= \tau_{zr} / G_{zr} \\ \gamma_{r\theta} &= \tau_{r\theta} / G_{r\theta} \end{aligned} \quad (22)$$

These relations can be further specialized for the circumferentially wound tube inasmuch as the material plane normal to the local fiber direction can be assumed to be a plane of elastic isotropy. Thus

$$\begin{aligned} E_z &= E_r \\ \nu_{r\theta} &= \nu_{z\theta} \\ G_{\theta z} &= G_{r\theta} \end{aligned} \quad (23)$$

Equations (21) and (22) are also applicable to filament wound tubes which are symmetric with respect to the longitudinal and circumferential directions and which have a sufficient number of laminae such that coupling between extension and shear is negligible. To take advantage of this wider applicability the analysis will not utilize the simplifications offered by Equation (23). Since the applied loads are symmetric, there will be no shear stresses or strains and the constitutive relations for this problem are those of Equation (21). By symmetry, all variables will be functions only of the radial coordinate. Thus the equilibrium equations simplify to:

$$\frac{\partial \sigma_r}{\partial r} + \frac{\sigma_r - \sigma_\theta}{r} = 0 \quad (24)$$

which can be satisfied by selecting a stress function,  $\varphi$ , such that

$$\begin{aligned} \sigma_r &= \frac{1}{r} \frac{d\varphi}{dr} \\ \sigma_\theta &= \frac{d^2\varphi}{dr^2} \end{aligned} \quad (25)$$

The only compatibility equation which is not satisfied automatically is:

$$-r \frac{d\epsilon_r}{dr} + \frac{d}{dr} \left( r^2 \frac{d\epsilon_\theta}{dr} \right) = 0 \quad (26)$$

Substitution of Equations (21) and (25) into (26) yields a fourth order differential equation on  $\varphi$  given by:

$$r^4 \varphi^{IV} + 2r^3 \varphi^{III} - r^2 \varphi^{II} + r \varphi^I = 0 \quad (27)$$

$$\text{where } \beta^2 = \frac{S_r}{S_\theta} = \frac{\left( \frac{1-\nu}{r} \frac{\nu}{z} \frac{z}{r} \right)}{\left( \frac{1-\nu}{\theta} \frac{\nu}{z} \frac{z}{\theta} \right)} \quad (28)$$

For  $\beta \neq 1$  the solution is:

$$\varphi = A r^{1-\beta} + B r^{1+\beta} + C r^2 + D \quad (29)$$

The stresses resulting from this are:

$$\left. \begin{aligned} \sigma_r &= A(1-\beta)r^{-(\beta+1)} + B(1+\beta)r^{\beta-1} + 2C \\ \sigma_\theta &= A\beta(\beta-1)r^{-(\beta+1)} + B\beta(\beta+1)r^{\beta-1} + 2C \end{aligned} \right\} \quad (30)$$

The cylinder is considered to be subjected to an axial shortening resulting in a uniform strain,  $\epsilon_z = e$ , and internal and external pressures,  $p_i$  and  $p_o$ , respectively. This strain displacement relations simplify to

$$\left. \begin{aligned} \epsilon_r &= \frac{du}{dr} \\ \epsilon_\theta &= \frac{u}{r} \end{aligned} \right\} \quad (31)$$

Substitution of Equation (30) into Equation (21) defines the strains  $\epsilon_r$  and  $\epsilon_\theta$ . Equation (31) offer two methods of finding  $u$ . For a unique determination:

$$2C = e \left( \frac{\nu}{S_\theta} - \frac{\nu}{S_r} \right) \equiv p_z \quad (32)$$

Thus the third stress is determined initially with:

Use of the boundary conditions:

$$\begin{aligned}\sigma_r(r=r_i) &= -p_i \\ \sigma_r(r=r_o) &= -p_o\end{aligned}\quad (33)$$

defines the remaining two constants in Equation (30). This yields:

$$\begin{aligned}\sigma_r &= p_i \left(\frac{r}{r_i}\right)^{-(\beta+1)} \left[ \frac{1 - \left(\frac{r}{r_o}\right)^{2\beta}}{1 - C^{2\beta}} \right] - p_o \left(\frac{r}{r_o}\right)^{\beta-1} \left[ \frac{1 - \left(\frac{r}{r_i}\right)^{-2\beta}}{1 - C^{2\beta}} \right] \\ p_z &\left\{ 1 - \left(\frac{r}{r_o}\right)^{\beta-1} \left[ \frac{1 - C^{\beta+1}}{1 - C^{2\beta}} \right] - \left(\frac{r}{r_i}\right)^{-(\beta+1)} \left[ \frac{1 - C^{\beta-1}}{1 - C^{2\beta}} \right] \right\}\end{aligned}\quad (34)$$

$$\text{where } C = \frac{r_i}{r_o}$$

$$\sigma_\theta = p_i \beta \left(\frac{r}{r_i}\right)^{-(\beta+1)} \left[ \frac{1 + \frac{r}{r_o}}{1 - C^{2\beta}} \right] - p_o \beta \left(\frac{r}{r_o}\right)^{\beta-1} \left[ \frac{1 + \left(\frac{r}{r_i}\right)^{-2\beta}}{1 - C^{2\beta}} \right]\quad (35)$$

$$p_z \left\{ 1 + \beta \left(\frac{r}{r_i}\right)^{\beta-1} \left[ \frac{1 + C^{\beta+1}}{1 - C^{2\beta}} \right] + \beta \left(\frac{r}{r_i}\right)^{-(\beta+1)} \left[ \frac{1 - C^{\beta-1}}{1 - C^{2\beta}} \right] \right\}$$

$$\sigma_z = E_z e + \nu_{\theta z} \sigma_\theta + \nu_{rz} \sigma_r\quad (36)$$

## Axial Compression Test

It is now possible to compare the results obtained by the tube tests with the actual elastic moduli. First, consider the tube in axial compression. The measured modulus is given by:

$$\bar{E}_z = \frac{\bar{\sigma}_z}{e} \quad (37)$$

$\sigma_z$  is the average axial stress (total load divided by tube cross-sectional area)

Thus:

$$\bar{\sigma}_z = \frac{1}{A} \int \sigma_z dA$$

$$\bar{\sigma}_z = \frac{1}{\pi(r_o^2 - r_i^2)} \int \sigma_z r dr \quad (38)$$

Substituting Equations (36), (34) and (35) with  $p_i = p_o = 0$ , into Equation (38), and the result into Equation (37) yields, after much manipulation:

$$\frac{\bar{E}_z - E_z}{E_z} = \frac{(\nu_{\theta z} - \nu_{rz})^2}{(1 - \nu_{rz} \nu_{zr})} \frac{\beta^2 (\beta^2 + 1)}{(\beta^2 - 1)^2} \left\{ 1 - \frac{2\beta}{1 + \beta^2} \left[ \frac{(1 + C^{2\beta})(1 + C^2) - 4C^{\beta+1}}{(1 - C^{2\beta})(1 - C^2)} \right] \right\} \quad (39)$$

For a thin shell we find by taking the limit of Equation (39) as  $C \rightarrow 1$  that

$$\bar{E}_z = E_z$$

Thus the thin-walled circumferentially wound tube appears to be a suitable test technique for measuring the transverse Young's modulus. The magnitude of the



error associated with this technique is indicated by computing the quantity  $\Psi$  in the following equation as a function of  $\beta$ :

$$\frac{\frac{\bar{E}_z - E_z}{E_z}}{\frac{E_z}{E_z}} = \frac{(\nu_{\theta z} - \nu_{rz})^2}{1 - \nu_{rz} \nu_{zr}} \Psi \quad (40)$$

where the correction factor,  $\Psi$ , is determined by comparison of Equations (39) and (40).

The factor  $\Psi$  was evaluated for a radius ratio of  $C = 0.9$  which is a relatively thick shell for this purpose. Correction factors,  $\Psi$ , for smaller radius ratios,  $C$ , will be smaller. It was found that:

$$\begin{aligned} \Psi &< 0.01 & 2 < \beta \leq 6 \\ \Psi &< 0.1 & 2 < \beta \leq 10 \end{aligned}$$

It seems safe to conclude that the circumferentially wound tube in axial compression is a valid test for the Young's modulus transverse to the fibers of a uniaxial composite.

## Internal Pressure Test

An internal pressure test has been used (e. g. Ref. 29) to determine the Young's modulus in the fiber direction and the Poisson's ratio. Strains are measured on the inner and outer surface. For this loading we may examine the equations for strain by substituting Equations (34) - (36) into Equation (21). For zero longitudinal strain and zero external pressure this yields:

$$\epsilon_{\theta} = P_i \left( \frac{r}{r_i} \right)^{-(\beta+1)} \left( \frac{1}{1-c^{2\beta}} \right) \left\{ \beta \int_{\theta} \left[ 1 + \left( \frac{r}{r_o} \right)^{2\beta} \right] - \frac{\nu_{\theta r}}{2G_{rz}} \left[ 1 - \left( \frac{r}{r_o} \right)^{2\beta} \right] \right\} \quad (41)$$

The measured surface strains will then be given by:

$$\epsilon_{\theta}(r_i) = \frac{P_i}{1-c^{2\beta}} \left\{ \beta \int_{\theta} \left[ 1 + c^{2\beta} \right] - \frac{\nu_{\theta r}}{G_{rz}} (1-c^{2\beta}) \right\} \quad (42)$$

$$\epsilon_{\theta}(r_o) = 2\beta \int_{\theta} P_i \frac{c^{\beta+1}}{1-c^{2\beta}} \quad (43)$$

As in the preceding section, we choose to examine the error associated with the use of equations developed for isotropic materials. The alternative is to write the simultaneous equations relating all the measured strains to all the elastic moduli and solving for the latter. However, this alternative procedure is complex and perhaps not possible as there is no apparent direct measurement to define the transverse shear stiffness,  $G_{rz}$ . Thus, we consider

$$\bar{E}_{\theta} = \frac{\bar{\sigma}_{\theta}}{\epsilon_{\theta}} \quad (44)$$

where  $\bar{E}_\theta$  is the effective circumferential thickness for zero axial strain.  
 $\bar{\sigma}_\theta$  is average circumferential stress.

For equilibrium:

$$\bar{J}_\theta = P_i \left( \frac{c}{1-c} \right) \quad (45)$$

The stiffness defined by Equation (44) can be evaluated by the use of e. g. (45) and either Equation (42) or (43). We denote the results  $\bar{E}_\theta^i$  and  $\bar{E}_\theta^o$  respectively. Treating the thin shell we write:

$$c = 1 - \delta \quad (46)$$

where  $\delta$  is the shell thickness to radius ratio. The results are:

$$\bar{E}_\theta^o = \frac{1}{S_\theta} \left[ 1 + \frac{\delta}{2} \right] \quad (47)$$

$$\bar{E}_\theta^i = \frac{1}{S_\theta} \left[ 1 - \left( \frac{1}{2} + \frac{2\nu_{\theta z} \beta}{G_{rz} S_\theta} \right) \right] \quad (48)$$

Equation (47) shows that the use of the external surface strain measurement yields a result for the extensional stiffness which has an error measured by half the thickness to radius ratio, e. g. 5% error for a radius to thickness ratio of 10. On the other hand, the inner surface measurement involves many other material moduli and is therefore unsuitable for simple use in the circumferential modulus determination.

Note also that there is a significant difference between internal and ex-

ternal strains. Thus:

$$\frac{\epsilon_{\theta}(r_1) - \epsilon_{\theta}(r_0)}{\epsilon_{\theta}(r_0)} = \left( 1 + \frac{\nu_{\theta r}}{G_{rz} S_{\theta}} \right) \left[ \frac{\delta}{1 - (\beta + 1)\delta} \right] \quad (49)$$

*Torsion*

Tension Test

Reference to Section 43 of Reference 30 shows that the stress distribution in a cylindrically anisotropic hollow shell for which there exists at each point a plane of elastic symmetry normal to the axis is obtained in the same way as in an isotropic rod. That is,  $\sigma_{\theta z}$  is the only non-vanishing stress component and

$$\sigma_{\theta z} = \frac{M}{I_o} r$$

The circumferentially wound circular shell satisfies these symmetry requirements and therefore provides an exact measure of the in-plane shear stiffness,

$G_{\theta z}$ .

## CONCLUDING REMARKS

The application of existing analyses of strength and stiffness of fibrous composites to the analysis and design of composite structures has been treated. It has been shown that, although the present understanding of failure mechanisms is incomplete, it is possible to construct a rational set of failure criteria for fibrous composite laminates. Additional studies of the failure mechanisms of a uniaxial composite have been performed by using limit analysis techniques. Also the effect of stress concentrations upon tensile strength has been explored and initial studies were made of the complex moduli of fibrous composites having viscoelastic matrices.

The design criteria were used in the evaluation of columns, plates and panels in which uniaxial composites for high strength were combined with isotropic metals or composites for high stiffness. Designs offering substantial improvement over those made of one material only were demonstrated. Improved composite materials were achieved through the use of a third phase as a local reinforcement of the matrix. Also approximately isotropic three-dimensional materials were designed.

Test methods were analyzed leading to a verification of the suitability of thin-walled tubes for modulus measurements and the unsuitability of the NOL ring for tensile strength measurements. Improvements in methods for measurement of tensile and compressive strength were demonstrated.

The studies emphasize the feasibility of using present methods for the

mechanical analysis of composites in preliminary design studies. They also indicate that our understanding of composite failure mechanisms is a continually evolving one requiring additional theoretical and experimental study.

## REFERENCES

1. Dow, N. F., Rosen, B. W., and Hashin, Z., "Studies of Mechanics of Filamentary Composites," NASA CR-492, June 1966.
2. Dow, N. F., Rosen, B. W. and Kingsbury, H. B., "Evaluation of the Potential of Advanced Composite Materials for Aircraft Structures," AFML-TR-66-144, May 1966.
3. Rosen, B. W., "Tensile Failure of Fibrous Composites," AIAA Journal, Vol. 2, No. 11, (1964).
4. Rosen, B. W., "Mechanics of Composite Strengthening," in "Fiber Composite Materials," American Society for Metals, Metals Park, Ohio, (1965).
5. Shu, L. S. and Rosen, B. W., "Applications of the Methods of Limit Analysis to the Evaluation of the Strength of Fiber Reinforced Composites," to be published.
6. Shu, L. S., "The Evaluation of the Strength of Fiber-Reinforced Composites," presented at "The International Conference on the Mechanics of Composite Materials" held at Philadelphia, Pennsylvania, May 1967.
7. Tsai, S. W., "A Review of Strength Theories of Composite Materials," presented at the Major Status Report - Advanced Composites, " Washington, D. C., September 1966.
8. Azzi, V. D. and Tsai, S. W., "Anisotropic Strength of Composites," Experimental Mechanics, Vol. 5, 283-288 (1965).
9. Tsai, S. W. and Azzi, V. D., "Strength of Laminated Composite Materials," AIAA Journal, Vol. 4, No. 2, 296-301 (1966).
10. Hill, R., "A Theory of the Yielding and Plastic Flow of Anisotropic Metals," Proceedings of the Royal Society of London, A., 281-297, (1948).
11. Hashin, Z. and Rosen, B. W., "The Elastic Moduli of Fiber Reinforced Materials," Journal of Applied Mechanics, Vol. 31E, 223-232 (1964).
12. See for example, Prager, W. and Hodge, Jr., P. G., "Theory of Perfectly Plastic Solids," John Wiley and Sons, Inc. (1965).
13. Drucker, D. C., Greenberg, H. J. and Prager, W., "The Safety Factor of an Elastic-Plastic Body in Plane Strain," Journal of Applied Mechanics, 18, 371-378, 1951b.

14. Koiter, W. T., "General Theorems for Elastic Plastic Solids," Chapter IV in "Progress in Solid Mechanics," Sneddon and Hill, eds., North Holland (1960).
15. Schuerch, H., "Prediction of Compressive Strength in Uniaxial Boron Fiber-Metal Matrix Composite Materials," AIAA Journal, Vol. 4, No. 1, 102-106, 1966.
16. Parratt, N. J., "Defects in Glass Fibers and Their Effect on the Strength of Plastic Mouldings," Rubber and Plastics Age, March 1960, pp. 263-266.
17. Flom, D. G., Mazzio, V. F. and Friedman, E., "High Strength High Modulus, Whisker Reinforced Plastic Composites," AFML-TR-66-362, February 1967.
18. Hedgepeth, J. M., "Stress Concentrations in Filamentary Structures," NASA TN D-882, May 1961.
19. Lenoe, E. M., "Micromechanics of Boron Filament Reinforced Aluminum Composites," Paper No. 9, Seventieth Annual Meeting of the ASTM, Boston, June 1967.
20. Grinius, Victor G., "Micromechanics - Failure Mechanism Studies," AFML-TR-66-177, August 1966.
21. Hashin, Z., "Viscoelastic Fiber Reinforced Materials," AIAA Journal, 4(8), 1411-1417 (1966).
22. DeGroot, S. R., "Thermodynamics of Irreversible Processes," North Holland Publishing Co. (1951).
23. Fung, Y. C., "Foundations of Solid Mechanics," Prentice Hall, New Jersey (1965).
24. Rosen, B. W. and Dow, N. F., "Influence of Constituent Properties Upon the Structural Efficiency of Fibrous Composite Shells," Journal of Spacecraft and Rockets, September 1966.
25. Shanley, F. R., "Weight-Strength Analysis of Aircraft Structures," Dover Publications, New York.
26. Anon., "Buckling of Thin-Walled Circular Cylinders," NASA SP-8007, Dover Publications, New York.



27. Carter, L. L., Dow, N. F., and Rosen, B. W., "Development of a Computer Program for the Evaluation of the Efficiency of Composite, Z-Stiffened Compression Panels, and Some Supporting Experimental Studies," AFML-TR (to be published).
28. Love, A. E. H., "A Treatise on the Mathematical Theory of Elasticity," Dover Publications, New York, (1944).
29. Card, M. F., "Experiments to Determine the Strength of Filament-Wound Cylinders Loaded in Axial Compression," NASA TN D-3522, (1966).
30. Lekhnitskii, S. G., "Theory of Elasticity of an Anisotropic Elastic Body," Holden-Day, Inc., San Francisco, (1963).

## APPENDIX A - Limit Analysis For Composites With Elastic-Brittle Fibers

Five types of surface loadings are considered:

1. Traction equivalent to a uniform shear stress  $\tau_{12}$  are applied on the entire boundary surface.

Use will be made of the theorems of limit analysis which will not be stated here. For lower bound construction, a uniform stress field

$$\tau_{ij} = \begin{bmatrix} 0 & \tau_0 & 0 \\ \tau_0 & 0 & 0 \\ 0 & 0 & 0 \end{bmatrix}$$

is chosen as a statically admissible stress field where  $\tau_0$  is such that Von Mises' yield criterion of the matrix is not violated. Then it can easily be shown that

$$\left( \tau_{12}^L \right)_L = k_b \quad (1)$$

where  $k_b$  is the yield stress of the matrix in simple shear.

For upper bound construction, a kinematically admissible velocity field is chosen as follows:

(a) In the region of the composite specimen not occupied by composite cylinders and on the boundary of the composite cylinders.

$$u_1 = 0, \quad u_2 = \gamma_0 x_1, \quad u_3 = 0 \quad (2)$$

where  $\gamma_0$  is any real number.

(b) In any composite cylinder, the velocity field  $u$  is the elastic displacement solution to the displacement boundary value problem with displacement boundary conditions (Eq. 2) prescribed as formulated in Appendix 2 of (Ref. 11) with the modification that the fibrous core is rigid.

An application of the upper bound theorem gives an upper bound  $(\tau_{12}^L)_U$  as a function of  $\beta$  and  $v_1$  the latter being the volume fraction of all the composite cylinders embedded in the composite specimen:

$$(\tau_{12}^L)_U = k_b + k_b v_1 (I_1 - 1) \quad (3)$$

where

$$I_1 = \frac{1}{\pi(1-\beta^2)} \int_{\beta}^1 \int_0^{2\pi} R \sqrt{1 + \frac{\beta^4}{R^4} + 2 \frac{\beta^2}{R^2} \cos \theta} d\theta dR$$

In the case of "random array" (Ref. 11) for which  $v_1 = 0$  and the fiber volume fraction of the composite specimen  $v_f = \beta^2$ , Equation (3) becomes

$$\frac{(\tau_{12}^L)_U}{k_b} = I_1 \quad (4)$$

2. Tractions equivalent to a uniform shear stress  $\tau_{23}$  are applied on the surface of the specimen.

The condition of plane strain is assumed. Then, the Von Mises' yield criterion for the matrix reduces to a simple form

$$(\tau_{22} - \tau_{33})^2 + 4\tau_{23}^2 \leq 4k_b^2 \quad (5)$$

For lower bound construction, a uniform stress field

$$\tau_{ij} = \begin{bmatrix} 0 & 0 & 0 \\ 0 & 0 & \tau_0 \\ 0 & \tau_0 & 0 \end{bmatrix}$$

is chosen as a statically admissible stress field where  $\tau_0$  is such that Eq. (5) is nowhere violated. Then it follows that the lower bound for the limit load

$$\left( \tau_{23}^L \right)_L = k_b$$

which is independent of fiber volume fraction.

For upper bound construction, the same principle is used here. A kinematically admissible velocity field is chosen as follows:

(a) In the region of the composite specimen not occupied by composite cylinders and on the boundary of the composite cylinders,

$$u_1 = 0, \quad u_2 = \frac{y_0}{2} x_3, \quad u_3 = \frac{y_0}{2} x_2 \quad (6)$$

(b) In any composite cylinder, the velocity field  $\vec{u}$  is the elastic displacement solution to the displacement boundary value problem with displacement boundary conditions (Eq. (6)) prescribed as formulated in Appendix 1 of Ref. 11 with an additional condition that the fibrous core is rigid and the

binder shell is incompressible.

An application of the upper bound theorem gives an upper bound  $(\tau_{23}^L)_U$  as a function of  $\beta$  and  $v_1$ :

$$(\tau_{23}^L)_U = k_b + k_b v_1 (I_2 - 1) \quad (7)$$

where

$$I_2 = \frac{2}{\pi(1-\beta^2)^3} \int_{\beta}^1 \int_0^{2\pi} R \sqrt{\psi_1(\beta, R) + \psi_2(\beta, R) \cos \theta} d\theta dR$$

and

$$\begin{aligned} \psi_1(\beta, R) &= \frac{\beta^4}{R^4} \left[ (\beta^4 + \beta^2 + 1) - \frac{3}{2} (\beta^2 + 1) \frac{\beta^2}{R^2} \right]^2 + \left[ -\frac{(4\beta^4 + \beta^2 + 1)}{2} + 3\beta^2 R^2 \right]^2 \\ \psi_2(\beta, R) &= \frac{2\beta^2}{R^2} \left[ (\beta^4 + \beta^2 + 1) - \frac{3}{2} (\beta^2 + 1) \frac{\beta^2}{R^2} \right] \left[ -\frac{(4\beta^4 + \beta^2 + 1)}{2} + 3\beta^2 R^2 \right] \end{aligned}$$

3. Tractions equivalent to uniform axial tension  $\tau_{22}$  on the composite specimen under the conditions of plane strain.

Using the same principle, the lower bound for the limit load is

$$(\tau_{22}^L)_L = 2k_b$$

For upper bound construction, a kinematically admissible velocity field is chosen which is obtained from the one constructed for the preceding case through an orthogonal transformation such that

$$u_i = d_{ij} u'_j \quad \text{with } d_{ij} = \begin{bmatrix} 0 & 0 & 0 \\ 0 & \frac{1}{\sqrt{2}} & \frac{1}{\sqrt{2}} \\ 0 & -\frac{1}{\sqrt{2}} & \frac{1}{\sqrt{2}} \end{bmatrix}$$

where  $u'_j$  are the velocity components used in the preceeding case referred to an  $x'$ -system. Then, after some manipulation, it turns out that

$$\left( \tau_{22}^L \right)_U = 2 \left( \tau_{23}^L \right)_U$$

Another kinematically admissible velocity field was constructed:

a. In the region of the composite specimen not occupied by composite cylinders and on the boundary of the composite cylinders,

$$u_1 = 0, \quad u_2 = \frac{\gamma_0}{2} x_2, \quad u_3 = -\frac{\gamma_0}{2} x_3$$

or in polar coordinates,

$$u_1 = 0, \quad u_r = \frac{\gamma_0}{2} r_b \cos 2\theta, \quad u_\theta = -\frac{\gamma_0}{2} r_b \sin 2\theta$$

b. In any composite cylinder, the velocity field in polar coordinates is assumed to have the following form:

$$\begin{aligned} u_r &= \frac{\gamma_0}{2} \rho(r) \cos 2\theta \\ u_\theta &= -\frac{\gamma_0}{2} \Omega(r) \sin 2\theta \end{aligned} \quad \text{for } r_f \leq r \leq r_b$$

where  $\rho(r)$  and  $\Omega(r)$  are arbitrary functions and

$$\rho(r_b) = \Omega(r_b) = r_b \quad (8)$$

In addition, we assume that  $\rho(r_f) = \Omega(r_f) = 0$ . Because of the assumed incompressibility of velocity field,  $\rho(r)$  and  $\Omega(r)$  satisfy the following equation:

$$\frac{d\rho(r)}{dr} - \frac{2\Omega(r)}{r} + \frac{\rho(r)}{r} = 0. \quad (9)$$

Furthermore, let  $\rho(r) = A_1(r-r_f)^2 + A_2(r-r_f)^3$  where the constants

$$A_1 = \frac{r_f + 2r_b}{(r_b - r_f)^2}$$

and

$$A_2 = -\frac{r_f + r_b}{(r_b - r_f)^3}$$

have been determined from (8) and (9).

Now the velocity field of the entire specimen is constructed and the upper bound theorem is applied to obtain a new  $\left(\tau_{22}^L\right)_U$  in terms of fiber-volume fraction for the case of "random array". Incidentally, this same velocity field, after an orthogonal transformation, can also be used to obtain a new  $\left(\tau_{23}^L\right)_U$ . Unfortunately, numerical calculations show that for all fiber-volume fractions between 0 and 1, both  $\left(\tau_{22}^L\right)_U$  and  $\left(\tau_{23}^L\right)_U$  obtained here are slightly higher than their corresponding values obtained previously.

4. Tractions equivalent to biaxial uniform tension  $\tau_{22}$  and  $\tau_{33}$

( $\tau_{22} \neq \tau_{33}$ ) on the composite specimen.

For definiteness assume  $\tau_{22} > \tau_{33}$ . Then following the ideas used in

Case 3, it can be shown that

$$(\tau_{22}^L)_L - (\tau_{33}^L)_L = 2k_b$$

$$(\tau_{22}^L)_U - (\tau_{33}^L)_U = 2(\tau_{23}^L)_U$$

5. The type of surface loading considered here is for  $\tau_{ij}$  in the follow-

ing form:

$$\tau_{ij} = \begin{bmatrix} 0 & \tau_{12} & 0 \\ \tau_{12} & \tau_{22} & 0 \\ 0 & 0 & 0 \end{bmatrix} \quad (10)$$

where the constant stress components  $\tau_{12}$  and  $\tau_{22}$  are related in the following way:

$$\tau_{12} = \alpha \tau_{22} \quad (11)$$

with  $\alpha \geq 0$ . This amounts to a proportional loading of combined uniform shear stresses  $\tau_{12}$  and uniform tensile stresses  $\tau_{22}$  on the boundary surface  $S$  of the specimen.

Since both  $\tau_{12}$  and  $\tau_{22}$  are assumed finite, it is obvious that  $\alpha = 0$  corresponds to the case where only uniform tensile stresses  $\tau_{22}$  are present. On the other hand,  $\alpha \rightarrow \infty$  corresponds to the case where the specimen is sub-



jected to uniform shear stresses  $\tau_{12}$ .

In lower bound construction, a uniform stress field of the form (2) supplemented by (3) is chosen as a statically admissible stress field to obtain lower bounds for the limit loads  $\tau_{22}^L$  and  $\tau_{12}^L$ , respectively. It turns out that,

$$\frac{(\tau_{22}^L)_L}{k_b} = \frac{1}{\sqrt{\frac{1}{3} + \alpha^2}}$$

and

(12)

$$\frac{(\tau_{12}^L)_L}{k_b} = \frac{\alpha}{\sqrt{\frac{1}{3} + \alpha^2}}$$

for  $\alpha \geq 0$ .

From Equation (12) it is obvious that for the special case where  $\alpha = 0$  (i. e. for uniform transverse stress  $\tau_{22}$  acting alone),

$$\frac{(\tau_{22}^L)_L}{k_b} = \sqrt{3} \quad (13)$$

In the case where  $\alpha \rightarrow \infty$ , corresponding to the case where the specimen is subjected to the uniform in-plane shear stresses  $\tau_{12}$  alone,

$$\lim_{\alpha \rightarrow \infty} \frac{(\tau_{12}^L)_L}{k_b} = 1$$

For upper bound construction, a kinematically admissible velocity field  $\vec{u}$  is chosen to be a linear combination of the two kinematically admissible velocity fields used to obtain  $(\tau_{12}^L)_U$  and  $(\tau_{22}^L)_U$ , respectively:

(a) In the region of the composite specimen not occupied by composite cylinders and on the boundary of the composite cylinders:

$$\vec{u} = \vec{u}^{(1)} + \vec{u}^{(2)} \quad (14)$$

where  $\vec{u}^{(1)} = (0, \gamma_1 x_1, 0)$

and  $\vec{u}^{(2)} = (0, \frac{\gamma_2}{2} x_2, -\frac{\gamma_2}{2} x_3)$

with

$$\gamma_1 = \omega \gamma_2 \quad (15)$$

where  $\omega$  is any real number.

(b) In any composite cylinder, the velocity field is the elastic displacement solution to the displacement boundary conditions (14) together with (15) prescribed with an additional condition that the fibrous core is rigid and the binder material is incompressible. In fact, the solution to this displacement boundary value problem can be obtained from the associated solutions to the individual problems connected with obtaining  $(\tau_{12}^L)_U$  and  $(\tau_{22}^L)_U$  by the principle of superposition.

Then an application of the upper bound theorem gives, for the case of constant  $\beta$  throughout the specimen

$$\frac{(\tau_{22}^L)_U}{k_b} = \frac{\sqrt{1+w^2} + v_1 (I_3 - \sqrt{1+w^2})}{\frac{1}{2} + \alpha w} \quad (16)$$

where

$$I_3 = \frac{1}{\pi(1-\beta^2)^3} \int_{\beta}^1 \int_0^{2\pi} R \sqrt{\Omega_1(w, \beta, R) + \Omega_2(w, \beta, R) \cos \theta + \Omega_3(\beta, R) \cos 2\theta} d\theta dR$$

$$\begin{aligned} \Omega_1(w, \beta, R) = & 4 \left\{ \frac{\beta^4}{R^4} \left[ (\beta^4 + \beta^2 + 1) - \frac{3}{2} (\beta^2 + 1) \frac{\beta^2}{R^2} \right]^2 \right. \\ & \left. + \left[ 3\beta^2 R^2 - \frac{(4\beta^4 + \beta^2 + 1)}{2} \right]^2 \right\} \\ & + w^2 (1 - \beta^2) \left( 1 + \frac{\beta^4}{R^4} \right) \end{aligned}$$

$$\Omega_2(w, \beta, R) = 2w^2 (1 - \beta^2)^4 \frac{\beta^2}{R^2}$$

and

$$\Omega_3(\beta, R) = 8 \frac{\beta^2}{R^2} \left[ (\beta^4 + \beta^2 + 1) - \frac{3}{2} (\beta^2 + 1) \frac{\beta^2}{R^2} \right] \left[ 3\beta^2 R^2 - \frac{(4\beta^4 + \beta^2 + 1)}{2} \right]$$

In the case of "random array", (16) reduces to

$$\frac{(\tau_{22}^L)_U}{k_b} = \frac{I_3}{\frac{1}{3} + \alpha w} \quad (17)$$

Since  $w$  in (15) is arbitrary, the lowest upper bound among the class of upper bounds in (17) will be obtained by minimizing the right-hand side of (17) with respect to  $w$ .

Thus,

$$(\tau_{22}^L)_U = \min_{\{w\}} \frac{\frac{k}{b} I_3}{\frac{1}{2} + \alpha w} \quad (18)$$

and

$$(\tau_{12}^L)_U = \min_{\{w\}} \frac{\frac{k}{b} \alpha I_3}{\frac{1}{2} + \alpha w}$$

will be chosen as the upper bounds for  $\tau_{22}^L$  and  $\tau_{12}^L$ , respectively.

Numerical calculation is performed to obtain  $(\tau_{22}^L)_U$  and  $(\tau_{12}^L)_U$  from (18) for different values of  $\beta$  and  $\alpha$ . It is interesting to note that in the numerical calculation, for any given  $\beta$ ,  $w$  which minimizes the right hand side of Equation (18) is a monotonic increasing function of  $\alpha$  but  $w \neq \alpha$  (except when  $\alpha = 0$ , then  $w = \alpha = 0$ ).

## APPENDIX B - Derivation of Equations for N. O. L. Ring Split-Dee Test Analysis

The assumptions are made that the N. O. L. ring exactly fits around the two dees at zero load and that there is no friction between dees and ring, so that the portion of the ring that remains in contact with the dees is subjected to essentially a radial pressure which induces a hoop tensile force  $P$  in the ring. This hoop tension produces a circumferential expansion  $\Delta_C$  of the ring, equivalent to:

$$\Delta_C = \frac{P}{E, A} (2\pi) \left( R_0 + \frac{t}{2} \right) \quad (1)$$

where

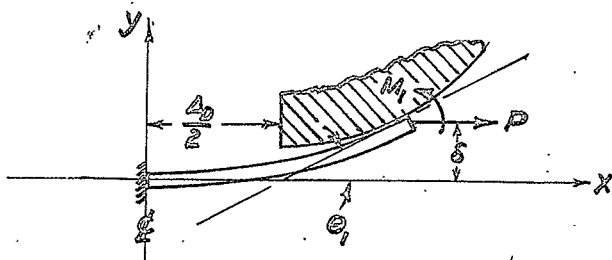
$E_1$	Young's modulus in hoop direction of ring
$A$	cross-sectional area of ring
$R_0$	initial inside radius of ring
$t$	ring thickness

This circumferential expansion is converted to a straight-line separation  $\Delta_D$  between the dees, so that

$$\Delta_D = \frac{P}{E, A} (\pi) \left( R_0 + \frac{t}{2} \right) \quad (2)$$

very nearly, and the problem is that of the analysis of a beam at the split in the

dees as sketched below:



That is, the beam is tangent to the dees at some point at a distance from the center line of the split between the Dees. At the centerline the beam is subjected to the tensile force  $P$  and a moment  $M_L$ . At the point of tangency the force  $P$  is also acting and a fictitious moment  $M_0$  is hypothesized of the magnitude required to form the ring to its initial radius of curvature  $R_0 + \frac{t}{2}$ .

So

$$M_0 = \frac{E I}{R_0 + \frac{t}{2}}$$

In other words the analysis considers the beam as initially straight when unstressed. The desired bending moment at the center line  $M_L$  will thus be found by subtraction of the fictitious moment  $M_0$  from  $M_L$ .

Selecting x-y coordinates as shown, we note that the moment  $M$  at any section of the beam is

$$M = -P(\delta - y) + M_0 \quad (3)$$

or

$$E, I \frac{d^2 y}{dx^2} = -P(\delta - y) + M_0 \quad (4)$$

Let

$$k^2 = \frac{P}{E, I} \quad (5)$$

By substitution (4) becomes

$$\frac{d^2 y}{dx^2} - k^2 y = -k^2 \delta + \frac{M_0}{E, I} \quad (6)$$

The solution of (6) is

$$y = \left( \delta - \frac{M_0}{E, I k^2} \right) (1 - \cosh kx) \quad (7)$$

Accordingly the slope  $\Theta_1$  at the point of tangency of the beam to the dees is

$$\Theta_1 = \tan^{-1} \left\{ - \left( \delta - \frac{M_0}{P} \right) \sqrt{\frac{P}{E, I}} \sinh \left( \frac{l}{\sqrt{E, I/P}} \right) \right\} \quad (8)$$

The deflection  $\delta$  is similarly found as

$$\delta = \frac{M_0}{P} \left\{ 1 - \frac{1}{\cosh \left( \frac{l}{\sqrt{E, I/P}} \right)} \right\} \quad (9)$$

Combining (8) and (9)

$$\theta_1 = \tan^{-1} \left\{ \frac{M_0}{P} \sqrt{\frac{P}{E_1 I}} \tanh \left( \frac{l}{\sqrt{E_1 I/P}} \right) \right\} \quad (10)$$

Because the beam is tangent to the dee at  $x = l$ , the angle  $\theta_1'$  subtended by the arc of the dee between the split and the point of contact may be found by trigonometry as

$$\theta_1' = \sin^{-1} \left\{ \frac{l - \frac{1}{2} \frac{P}{E_1 A} (\pi) (R_0 + \frac{r}{2})}{R_0 + \frac{r}{2}} \right\} \quad (11)$$

And

$$\theta_1 = \theta_1' \quad (12)$$

Finally, from (3) for  $y = 0$

$$M = M_E = M_0 - P\delta \quad (13)$$

Or by substitution of (9)

$$M_E = \frac{M_0}{\cosh \left( \frac{l}{\sqrt{E_1 I/P}} \right)} \quad (14)$$



Shear deflections may be included in the analysis by re-writing equation (7) as

$$y = \left\{ \delta - \frac{M_0}{P \left( \frac{1}{1 - \frac{nP}{G_2 A}} \right)} \right\} \left\{ 1 - \cosh \left( \frac{x}{\sqrt{E_1 I_1 / P}} \right) \right\} \quad (15)$$

For a rectangular section  $n = 1.2$ , and (15) becomes

$$y = \left\{ \delta - \frac{M_0}{P} \left( 1 - \frac{1.2}{G_{12}} \frac{P}{A} \right) \right\} \left\{ 1 - \cosh \left( \frac{x}{\sqrt{E_1 I_1 / P}} \right) \right\} \quad (16)$$

Analysis to include the effect of the straightaway on the racetrack specimen follows the same form as above, leading directly to the equations given in the text.

# 1-Direction Filaments

$$(\beta_L \neq \beta_T \neq \beta_{LT} \neq \beta_C)$$

$$A_1 = \frac{E_b(1-\nu_b)}{(1+\nu_b)(1-2\nu_b)}[1-\rho_{0L}\nu_f] + \frac{E_f(1-\nu_f)}{(1+\nu_f)(1-2\nu_f)}[\rho_{0L}\nu_f]$$

$$A_2=A_3 = \frac{\nu_b E_b}{(1+\nu_b)(1-2\nu_b)}[1-\rho_{0LT}\nu_f] + \frac{\nu_f E_f}{(1+\nu_f)(1-2\nu_f)}[\rho_{0LT}\nu_f]$$

$$A_5 = \frac{\nu_b E_b}{(1+\nu_b)(1-2\nu_b)}[1-\rho_{0C}\nu_f] + \frac{\nu_f E_f}{(1+\nu_f)(1-2\nu_f)}[\rho_{0C}\nu_f]$$

$$A_4=A_6 = \frac{E_b(1-\nu_b)}{(1+\nu_b)(1-2\nu_b)}[1-\rho_{0T}\nu_f] + \frac{E_f(1-\nu_f)}{(1+\nu_f)(1-2\nu_f)}[\rho_{0T}\nu_f]$$

$$A_7=A_9 = G_b[1-\rho_{0'}\nu_f] + G_f[\rho_{0'}\nu_f]$$

$$A_8 = G_b[1-\rho_{0''}\nu_f] + G_f[\rho_{0''}\nu_f]$$

Table 1. - Generalized equations for compliances of composites having uni-directional reinforcing filaments in the 1'-direction (from Ref. 1).

## 1-Direction Filaments

*Interrelationships among constants for  
transverse isotropy*

$$A_1 = E_1 \left[ \frac{1 - \nu_{23}}{1 - \nu_{23} - 2\nu_{12}\nu_{21}} \right]$$

$$A_2 = A_3 = \frac{\nu_{21} E_2}{1 - \nu_{23} - 2\nu_{12}\nu_{21}}$$

$$A_5 = A_4 - 2A_8$$

$$A_4 = A_6 = \frac{E_2 (1 - \nu_{12}\nu_{21})}{(1 - \nu_{23} - 2\nu_{12}\nu_{21})(1 + \nu_{23})}$$

$$A_7 = A_9 = G_{12}$$

$$A_8 = G_{23}$$

Table 2. - Relationships among elastic constants and compliances for uni-directional reinforcement for use in evaluations of the various  $\beta$ 's in Table 1 (from Ref. 1).

$$\beta_{oL} = \frac{E_1 \left( \frac{1-\nu_{23}}{1-\nu_{23}-2\nu_{12}\nu_{21}} \right) - E_b \left( \frac{1-\nu_b}{1-\nu_b-2\nu_b^2} \right) (1-\nu_f)}{E_f \left( \frac{1-\nu_f}{1-\nu_f-2\nu_f^2} \right) (\nu_f)}$$

$$\beta_{oT} = \frac{E_2 \left( \frac{1-\nu_{12}\nu_{21}}{(1-\nu_{23}-2\nu_{12}\nu_{21})(1+\nu_{23})} \right) - E_b \left( \frac{1-\nu_b}{1-\nu_b-2\nu_b^2} \right) (1-\nu_f)}{E_f \left( \frac{1-\nu_f}{1-\nu_f-2\nu_f^2} \right) (\nu_f)}$$

$$\beta_{oLT} = \frac{E_2 \left( \frac{\nu_{21}}{1-\nu_{23}-2\nu_{12}\nu_{21}} \right) - E_b \left( \frac{\nu_b}{1-\nu_b-2\nu_b^2} \right) (1-\nu_f)}{E_f \left( \frac{\nu_f}{1-\nu_f-2\nu_f^2} \right) (\nu_f)}$$

$$\beta_{oG} = \frac{E_2 \left( \frac{1-\nu_{12}\nu_{21}}{(1-\nu_{23}-2\nu_{12}\nu_{21})(1+\nu_{23})} \right) - 2G_{23} - E_b \left( \frac{\nu_b}{1-\nu_b-2\nu_b^2} \right) (1-\nu_f)}{E_f \left( \frac{\nu_f}{1-\nu_f-2\nu_f^2} \right) (\nu_f)}$$

$$\beta_o' = \frac{G_{12} - G_b (1-\nu_f)}{G_f (\nu_f)}$$

$$\beta_o'' = \frac{G_{23} - G_b (1-\nu_f)}{G_f (\nu_f)}$$

Table 3. - Equations for the transverse effectiveness factors ( $\beta$ ) in terms of the elastic constants for uni-directional reinforcement (equations of Table 2 solved in terms of  $\beta$  for  $\beta_o$  values equal to unity).

$$\begin{aligned}
A_1 = & \frac{E_b(1-\nu_b)}{(1+\nu_b)(1-2\nu_b)} + \left[ \frac{E_{f_1}(1-\nu_{f_1})}{(1+\nu_{f_1})(1-2\nu_{f_1})} \rho_{a_{L_1}} - \frac{E_b(1-\nu_b)}{(1+\nu_b)(1-2\nu_b)} \rho_{a_{L_1}} \right] (\nu_{f_1}) \\
& + \left[ \frac{E_{f_2}(1-\nu_{f_2})}{(1+\nu_{f_2})(1-2\nu_{f_2})} \rho_{a_{L_2}} - \frac{E_b(1-\nu_b)}{(1+\nu_b)(1-2\nu_b)} \rho_{a_{L_2}} \right] (\nu_{f_2}) \\
& + \left[ \frac{E_{f_3}(1-\nu_{f_3})}{(1+\nu_{f_3})(1-2\nu_{f_3})} \rho_{a_{L_3}} - \frac{E_b(1-\nu_b)}{(1+\nu_b)(1-2\nu_b)} \rho_{a_{L_3}} \right] (\nu_{f_3}) \\
& + \left[ \frac{E_{f_4}(1-\nu_{f_4})}{(1+\nu_{f_4})(1-2\nu_{f_4})} \right] \left\{ \rho_{a_{L_4}} \cos^2 \psi + \rho_{a_{L_5}} \sin^2 \psi + \left[ \nu_{f_4} \rho_{a_{L_4}} + (1-2\nu_{f_4}) \rho_{a_{L_5}}' \right] \left[ \frac{2 \sin^2 \psi \cos^2 \psi}{1-\nu_{f_4}} \right] \right\} (\nu_{f_4}) \\
& - \left[ \frac{E_b(1-\nu_b)}{(1+\nu_b)(1-2\nu_b)} \right] \left\{ \rho_{a_{L_4}} \cos^2 \psi + \rho_{a_{L_5}} \sin^2 \psi + \left[ \nu_b \rho_{a_{L_4}} + (1-2\nu_b) \rho_{a_{L_5}}' \right] \left[ \frac{2 \sin^2 \psi \cos^2 \psi}{1-\nu_b} \right] \right\} (\nu_b) \\
A_2 = & \frac{\nu_b E_b}{(1+\nu_b)(1-2\nu_b)} + \left[ \frac{\nu_{f_1} E_{f_1}}{(1+\nu_{f_1})(1-2\nu_{f_1})} \rho_{a_{L_1}} - \frac{\nu_b E_b}{(1+\nu_b)(1-2\nu_b)} \rho_{a_{L_1}} \right] (\nu_{f_1}) \\
& + \left[ \frac{\nu_{f_2} E_{f_2}}{(1+\nu_{f_2})(1-2\nu_{f_2})} \rho_{a_{L_2}} - \frac{\nu_b E_b}{(1+\nu_b)(1-2\nu_b)} \rho_{a_{L_2}} \right] (\nu_{f_2}) \\
& + \left[ \frac{\nu_{f_3} E_{f_3}}{(1+\nu_{f_3})(1-2\nu_{f_3})} \rho_{a_{L_3}} - \frac{\nu_b E_b}{(1+\nu_b)(1-2\nu_b)} \rho_{a_{L_3}} \right] (\nu_{f_3}) \\
& + \left[ \frac{E_{f_4}(1-\nu_{f_4})}{(1+\nu_{f_4})(1-2\nu_{f_4})} \right] \left\{ \left[ \rho_{a_{L_4}} + \rho_{a_{L_5}} - 2 \left( \frac{1-2\nu_{f_4}}{1-\nu_{f_4}} \right) (\rho_{a_{L_5}}') \right] (\cos^2 \psi \cos^2 \psi) \right. \\
& \quad \left. + \frac{\nu_{f_4}}{1-\nu_{f_4}} \left[ \rho_{a_{L_4}} (\sin^2 \psi \cos^2 \psi + \cos^2 \psi \cos^2 \psi + \cos^2 \psi) + \rho_{a_{L_5}} \cos^2 \psi \right] \right\} (\nu_{f_4}) \\
& - \left[ \frac{E_b(1-\nu_b)}{(1+\nu_b)(1-2\nu_b)} \right] \left\{ \left[ \rho_{a_{L_4}} + \rho_{a_{L_5}} - 2 \left( \frac{1-2\nu_b}{1-\nu_b} \right) (\rho_{a_{L_5}}') \right] (\cos^2 \psi \cos^2 \psi) \right. \\
& \quad \left. + \frac{\nu_b}{1-\nu_b} \left[ \rho_{a_{L_4}} (\sin^2 \psi \cos^2 \psi + \cos^2 \psi \cos^2 \psi + \cos^2 \psi) + \rho_{a_{L_5}} \cos^2 \psi \right] \right\} (\nu_b)
\end{aligned}$$

Table 4. - Generalized equations for the compliances of three-dimensionally reinforced composites having three orthogonal planes of symmetry.

$$\begin{aligned}
A_3 = & \frac{v_b E_b}{(1+v_b)(1-2v_b)} + \left[ \frac{v_{f_1} E_{f_1}}{(1+v_{f_1})(1-2v_{f_1})} \beta_{oLT_1} - \frac{v_b E_b}{(1+v_b)(1-2v_b)} \beta_{oLT} \right] (v_{f_1}) \\
& + \left[ \frac{v_{f_2} E_{f_2}}{(1+v_{f_2})(1-2v_{f_2})} \beta_{oG_2} - \frac{v_b E_b}{(1+v_b)(1-2v_b)} \beta_{oG} \right] (v_{f_2}) \\
& + \left[ \frac{v_{f_3} E_{f_3}}{(1+v_{f_3})(1-2v_{f_3})} \beta_{oLT_3} - \frac{v_b E_b}{(1+v_b)(1-2v_b)} \beta_{oLT} \right] (v_{f_3}) \\
& + \left[ \frac{E_{f_s}(1-v_{f_s})}{(1+v_{f_s})(1-2v_{f_s})} \left\{ \left[ (\beta_{o_s} + \beta_{o_{\tau_s}}) - 2 \left( \frac{1-2v_{f_s}}{1-v_{f_s}} \right) (\beta_{o_s}') \right] (\cos^2 \phi \cos^2 \Omega) \right. \right. \\
& \quad \left. \left. + \frac{v_{f_s}}{1-v_{f_s}} \left[ \beta_{o_{LT_s}} \left( \sin^2 \phi \cos^2 \Omega + \cos^2 \phi \right) (\cos^2 \phi \cos^2 \Omega + \cos^2 \phi) \right] + \beta_{o_s} \cos^2 \phi \right\} \right] (v_{f_s}) \\
& - \left[ \frac{E_b(1-v_b)}{(1+v_b)(1-2v_b)} \left\{ \left[ (\beta_{o_s} + \beta_{o_{\tau_s}}) - 2 \left( \frac{1-2v_b}{1-v_b} \right) (\beta_{o_s}') \right] (\cos^2 \phi \cos^2 \Omega) \right. \right. \\
& \quad \left. \left. + \frac{v_b}{1-v_b} \left[ \beta_{o_{LT}} \left( \sin^2 \phi \cos^2 \Omega + \cos^2 \phi \right) (\cos^2 \phi \cos^2 \Omega + \cos^2 \phi) \right] + \beta_{o_s} \cos^2 \phi \right\} \right] (v_{f_s})
\end{aligned}$$

Table 4. - (Cont.)

$$\begin{aligned}
A_4 = & \frac{E_b(1-\nu_b)}{(1+\nu_b)(1-2\nu_b)} + \left[ \frac{E_f(1-\nu_f)}{(1+\nu_f)(1-2\nu_f)} \rho_{0f} - \frac{E_b(1-\nu_b)}{(1+\nu_b)(1-2\nu_b)} \rho_{0f} \right] (\nu_f) \\
& + \left[ \frac{E_{f_2}(1-\nu_{f_2})}{(1+\nu_{f_2})(1-2\nu_{f_2})} \rho_{0f_2} - \frac{E_b(1-\nu_b)}{(1+\nu_b)(1-2\nu_b)} \rho_{0f_2} \right] (\nu_{f_2}) \\
& + \left[ \frac{E_{f_3}(1-\nu_{f_3})}{(1+\nu_{f_3})(1-2\nu_{f_3})} \rho_{0f_3} - \frac{E_b(1-\nu_b)}{(1+\nu_b)(1-2\nu_b)} \rho_{0f_3} \right] (\nu_{f_3}) \\
& + \left[ \frac{E_f(1-\nu_f)}{(1+\nu_f)(1-2\nu_f)} \right] \left\{ \rho_{f_3} \cos^2 \varphi + \rho_{f_2} \left[ \frac{\cos^2 \varphi \cos^2 \Omega + \cos^2 \Omega}{\sin^2 \varphi} \right] \right. \\
& \quad + \frac{2\nu_{f_2}}{1-\nu_{f_2}} \left[ \rho_{f_2} \left( \frac{\cos^2 \varphi \cos^2 \Omega + \cos^2 \Omega \cos^2 \Omega}{\sin^2 \varphi} \right) + \rho_{f_3} \left( \frac{\cos^2 \varphi \cos^2 \Omega \cos^2 \Omega}{\sin^2 \varphi} \right) \right] \\
& \quad + \frac{2(1-2\nu_{f_2})}{1-\nu_{f_2}} \left[ \rho_{f_2} \left( \frac{\cos^2 \varphi \cos^2 \Omega + \cos^2 \Omega \cos^2 \Omega}{\sin^2 \varphi} \right) + \rho_{f_3} \left( \frac{\cos^2 \varphi \cos^2 \Omega \cos^2 \Omega}{\sin^2 \varphi} \right) \right] \left\} (\nu_{f_2}) \right. \\
& - \left[ \frac{E_b(1-\nu_b)}{(1+\nu_b)(1-2\nu_b)} \right] \left\{ \rho_{f_2} \cos^2 \varphi + \rho_{f_3} \left[ \frac{\cos^2 \varphi \cos^2 \Omega + \cos^2 \Omega}{\sin^2 \varphi} \right] \right. \\
& \quad + \frac{2\nu_b}{1-\nu_b} \left[ \rho_{f_2} \left( \frac{\cos^2 \varphi \cos^2 \Omega + \cos^2 \Omega \cos^2 \Omega}{\sin^2 \varphi} \right) + \rho_{f_3} \left( \frac{\cos^2 \varphi \cos^2 \Omega \cos^2 \Omega}{\sin^2 \varphi} \right) \right] \\
& \quad + \frac{2(1-2\nu_b)}{1-\nu_b} \left[ \rho_{f_2} \left( \frac{\cos^2 \varphi \cos^2 \Omega + \cos^2 \Omega \cos^2 \Omega}{\sin^2 \varphi} \right) + \rho_{f_3} \left( \frac{\cos^2 \varphi \cos^2 \Omega \cos^2 \Omega}{\sin^2 \varphi} \right) \right] \left\} (\nu_{f_3}) \right.
\end{aligned}$$

$$\begin{aligned}
A_5 = & \frac{\nu_b E_b}{(1+\nu_b)(1-2\nu_b)} + \left[ \frac{\nu_f E_f}{(1+\nu_f)(1-2\nu_f)} \rho_{0f} - \frac{\nu_b E_b}{(1+\nu_b)(1-2\nu_b)} \rho_{0f} \right] (\nu_f) \\
& + \left[ \frac{\nu_{f_2} E_{f_2}}{(1+\nu_{f_2})(1-2\nu_{f_2})} \rho_{0f_2} - \frac{\nu_b E_b}{(1+\nu_b)(1-2\nu_b)} \rho_{0f_2} \right] (\nu_{f_2}) \\
& + \left[ \frac{\nu_{f_3} E_{f_3}}{(1+\nu_{f_3})(1-2\nu_{f_3})} \rho_{0f_3} - \frac{\nu_b E_b}{(1+\nu_b)(1-2\nu_b)} \rho_{0f_3} \right] (\nu_{f_3}) \\
& + \left[ \frac{E_{f_2}(1-\nu_{f_2})}{(1+\nu_{f_2})(1-2\nu_{f_2})} \right] \left\{ \left[ \rho_{f_2} + \rho_{f_3} \right] - 2 \left( \frac{1-2\nu_{f_2}}{1-\nu_{f_2}} \right) \left[ \rho_{f_2}' + \rho_{f_3}' \frac{\cos^2 \varphi}{\sin^2 \varphi} \right] \left( \cos^2 \varphi \cos^2 \Omega \right) \right. \\
& \quad + \frac{\nu_{f_2}}{1-\nu_{f_2}} \left[ \rho_{f_2} \left( \frac{\cos^2 \varphi \cos^2 \Omega \cos^2 \Omega + \cos^2 \Omega \cos^2 \Omega}{\sin^2 \varphi} \right) + \rho_{f_3} \left( \frac{\cos^2 \varphi \cos^2 \Omega \cos^2 \Omega}{\sin^2 \varphi} \right) \right] \left\} (\nu_{f_2}) \right. \\
& - \left[ \frac{E_b(1-\nu_b)}{(1+\nu_b)(1-2\nu_b)} \right] \left\{ \left[ \rho_{f_2} + \rho_{f_3} \right] - 2 \left( \frac{1-2\nu_b}{1-\nu_b} \right) \left[ \rho_{f_2}' + \rho_{f_3}' \frac{\cos^2 \varphi}{\sin^2 \varphi} \right] \left( \cos^2 \varphi \cos^2 \Omega \right) \right. \\
& \quad + \frac{\nu_b}{1-\nu_b} \left[ \rho_{f_2} \left( \frac{\cos^2 \varphi \cos^2 \Omega \cos^2 \Omega + \cos^2 \Omega \cos^2 \Omega}{\sin^2 \varphi} \right) + \rho_{f_3} \left( \frac{\cos^2 \varphi \cos^2 \Omega \cos^2 \Omega}{\sin^2 \varphi} \right) \right] \left\} (\nu_{f_3}) \right.
\end{aligned}$$

Table 4. - (Cont.)

$$\begin{aligned}
A_6 = & \frac{E_b(1-\nu_b)}{(1+\nu_b)(1-2\nu_b)} + \left[ \frac{E_f(1-\nu_f)}{(1+\nu_f)(1-2\nu_f)} \rho_{\tau_f} - \frac{E_b(1-\nu_b)}{(1+\nu_b)(1-2\nu_b)} \rho_{\tau_b} \right] (\nu_{f_1}) \\
& + \left[ \frac{E_{f_2}(1-\nu_{f_2})}{(1+\nu_{f_2})(1-2\nu_{f_2})} \rho_{\tau_{f_2}} - \frac{E_b(1-\nu_b)}{(1+\nu_b)(1-2\nu_b)} \rho_{\tau_b} \right] (\nu_{f_2}) \\
& + \left[ \frac{E_{f_3}(1-\nu_{f_3})}{(1+\nu_{f_3})(1-2\nu_{f_3})} \rho_{\tau_{f_3}} - \frac{E_b(1-\nu_b)}{(1+\nu_b)(1-2\nu_b)} \rho_{\tau_b} \right] (\nu_{f_3}) \\
& + \left[ \frac{E_{f_5}(1-\nu_{f_5})}{(1+\nu_{f_5})(1-2\nu_{f_5})} \right] \left\{ \rho_{\tau_{f_5}} \cos^2 \Omega + \rho_{\tau_b} \left[ \frac{\cos^2 \psi \cos^2 \Omega + \cos^2 \psi}{\sin^2 \psi} \right] \right. \\
& \quad \left. + \frac{2\nu_{f_5}}{1-\nu_{f_5}} \left[ \rho_{\tau_{f_5}} \left( \frac{\cos^2 \psi \cos^2 \Omega + \cos^2 \psi \cos^2 \Omega}{\sin^2 \psi} \right) + \rho_{\tau_b} \left( \frac{\cos^2 \psi \cos^2 \psi \cos^2 \Omega}{\sin^2 \psi} \right) \right] \right. \\
& \quad \left. + \frac{2(1-2\nu_{f_5})}{1-\nu_{f_5}} \left[ \rho_{\tau_{f_5}} \left( \frac{\cos^2 \psi \cos^2 \Omega + \cos^2 \psi \cos^2 \Omega}{\sin^2 \psi} \right) + \rho_{\tau_b} \left( \frac{\cos^2 \psi \cos^2 \psi \cos^2 \Omega}{\sin^2 \psi} \right) \right] \right\} (\nu_{f_5}) \\
& - \left[ \frac{E_b(1-\nu_b)}{(1+\nu_b)(1-2\nu_b)} \right] \left\{ \rho_{\tau_b} \cos^2 \Omega + \rho_{\tau_f} \left[ \frac{\cos^2 \psi \cos^2 \Omega + \cos^2 \psi}{\sin^2 \psi} \right] \right. \\
& \quad \left. + \frac{2\nu_b}{1-\nu_b} \left[ \rho_{\tau_b} \left( \frac{\cos^2 \psi \cos^2 \Omega + \cos^2 \psi \cos^2 \Omega}{\sin^2 \psi} \right) + \rho_{\tau_f} \left( \frac{\cos^2 \psi \cos^2 \psi \cos^2 \Omega}{\sin^2 \psi} \right) \right] \right. \\
& \quad \left. + \frac{2(1-2\nu_b)}{1-\nu_b} \left[ \rho_{\tau_b} \left( \frac{\cos^2 \psi \cos^2 \Omega + \cos^2 \psi \cos^2 \Omega}{\sin^2 \psi} \right) + \rho_{\tau_f} \left( \frac{\cos^2 \psi \cos^2 \psi \cos^2 \Omega}{\sin^2 \psi} \right) \right] \right\} (\nu_b)
\end{aligned}$$

$$\begin{aligned}
A_7 = & G_f \rho_{\tau_f}' - G_b \rho_{\tau_b}' \left[ (\nu_{f_1}) + \left[ G_{f_2} \rho_{\tau_{f_2}}' - G_b \rho_{\tau_b}' \right] (\nu_{f_2}) \right. \\
& + \left[ G_{f_3} \rho_{\tau_{f_3}}'' - G_b \rho_{\tau_b}'' \right] (\nu_{f_3}) + \left[ G_{f_5} \rho_{\tau_{f_5}}'' - G_b \rho_{\tau_b}'' \right] (\cos^2 \Omega) (\nu_{f_5}) \\
& + \left[ G_{f_5} \rho_{\tau_{f_5}}' - G_b \rho_{\tau_b}' \right] \left[ \frac{\cos^2 \psi (\cos^2 \psi - \sin^2 \psi) + \cos^2 \psi \cos^2 \Omega}{\sin^2 \psi} \right] (\nu_{f_5}) \\
& + \left[ \frac{E_{f_5}(1-\nu_{f_5})}{(1+\nu_{f_5})(1-2\nu_{f_5})} \right] \left[ \rho_{\tau_{f_5}} + \rho_{\tau_b} - \left( \frac{2\nu_{f_5}}{1-\nu_{f_5}} \right) \rho_{\tau_{f_5}} \right] \left[ \cos^2 \psi \cos^2 \psi \right] (\nu_{f_5}) \\
& - \left[ \frac{E_b(1-\nu_b)}{(1+\nu_b)(1-2\nu_b)} \right] \left[ \rho_{\tau_b} + \rho_{\tau_f} - \left( \frac{2\nu_b}{1-\nu_b} \right) \rho_{\tau_{f_1}} \right] \left[ \cos^2 \psi \cos^2 \psi \right] (\nu_b)
\end{aligned}$$

Table 4. - (Cont.)



$$\begin{aligned}
A_g = & G_b + \left[ G_f \rho_a'' - G_b \rho_a'' \right] \left( \nu_f \right) + \left[ G_f \rho_a' - G_b \rho_a' \right] \left( \nu_f \right) \\
& + \left[ G_f \rho_a' - G_b \rho_a' \right] \left( \nu_f \right) + \left[ G_f \rho_a'' - G_b \rho_a'' \right] \left[ \frac{\cos^2 \phi (\cos^2 \psi - \cos^2 \Omega)}{\sin^2 \phi} \right] \left( \nu_f \right) \\
& + \left[ G_f \rho_a' - G_b \rho_a' \right] \left[ \frac{2 \cos^2 \phi \cos^2 \psi \cos^2 \Omega + (\cos^2 \psi - \cos^2 \Omega)^2}{\sin^2 \phi} \right] \left( \nu_f \right) \\
& + \left[ \frac{E_b (1 - \nu_b)}{(1 + \nu_b)(1 - 2\nu_b)} \right] \left[ \rho_{a_z} + \left( \frac{1 + \sin^2 \phi \cos^2 \psi}{\sin^2 \phi} \right) \rho_{a_r} \right. \\
& \quad \left. + \frac{2\nu_b}{1 - \nu_b} \left( \left( 1 - \frac{1}{\sin^2 \phi} \right) \rho_{a_z} - \left( \frac{1}{\sin^2 \phi} \right) \rho_{a_r} \right) \left( \frac{\cos \phi}{\sin \phi} \right) \right] \left[ \cos^2 \psi \cos^2 \Omega \right] \left( \nu_f \right) \\
& - \left[ \frac{E_b (1 - \nu_b)}{(1 + \nu_b)(1 - 2\nu_b)} \right] \left[ \rho_{a_z} + \left( \frac{1 + \sin^2 \phi \cos^2 \psi}{\sin^2 \phi} \right) \rho_{a_r} \right. \\
& \quad \left. + \frac{2\nu_b}{1 - \nu_b} \left( \left( 1 - \frac{1}{\sin^2 \phi} \right) \rho_{a_z} - \left( \frac{1}{\sin^2 \phi} \right) \rho_{a_r} \right) \left( \frac{\cos \phi}{\sin \phi} \right) \right] \left[ \cos^2 \psi \cos^2 \Omega \right] \left( \nu_f \right)
\end{aligned}$$

$$\begin{aligned}
A_g = & G_b + \left[ G_f \rho_a' - G_b \rho_a' \right] \left( \nu_f \right) + \left[ G_f \rho_a'' - G_b \rho_a'' \right] \left( \nu_f \right) \\
& + \left[ G_f \rho_a' - G_b \rho_a' \right] \left( \nu_f \right) + \left[ G_f \rho_a'' - G_b \rho_a'' \right] \left[ \cos^2 \phi \right] \left( \nu_f \right) \\
& + \left[ G_f \rho_a' - G_b \rho_a' \right] \left[ \frac{\cos^2 \Omega (\cos^2 \phi - \sin^2 \phi) + \cos^2 \phi \cos^2 \psi}{\sin^2 \phi} \right] \left( \nu_f \right) \\
& + \left[ \frac{E_b (1 - \nu_b)}{(1 + \nu_b)(1 - 2\nu_b)} \right] \left[ \rho_{a_z} + \left( \frac{2\nu_b}{1 - \nu_b} \right) \rho_{a_r} \right] \left[ \cos^2 \phi \cos^2 \Omega \right] \left( \nu_f \right) \\
& - \left[ \frac{E_b (1 - \nu_b)}{(1 + \nu_b)(1 - 2\nu_b)} \right] \left[ \rho_{a_z} + \left( \frac{2\nu_b}{1 - \nu_b} \right) \rho_{a_r} \right] \left[ \cos^2 \phi \cos^2 \Omega \right] \left( \nu_f \right)
\end{aligned}$$

Table 4. - (Cont.)

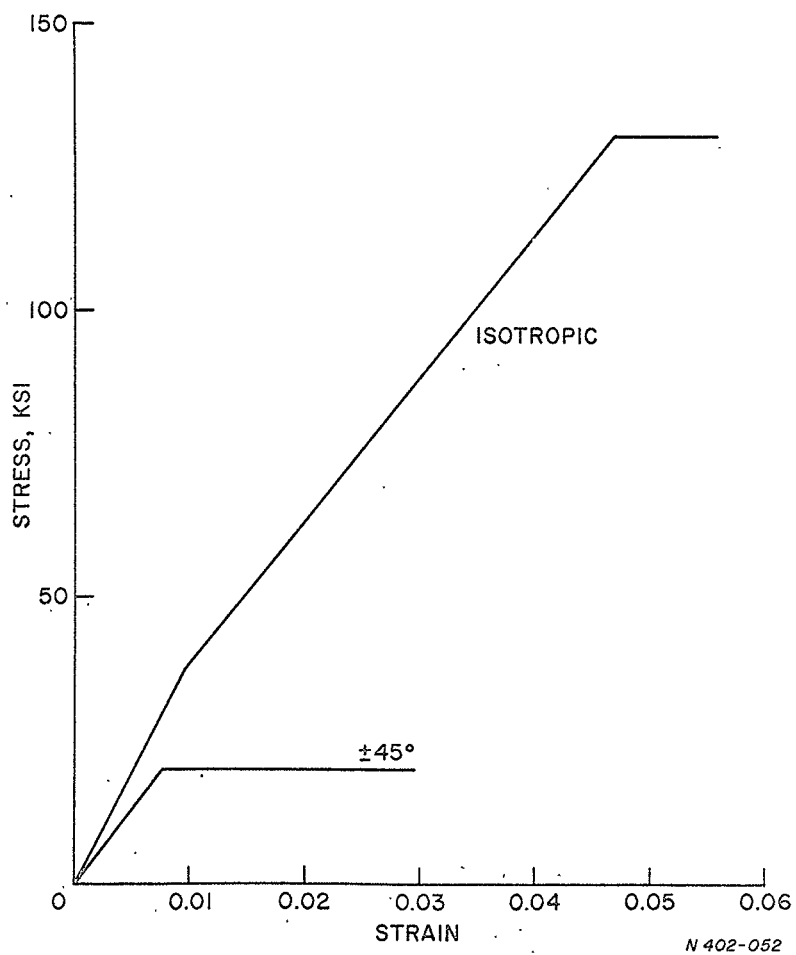


Figure 1. Calculated Stress-strain Curves for E-Glass and Epoxy Composite Laminates.

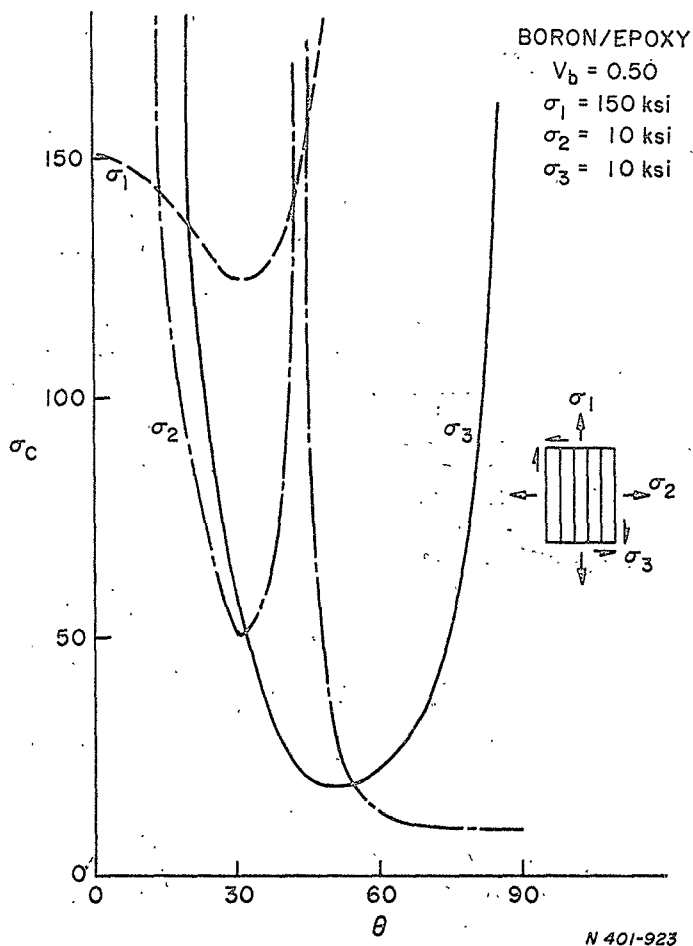


Figure 2. Yield Strength of a Symmetric Bi-axial Composite Laminate for Failure Modes Involving Each of the Principal Lamina Stresses.

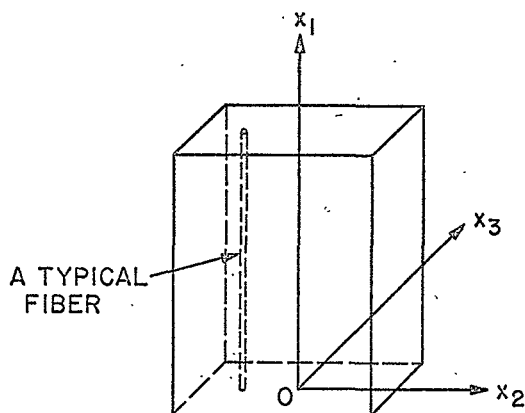


Figure 3. Composite Specimen for Limit Analysis. (Fibers in  $X_1$ -Direction).

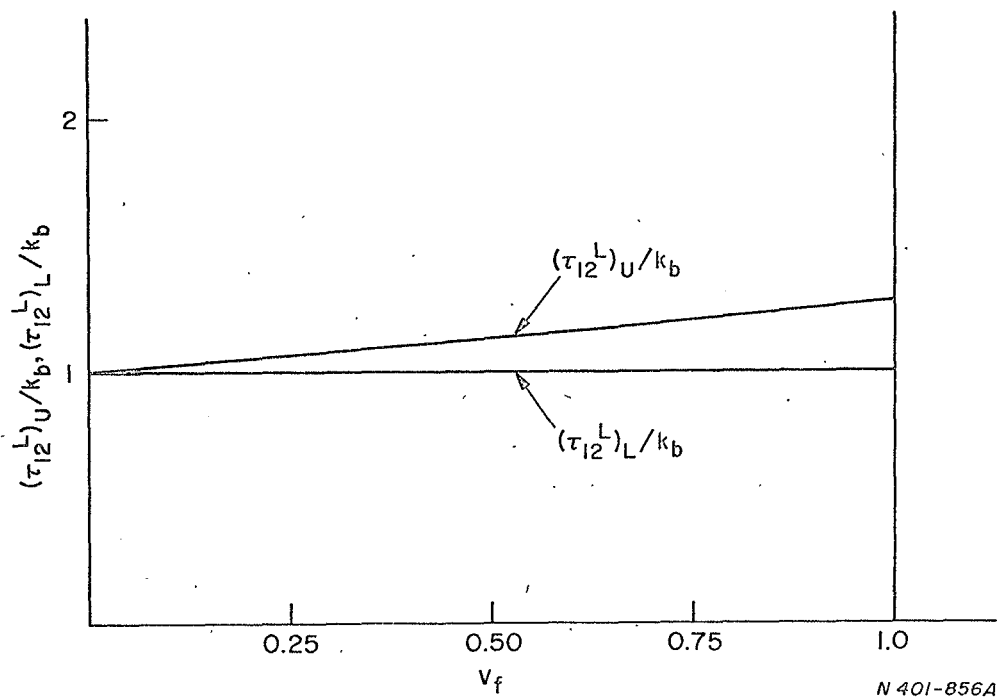
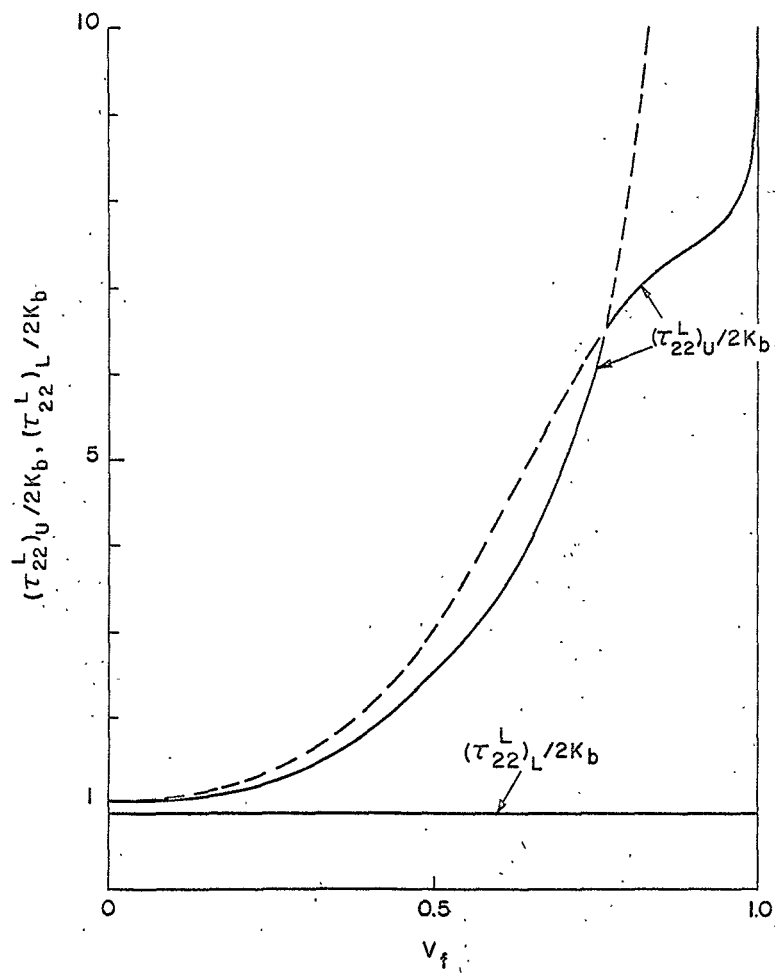


Figure 4. Bounds on the Limit Load for In-plane Shear.



N 402-132

Figure 5. Bounds on the Limit Load for Transverse Tension.

Figure 6. Bounds on the Interaction Curves for In-plane Shear and Transverse Tension for Various Fiber Volume Fractions.

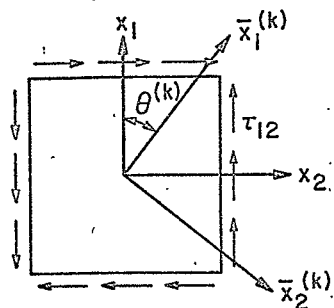


Figure 7. The  $K^{\text{th}}$  Layer in a Laminate for the Limit Analysis Model.

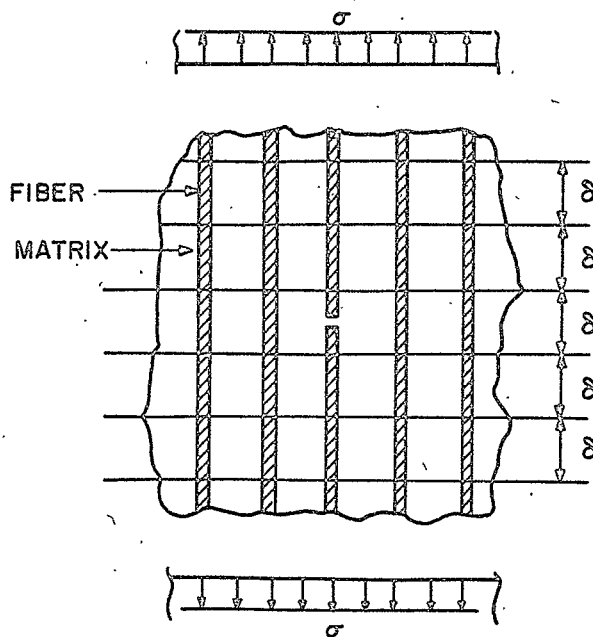


Figure 8. Tensile Failure Model for a Composite Reinforced by Continuous Fibers.



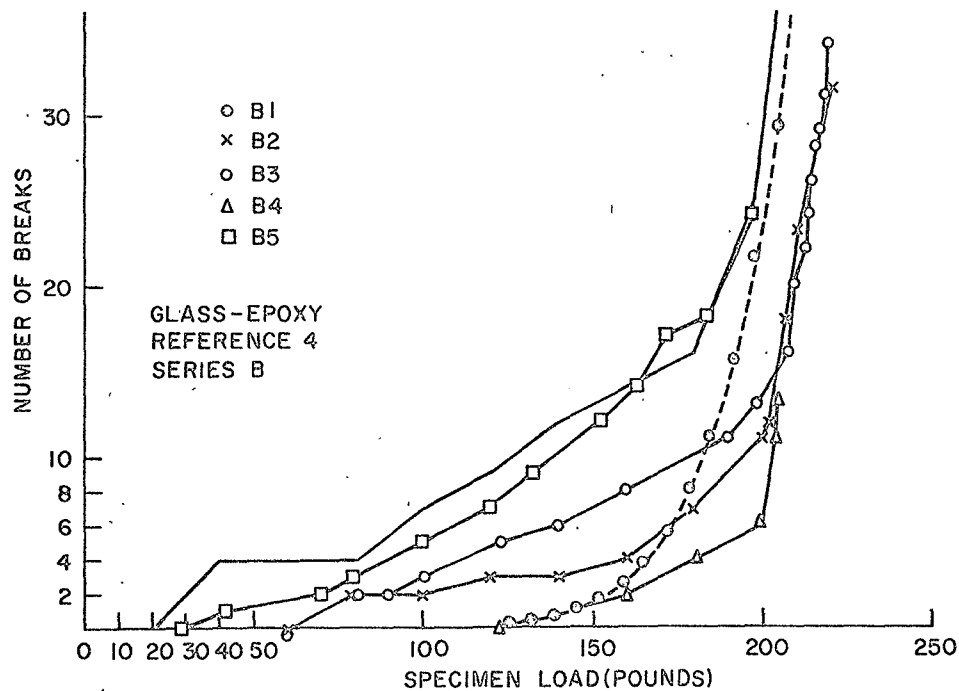


Figure 9. Number of Breaks as a Function of Applied Load (Ref. 4, Series B).

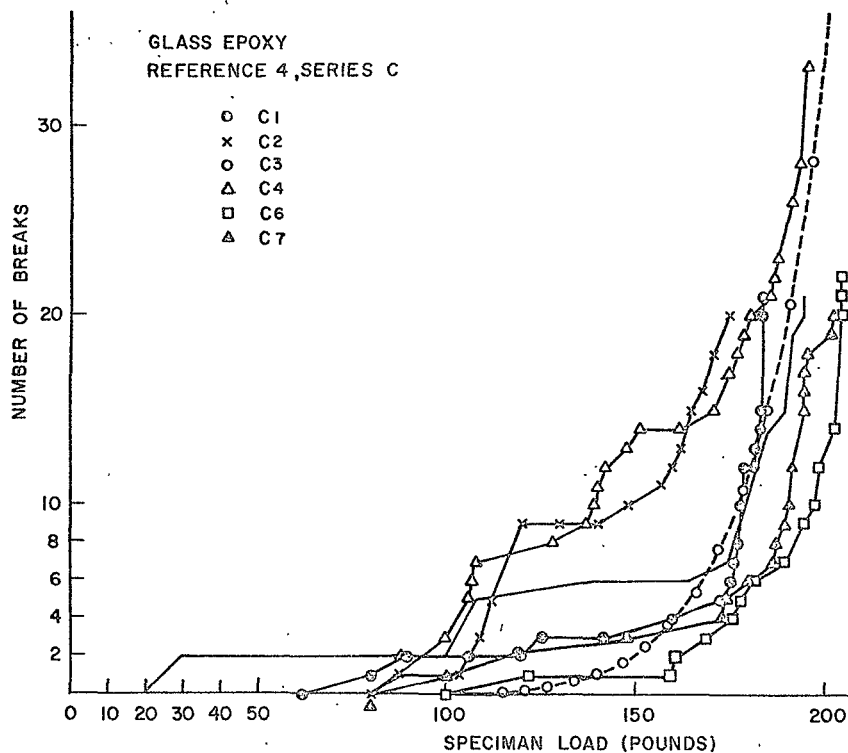


Figure 10. Number of Breaks as a Function of Applied Load (Ref. 4, Series C).

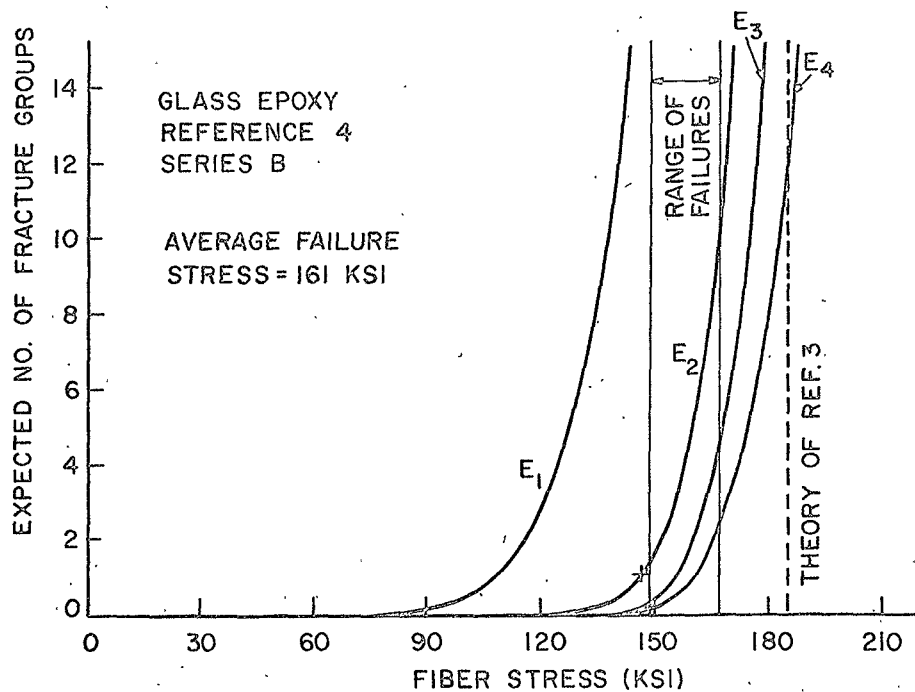


Figure 11. Expected Number of Groups of Fractures as a Function of Applied Load (Ref. 4, Series B).

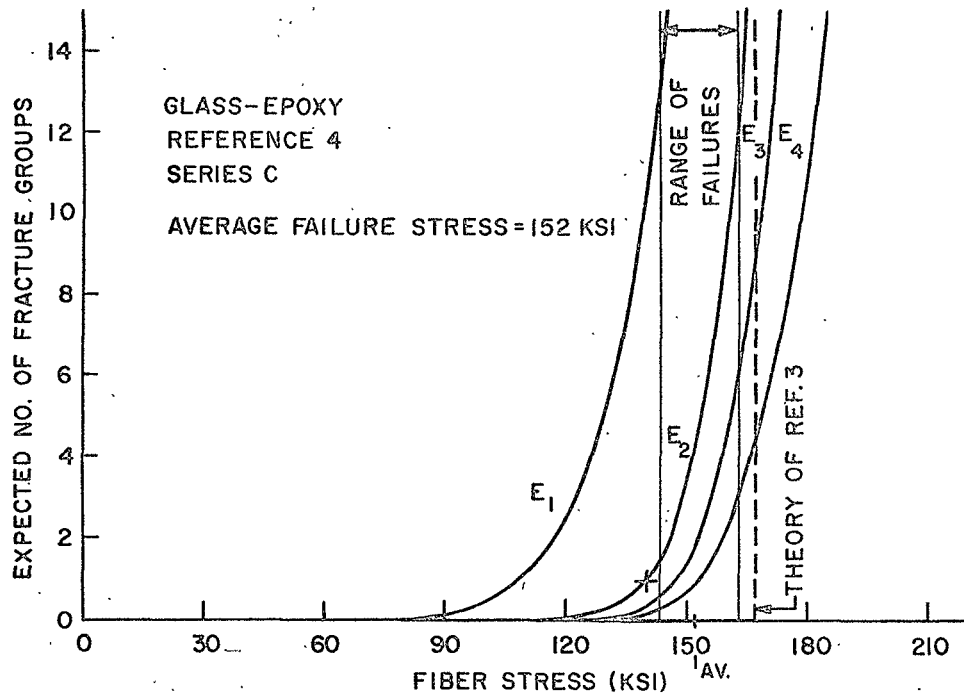


Figure 12. Expected Number of Groups of Fractures as a Function of Applied Load (Ref. 4, Series C).

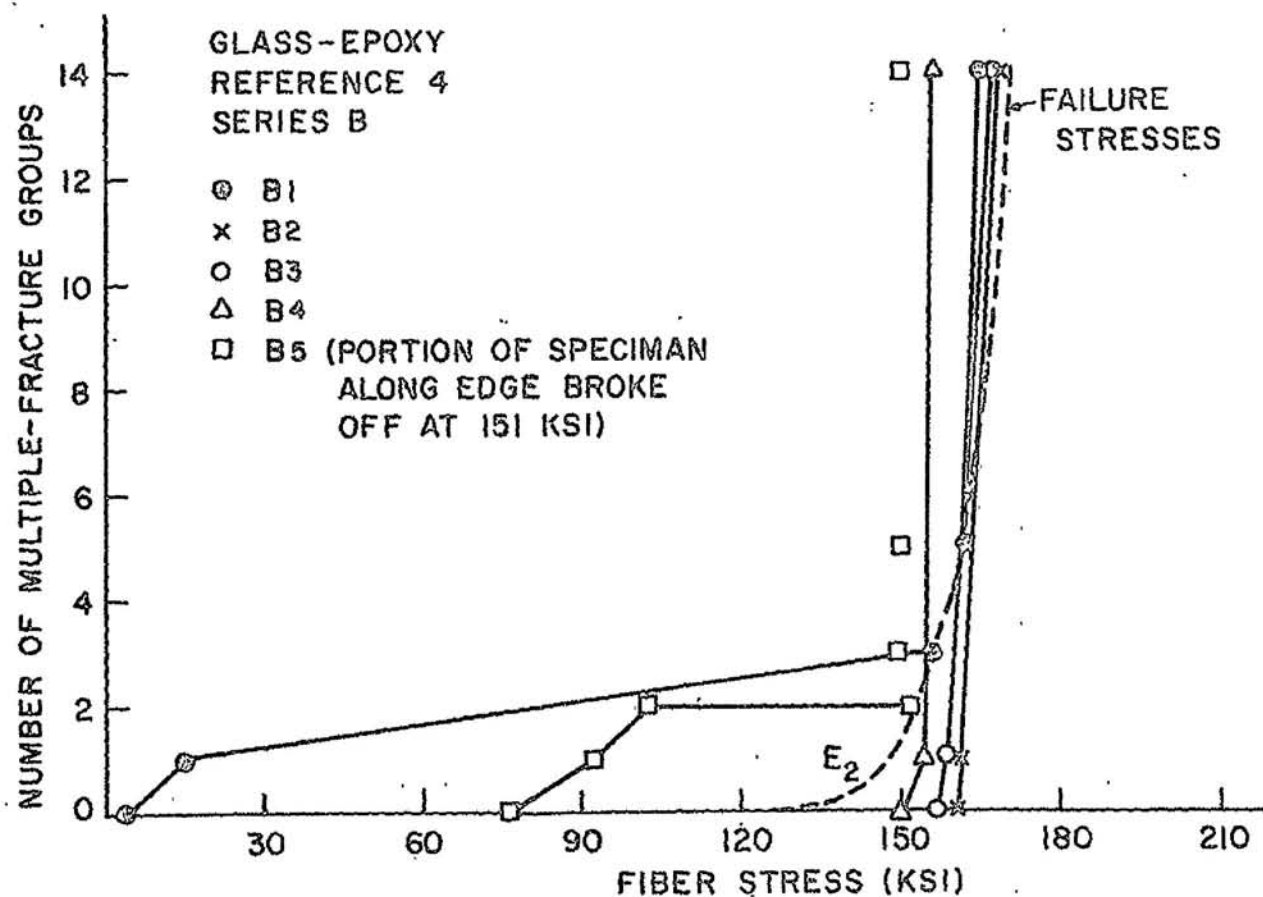


Figure 13. Observed and Predicted Multiple-Fracture Groups (Ref. 4, Series B).

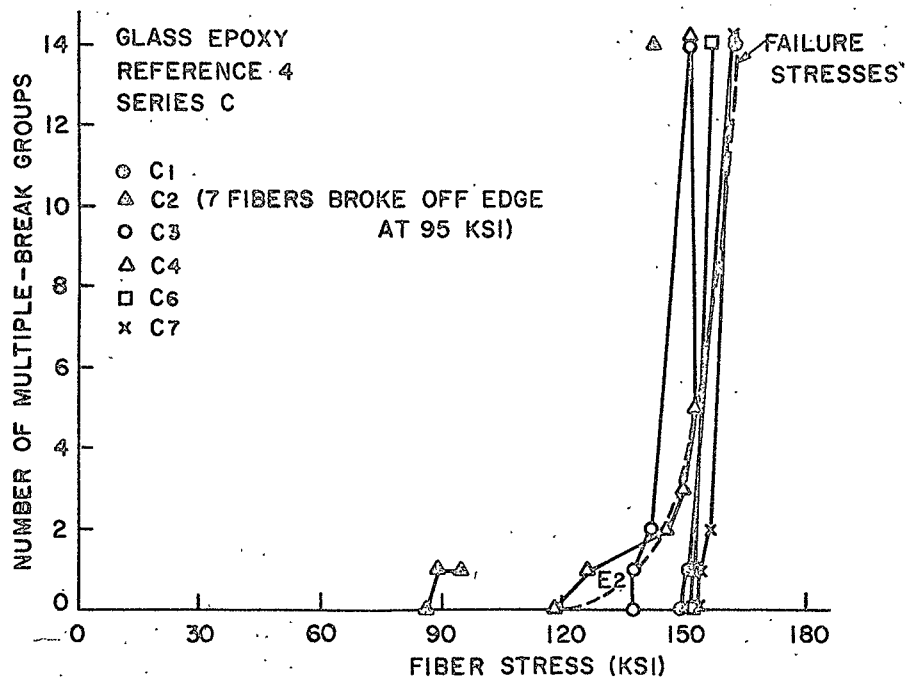


Figure 14. Observed and Predicted Multiple-Fracture Groups (Ref. 4, Series C).

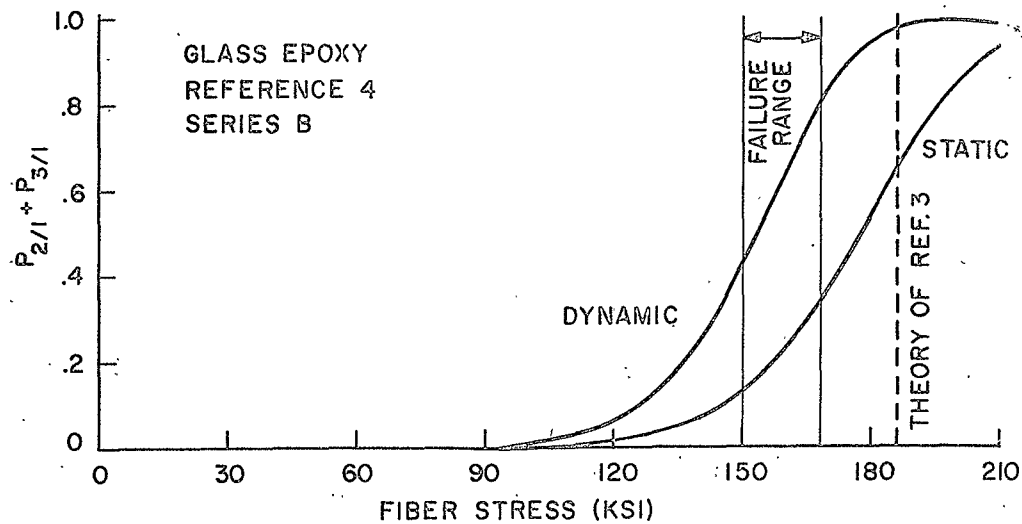


Figure 15. Static and Dynamic Values of  $P_{2/1}$  and  $P_{3/1}$  as a Function of Applied Load (Ref. 4, Series B).

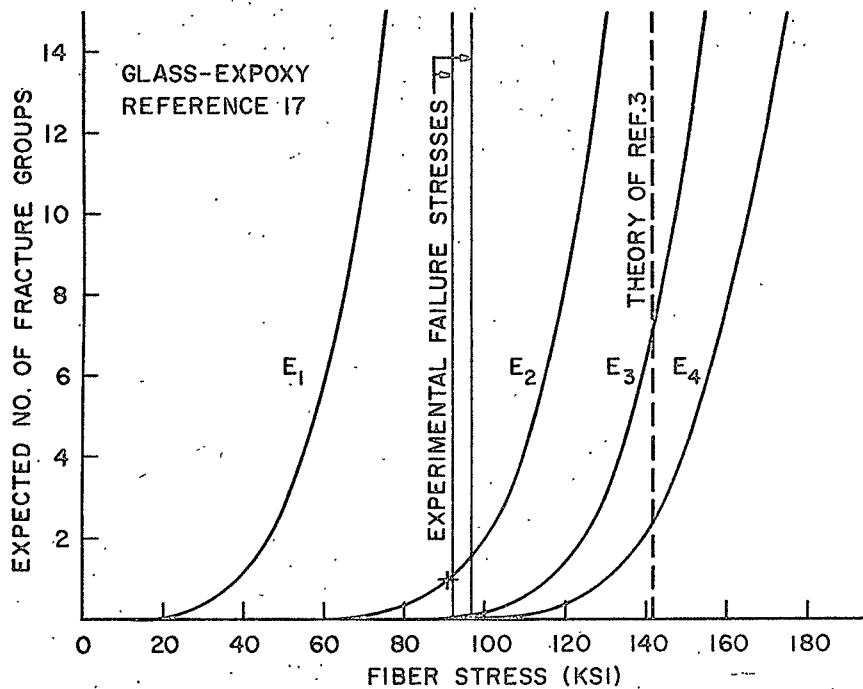


Figure 16. Expected Number of Fracture Groups as a Function of Applied Load (Ref. 17 Tests).



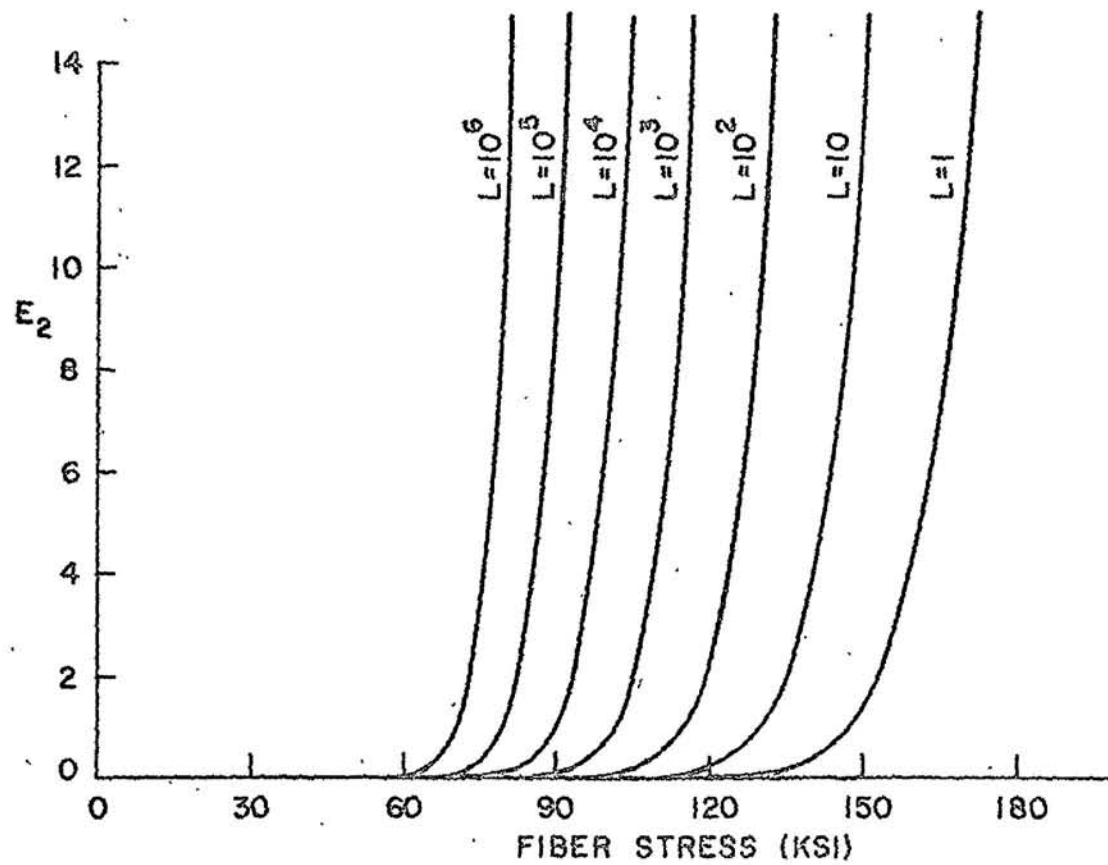


Figure 17. Variation of  $E_2$  with Applied Stress for Various Composite Lengths (Ref. 4, Series B).

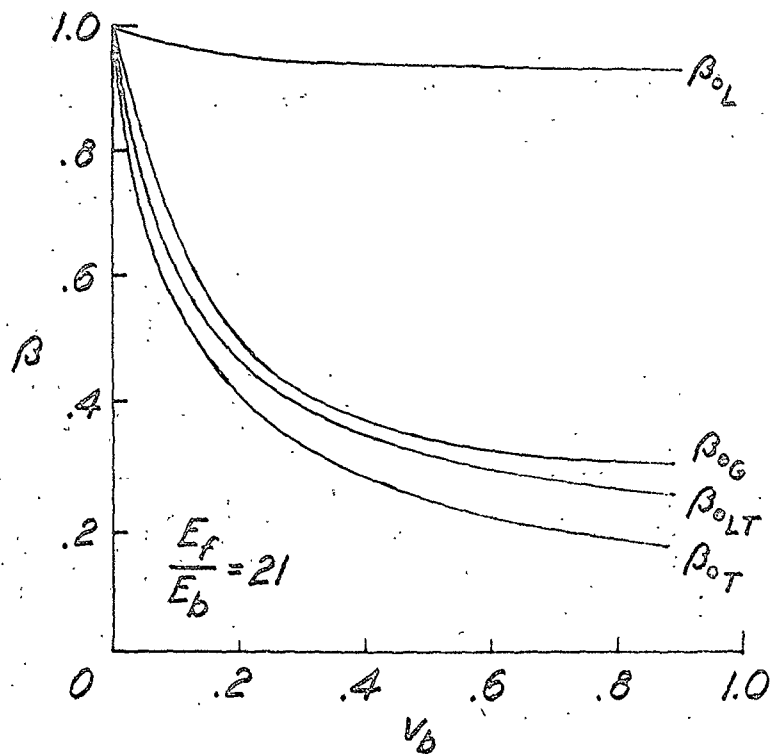


Figure 18. Typical Variations of Transverse Effectivenesses of Filamentary Reinforcement with Volume Fraction, as Calculated for an E-Glass/Epoxy Composite.

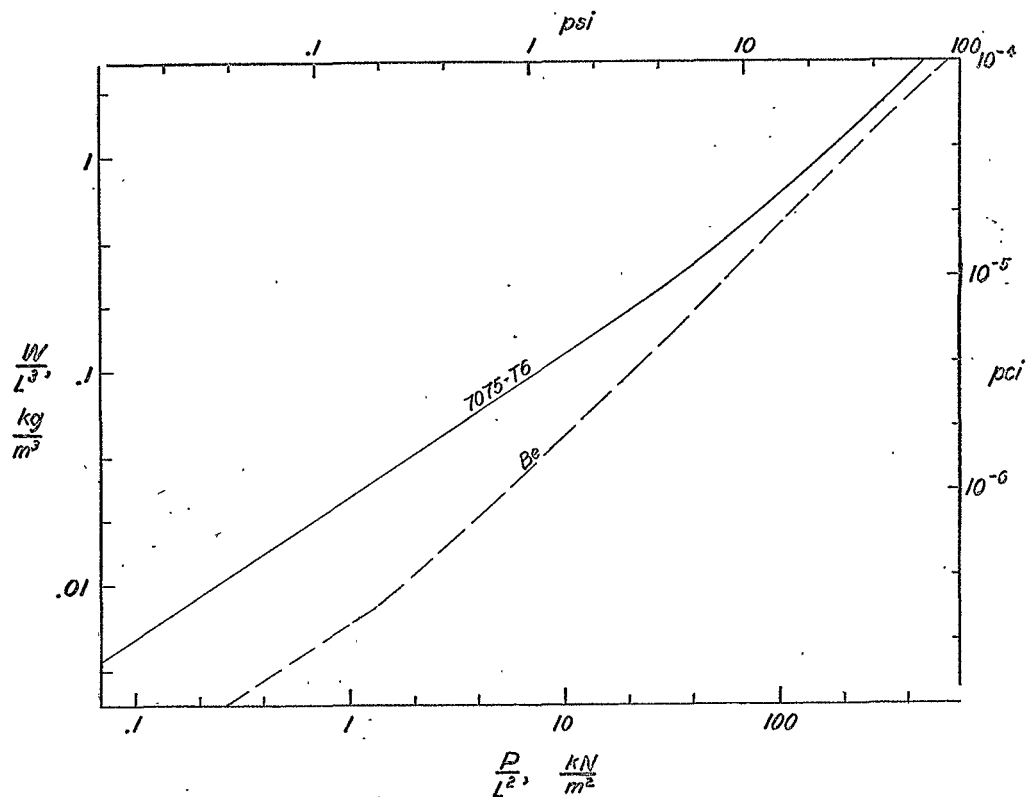


Figure 19. Efficiencies of Round, Unreinforced Tube - Columns of 7075-T6 Aluminum Alloy and Beryllium.

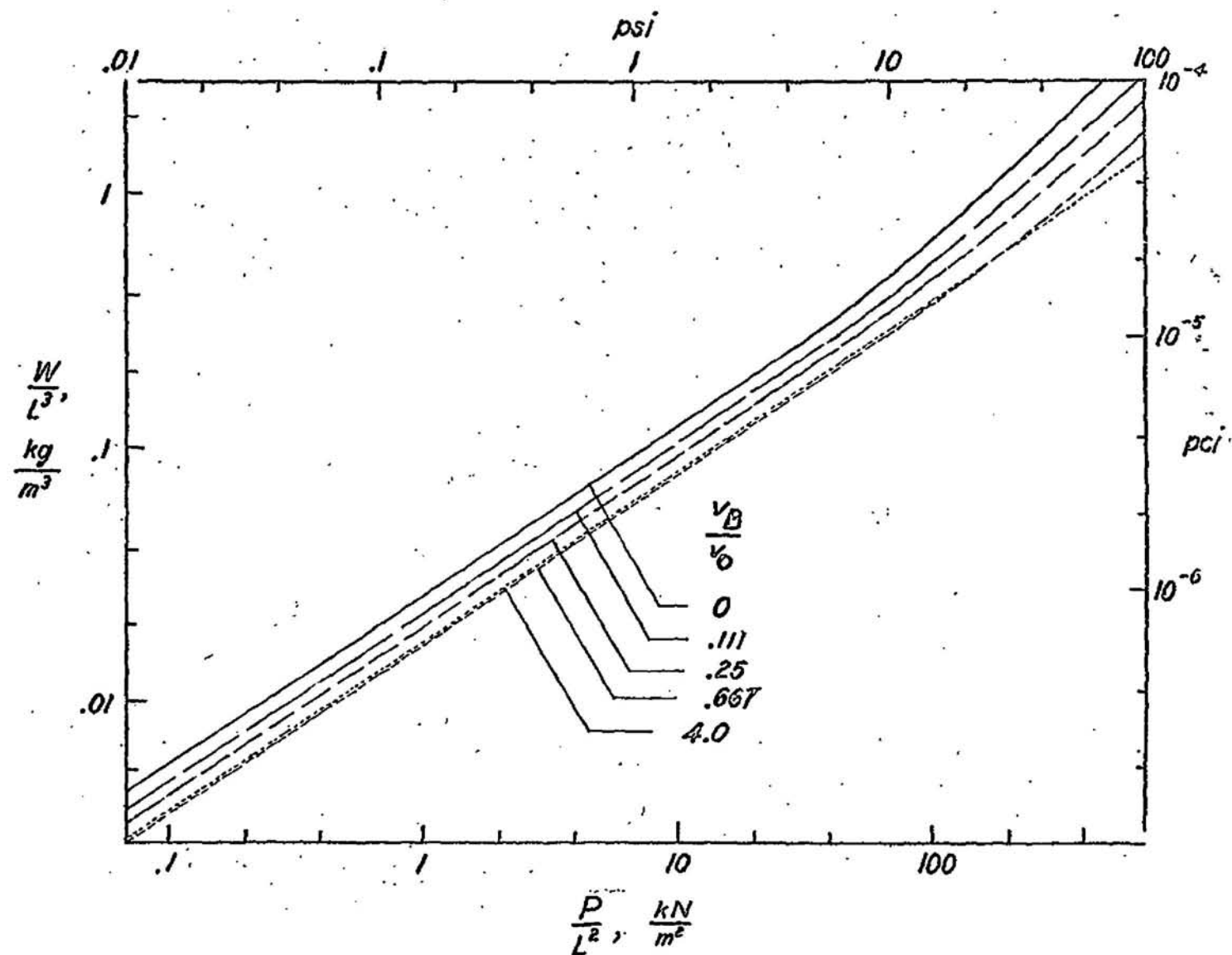


Figure 20. Efficiencies of Round 7075-T6 Aluminum - Alloy Tube-Columns Reinforced at Three Circumferential Points by Uni-directional Boron/Epoxy Stiffeners.

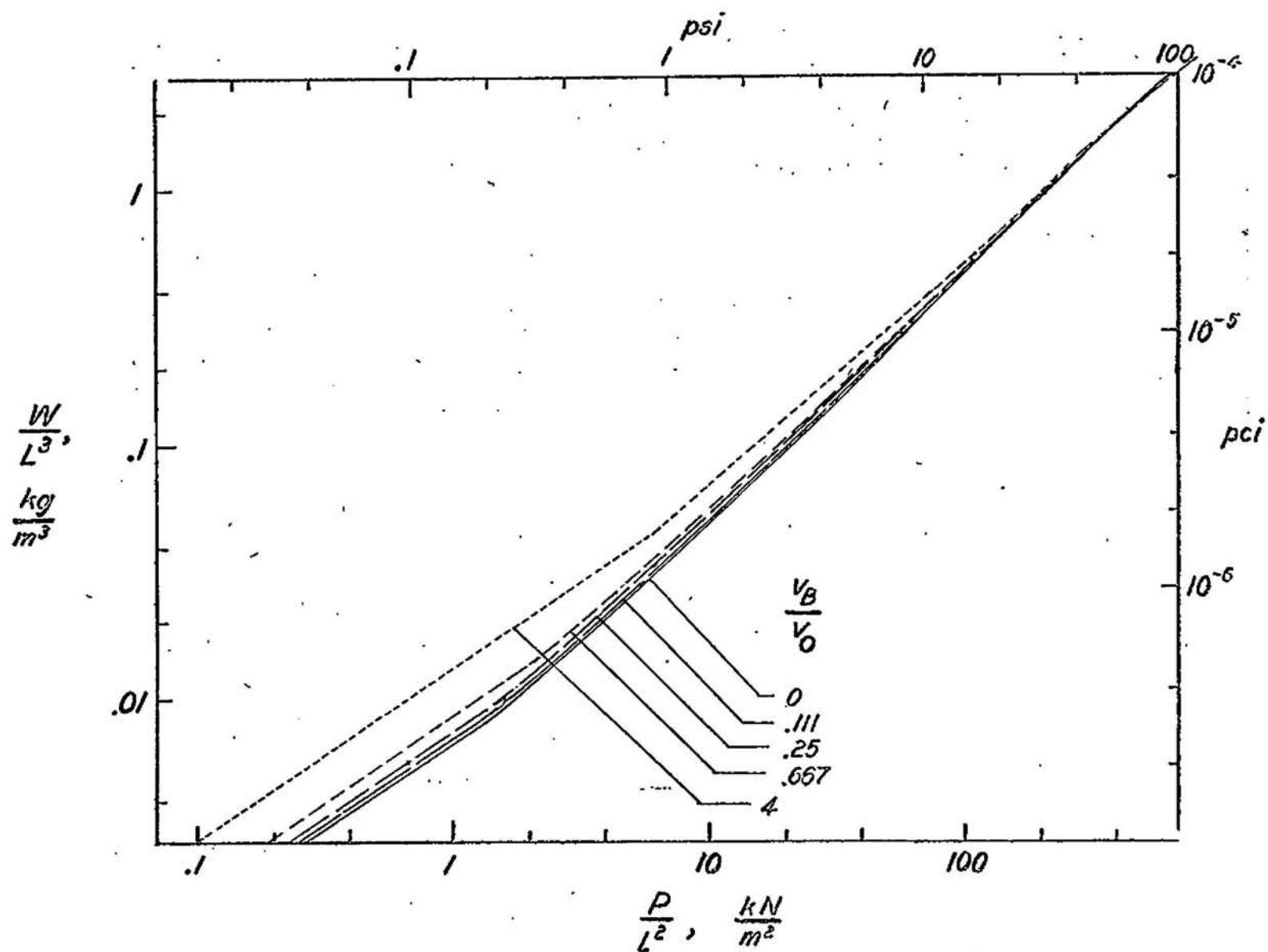


Figure 21. Efficiencies of Round Beryllium Tube-Columns Reinforced at Three Circumferential Points By Uni-directional Boron/Epoxy Stiffeners.

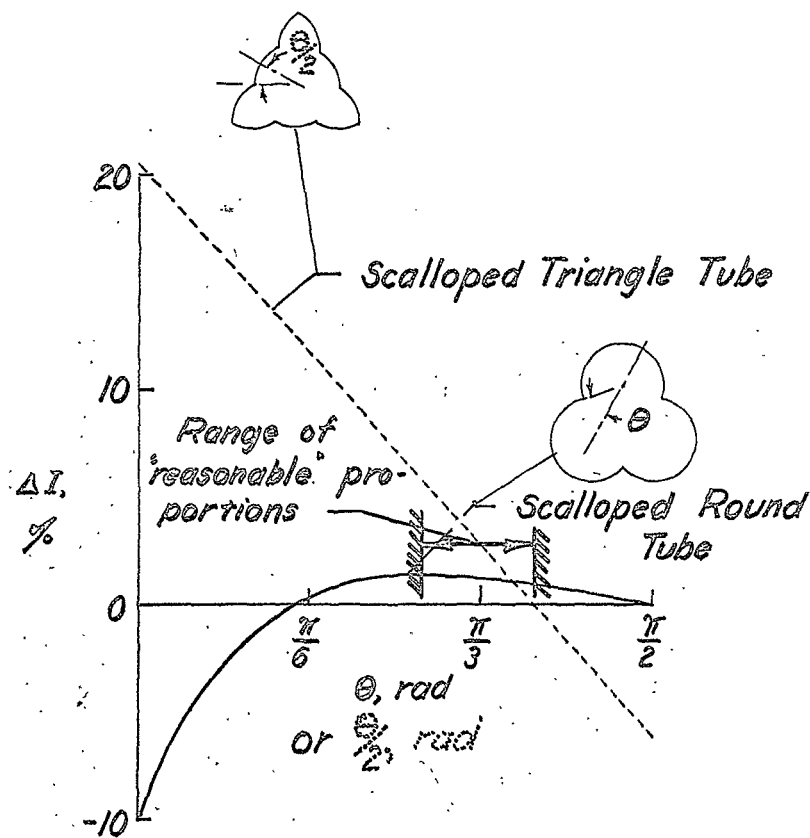


Figure 22. Changes in Column-Binding Characteristics of Scalloped Thin-Walled Tubes at Constant  $R/t$  with Angle Included by Scallop;

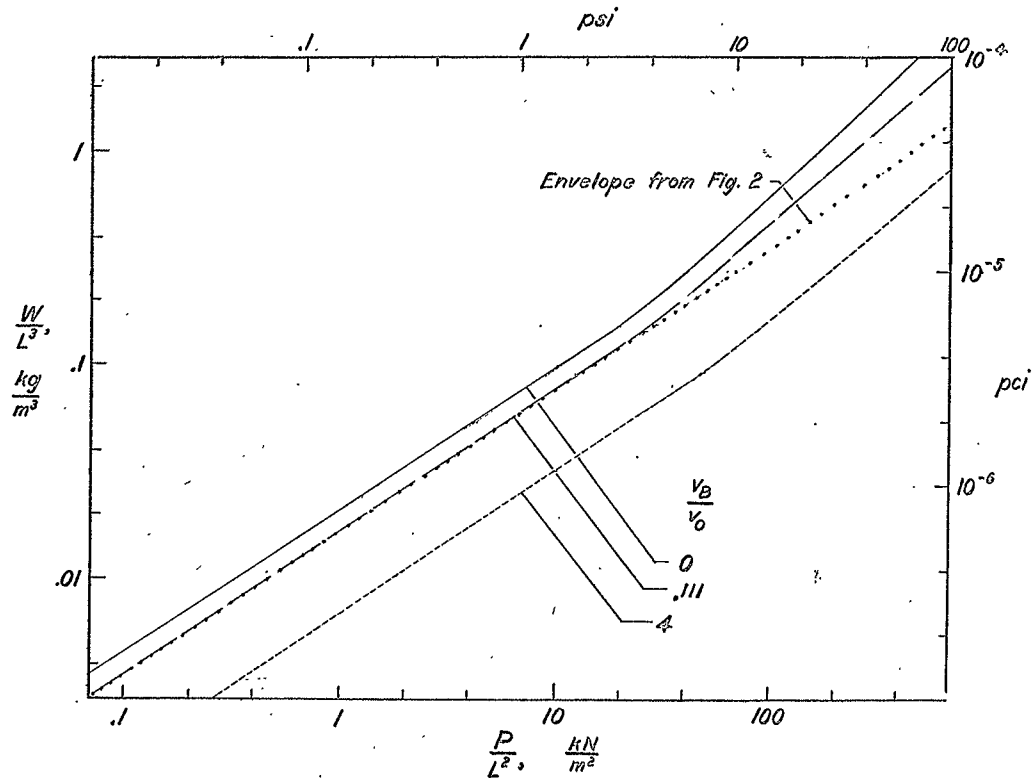


Figure 23. Efficiencies of 7075-T6 Aluminum-Alloy Scalloped Triangle Thin-Walled Tube Columns Reinforced at Apexes with  $0^\circ$  Boron/Epoxy Stiffeners, and Comparison with Minimum-Weight Reinforced 7075-T6 Round Tubes.

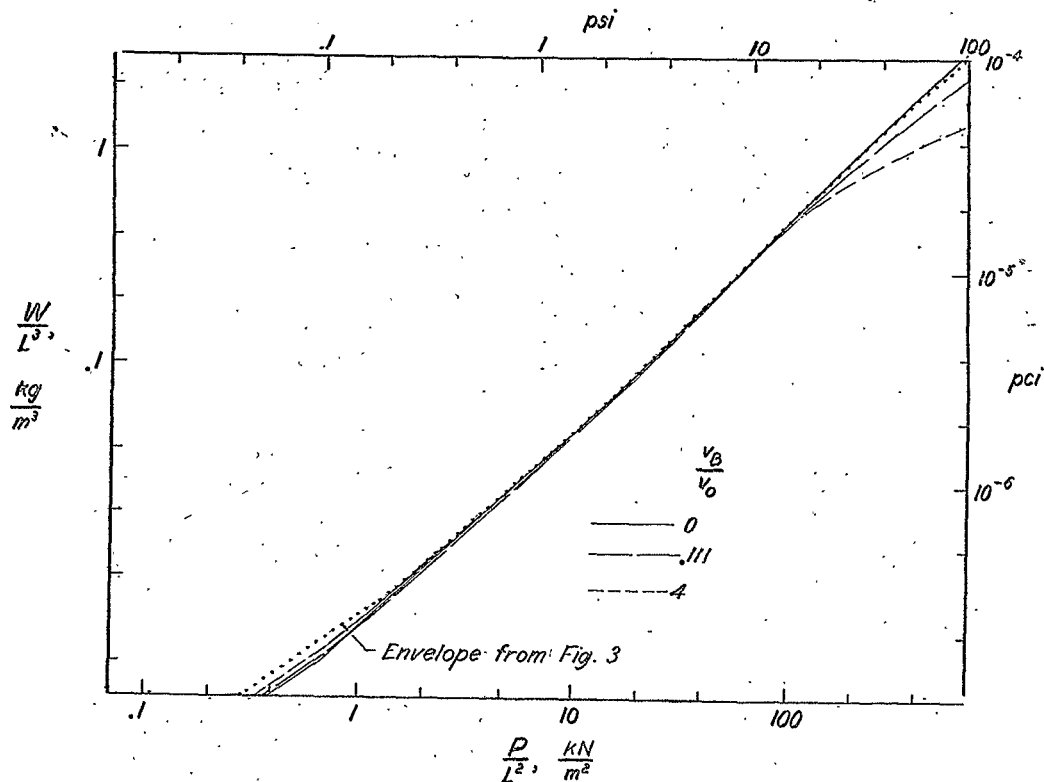


Figure 24. Efficiencies of Beryllium Scalloped Triangle Thin-Walled Tube Columns Reinforced at Apexes with  $0^\circ$  Boron/Epoxy Stiffeners, and Comparison with Minimum-Weight Reinforced Beryllium Round Tubes.



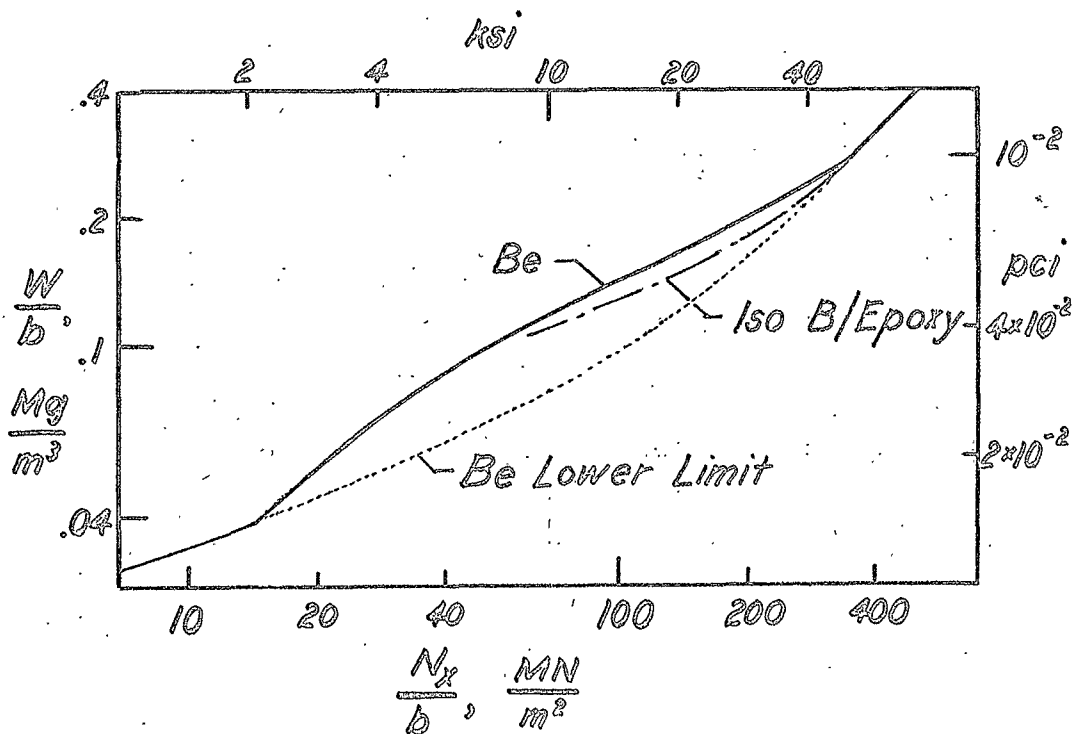


Figure 25. Efficiencies of Solid-Sandwich Plates having  $0^\circ$  Reinforced Boron/Epoxy Cores and Faces of Various Materials.

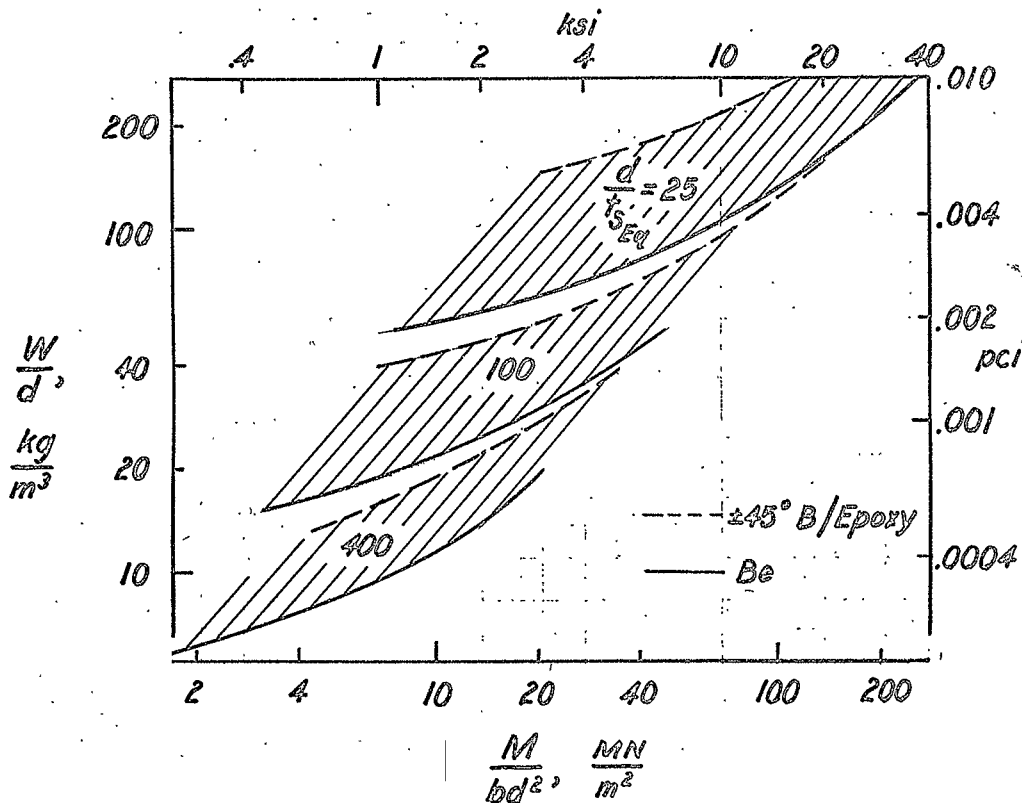
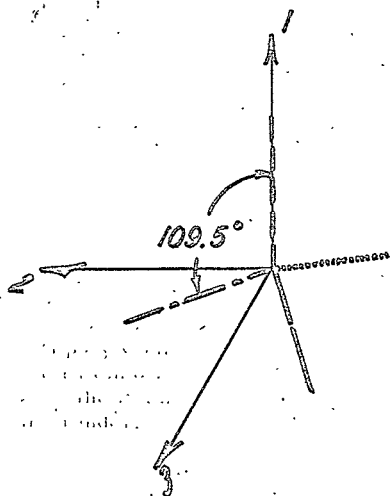


Figure 26. Comparative Efficiencies of Wing Box Beams having  $\pm 45^\circ$  Boron Reinforced Epoxy Compression Skins and Beryllium Skins on  $0^\circ$  Reinforced Boron/Epoxy Z-Section Stiffeners.

## Caltropic Reinforcement



$\nu_f$	$A_1$		$A_4 = A_6$	
	$\beta_s =$	$\beta_s \neq$	$\beta_s =$	$\beta_s \neq$
0.2	1.397	1.441	1.333	1.375
.4	2.198	2.234	2.062	2.110
.6	3.268	3.273	3.034	3.093
.8	4.977	4.987	4.525	4.779

Figure 27. Calculated Compliances  $A_1$ ,  $A_4$ , and  $A_6$ , Caltropic Reinforcement in the Directions of the Orthotropic axis 1-, 2-, 3- Respectively, for Equal and Unequal Assumed Transverse Effectivenesses  $\beta$ . ( $E_f = 10$ ,  $E_b = \frac{10}{21}$ ,  $\nu_f = 0.2$ ,  $\nu_b = 0.35$ ).

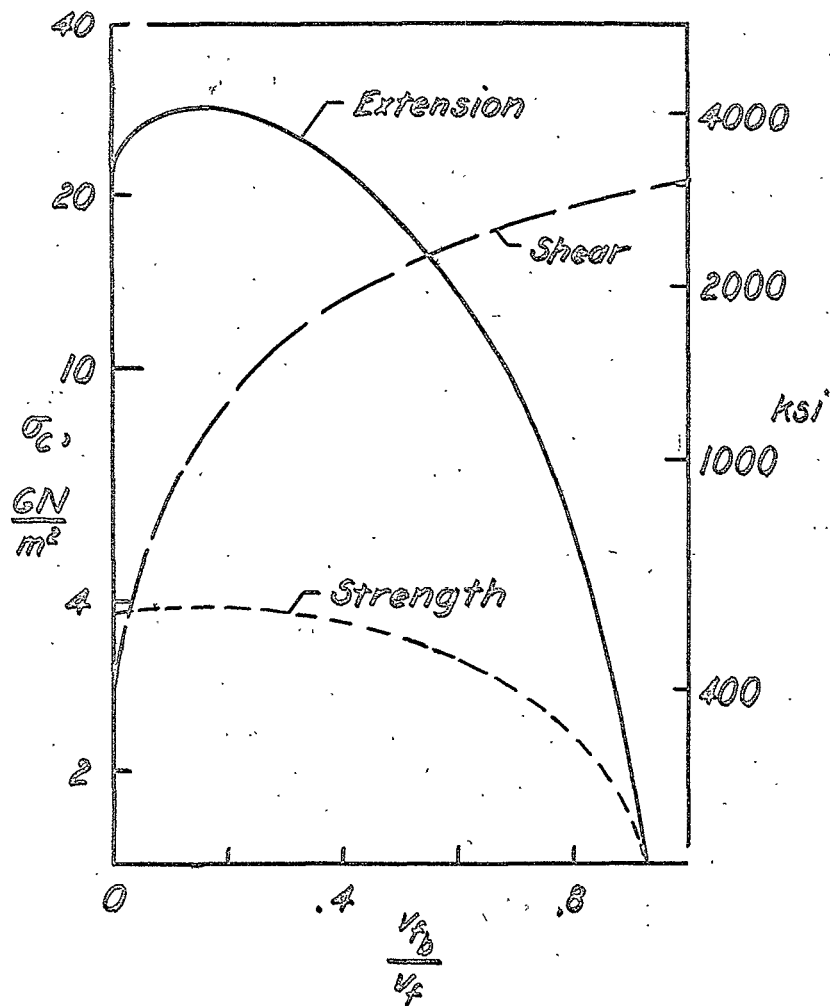


Figure 28. Calculated Compressive Strengths for Three Indicated Failure Modes for a Boron/Epoxy Composite of Nominal Constituent Properties with Constant Total Reinforcement Volume Fraction of 50% but Varying Proportions of the Reinforcement Uni-directional and Randomly Dispersed in the Binder.

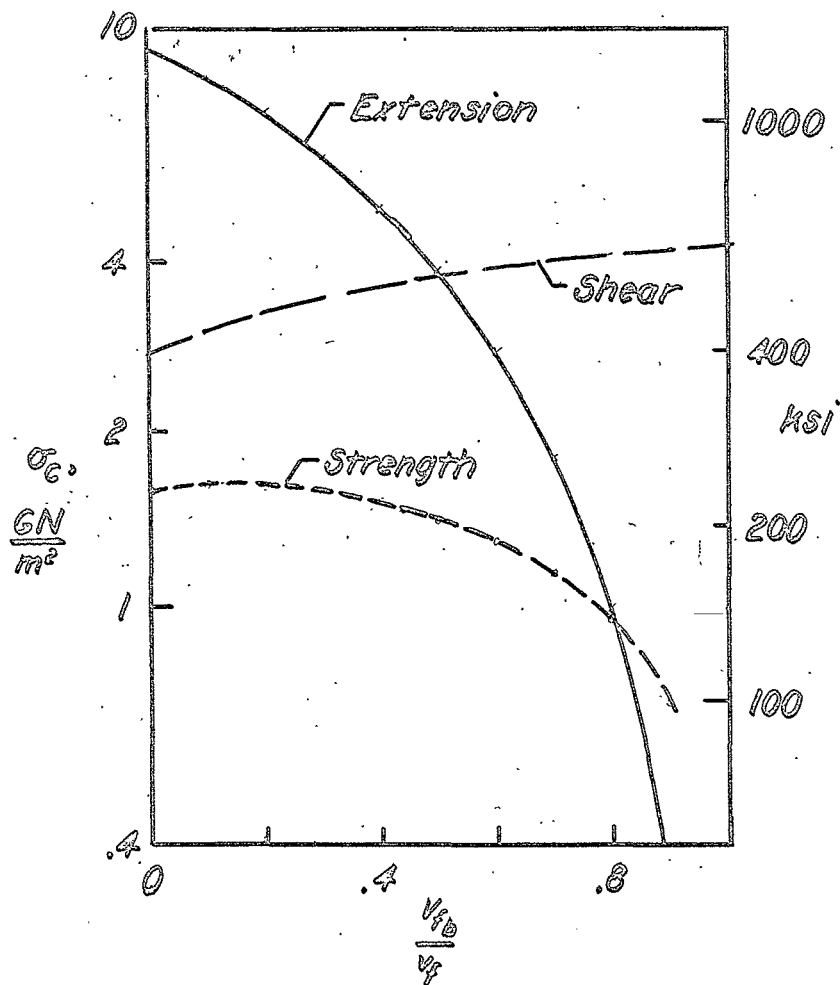


Figure 29. Calculated Compressive Strengths for Three Indicated Failure Modes for Glass/Epoxy Composites of Nominal Constituent Properties with Constant Total Reinforcement Volume Fraction of 50%, but Varying Proportions of the Reinforcement Uni-directional and Randomly Dispersed in the Binder.

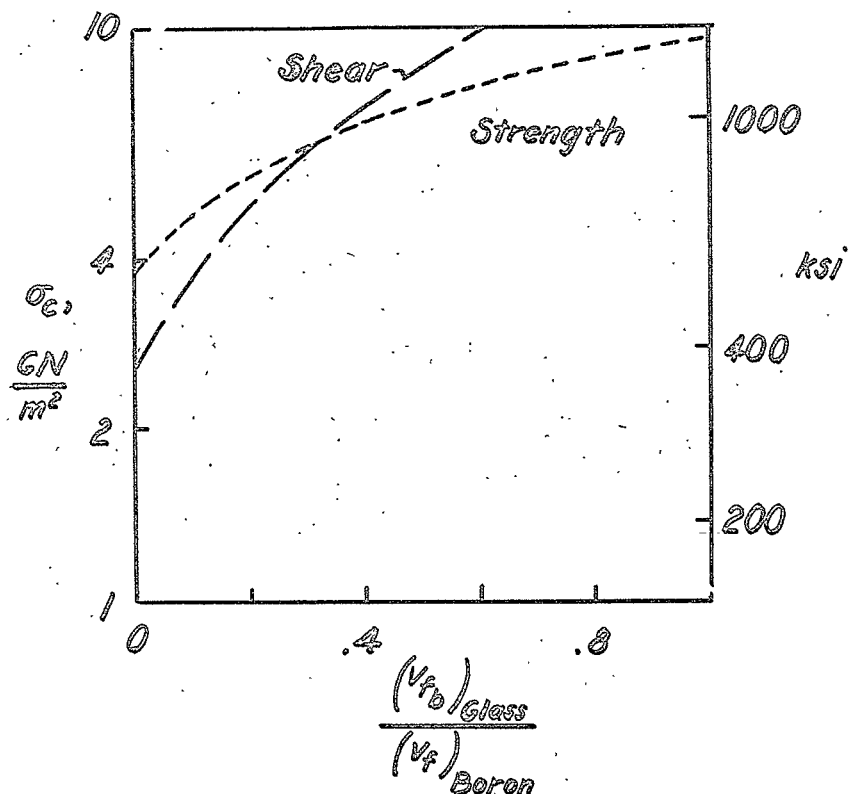


Figure 30. Calculated Compressive Strengths for Glass-Boron/Epoxy Composites of Nominal Constituent Properties with Constant Uni-Directional Boron Reinforcement Volume Fraction  $V_f \approx 0.5$  and Varying Quantities of Randomly Dispersed Glass Filaments in the Binder.

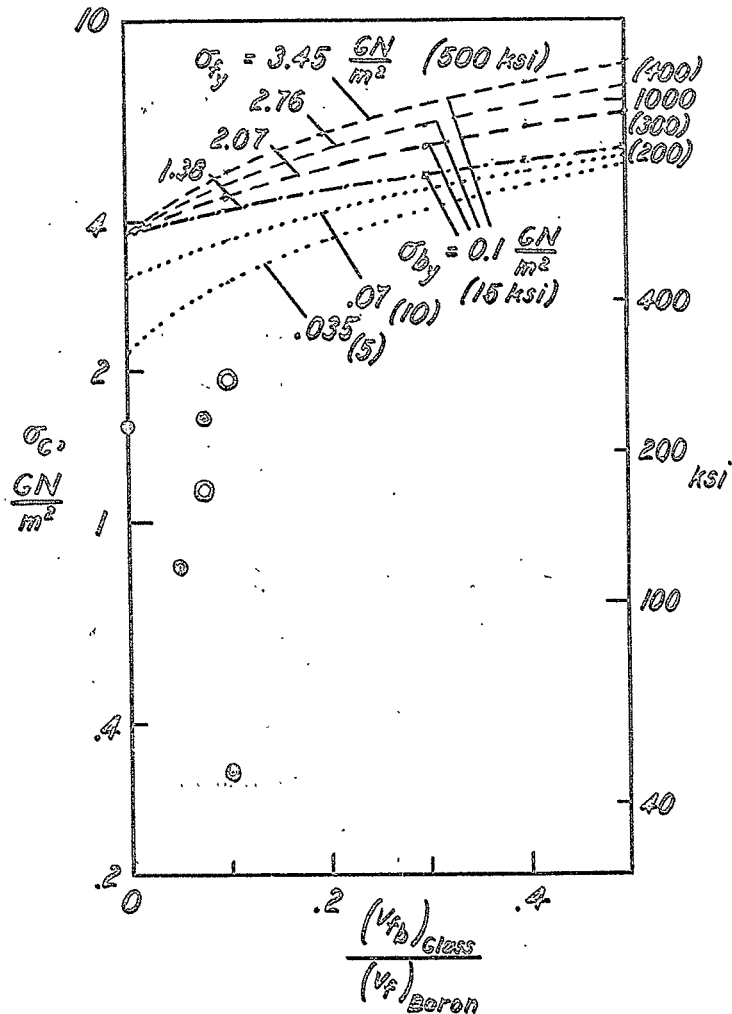
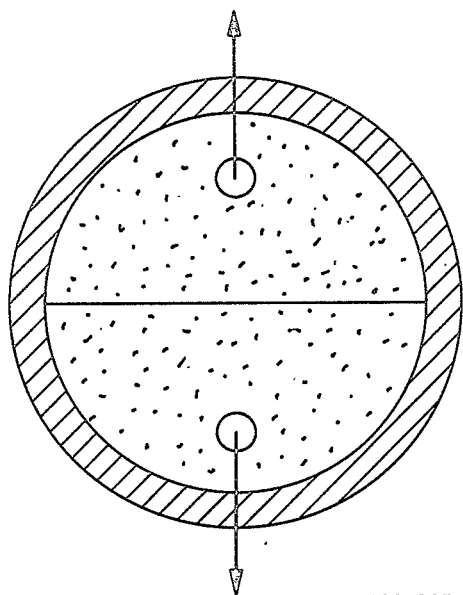


Figure 31. Experimental Results for Tests of Glass-Boron/Epoxy Composites having Uni-directional Boron Filamentary Reinforcement of Nominally 50% by Volume, and Comparison with Calculations for Various Glass-Filament and Binder Strengths.

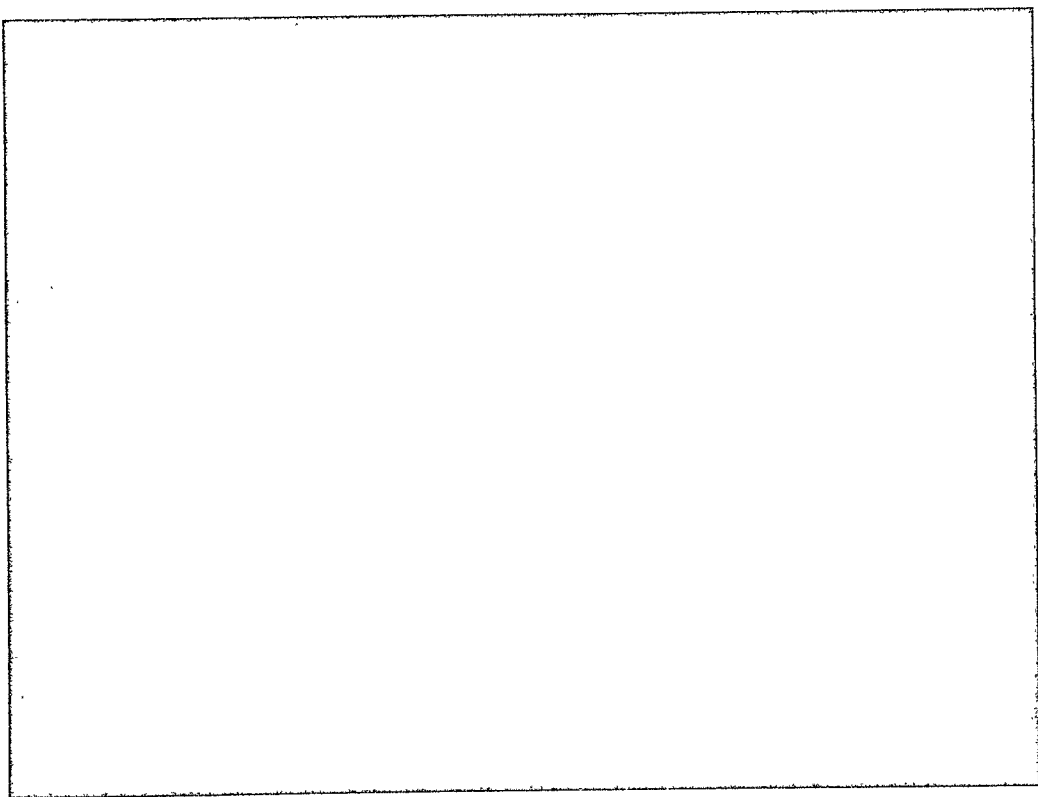


*N 402-093*

Figure 32. Schematic of N. O. L. Ring, "Split-Dee" Tensile Test.



GRAPHIC NOT REPRODUCIBLE



GRAPHIC NOT REPRODUCIBLE

Figure 33. Photoelastic Study of Stresses in the Vicinity of the Split between the Dees in an N. O. L. Ring "Split-Dee" Tensile Test.

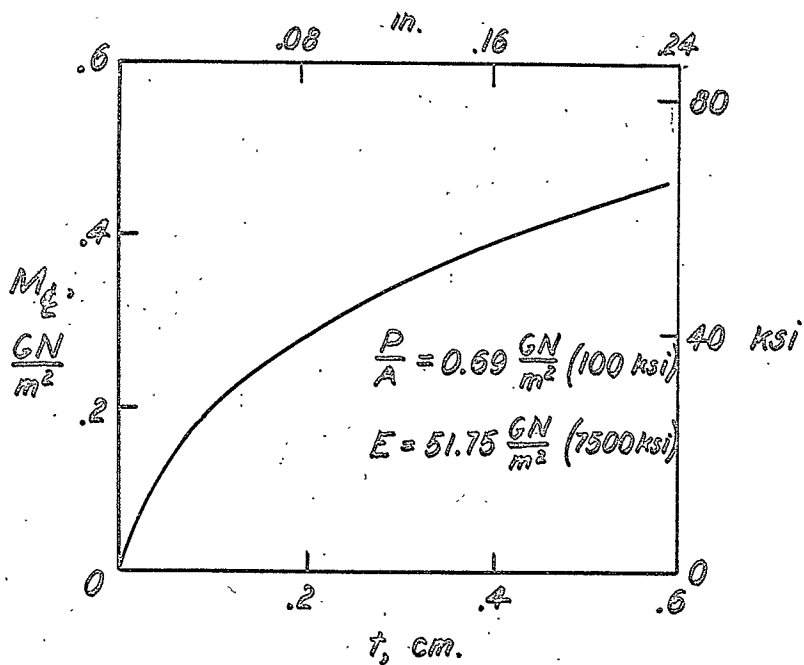
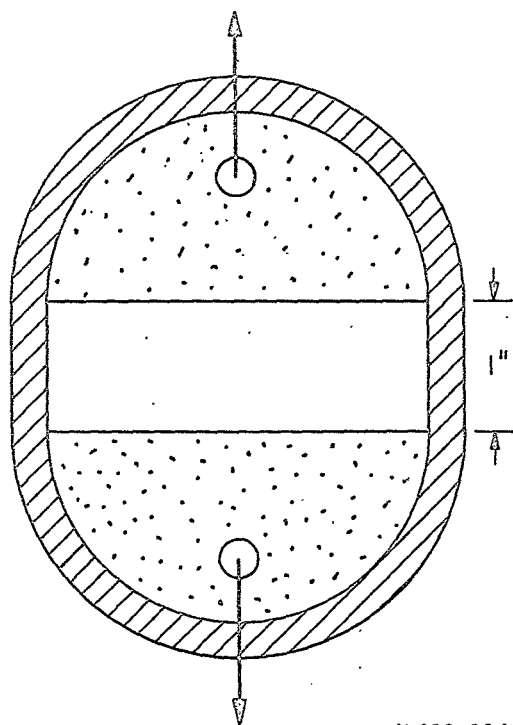


Figure 34. Results of Analysis of Maximum Bending Moment in the "Split-Dee" Test of a Glass Filament Reinforced Epoxy N.O.L. Ring.



*N 402-094*

Figure 35. "Race-Track", Filament-Wound Tensile Specimen.

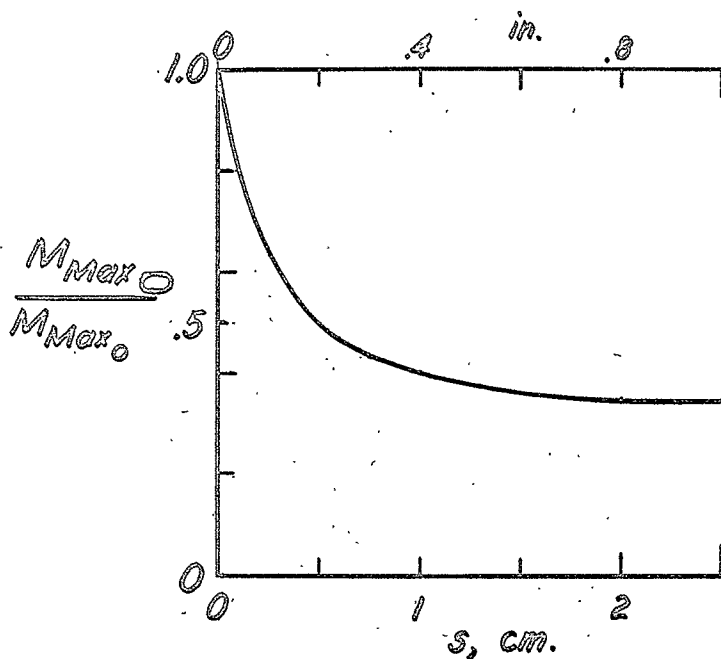
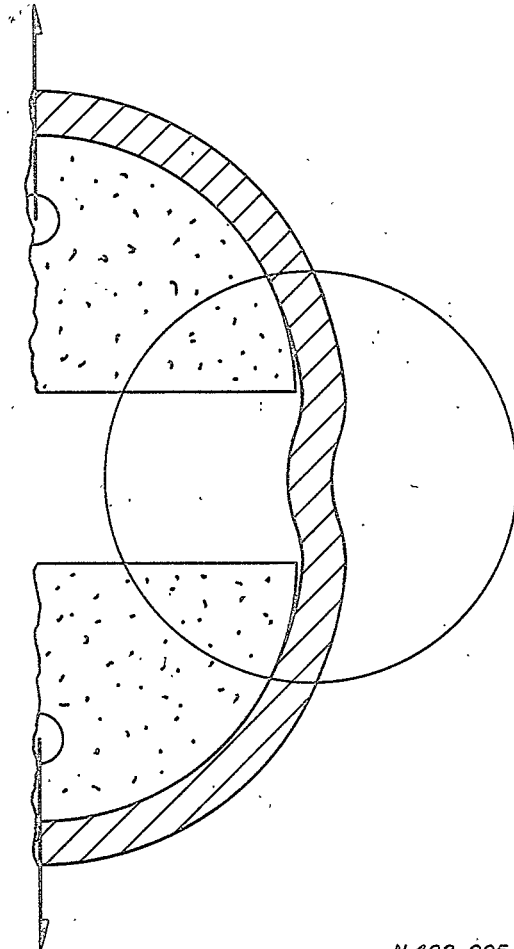


Figure 36. Ratios of Maximum Bending Moments Induced in Race-Track and Circular 0.15 cm. (0.06 in.) Thick Split-Dee Specimens of Glass/Epoxy at  $0.69 \frac{\text{GN}}{\text{m}^2}$  (100 ksi) Axial Stress.



N 402-095

Figure 37. Schematic Representative of Mechanics of Deflection of "Race-Track" Specimen.

GRAPHIC NOT REPRODUCIBLE

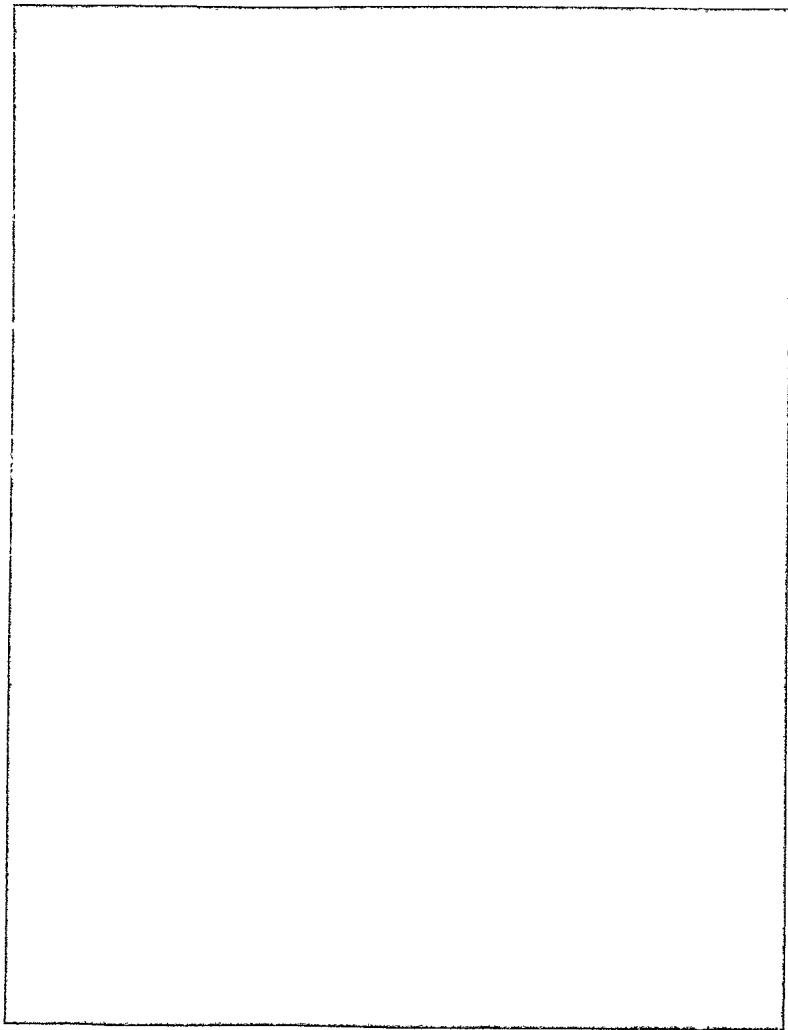


Figure 38. Photoelastic Study of Stresses in the Straightaway of a "Race-Track" Specimen.

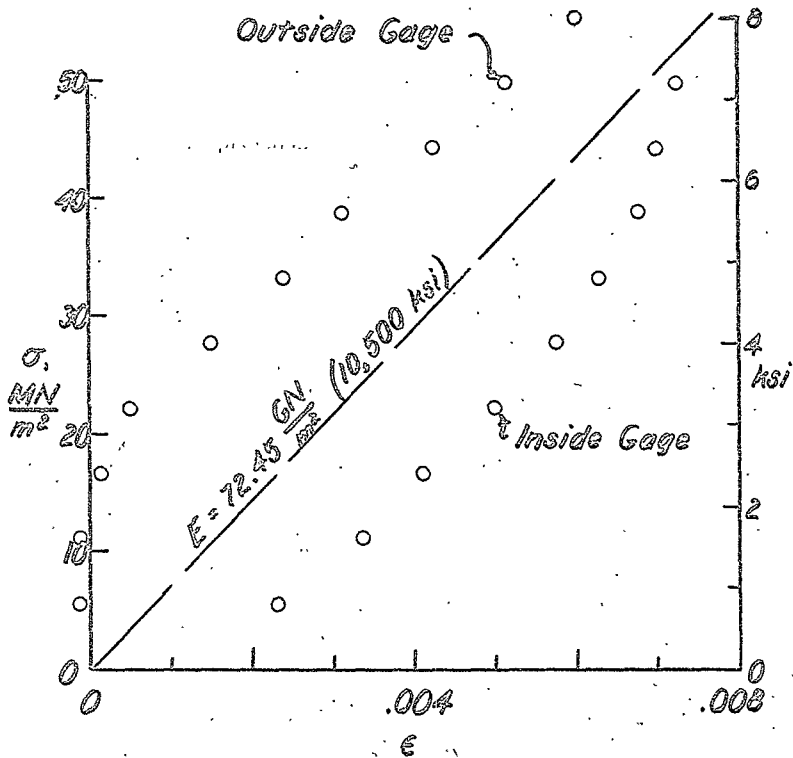


Figure 39. Strain Measurements Near the Split in the Dee in N.O.L. Ring Type Split-Dee Tension Test.

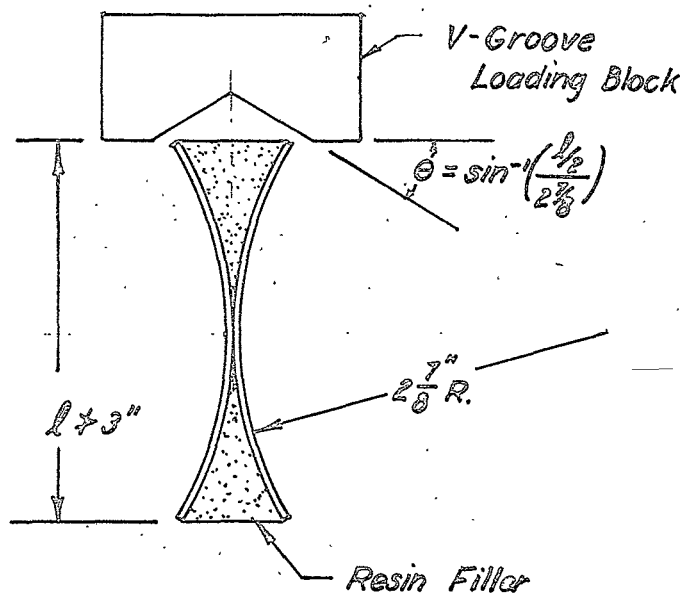


Figure 40. Proposed Compression Specimen Made from Segments of NOL Ring.



GRAPHIC NOT REPRODUCIBLE



GRAPHIC NOT REPRODUCIBLE

Figure 41. Aluminum Insert from Specimen Similar to that of Figure 40 after Test.

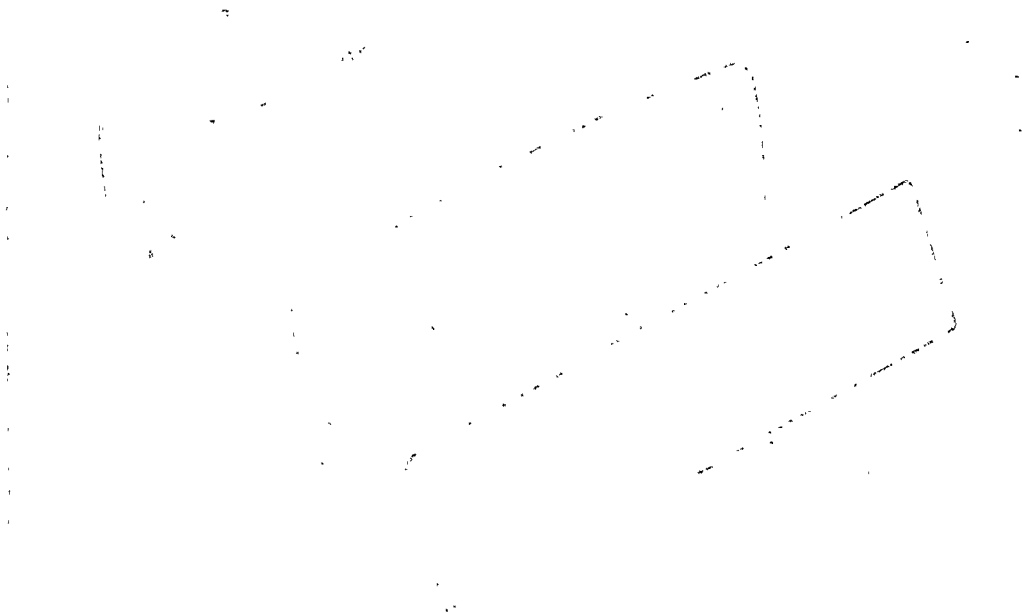
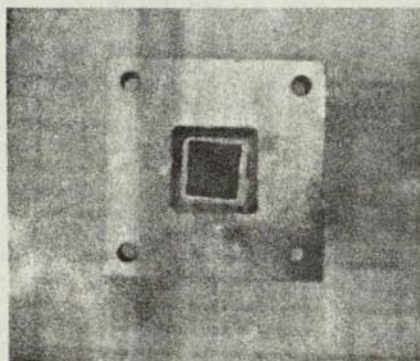
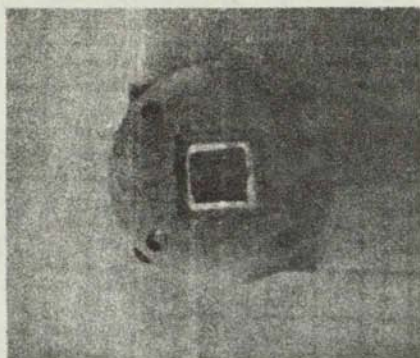


Figure 42. N.O.L. Ring Segment Compression Test Specimen Showing Shear Failure.

GRAPHIC NOT REPRODUCIBLE



GRAPHIC NOT REPRODUCIBLE

Figure 43. Top and End Views of Compression Specimen Cast in Gerrobend End Fixtures.